Effect of fabrication parameters on thermophysical properties of sintered wicks

by

Francisco Alonso Domínguez Espinosa

B.S., Mechanical Engineering
Instituto Tecnológico y de Estudios Superiores de Monterrey, 2008

Submitted to the Department of Mechanical Engineering
in partial fulfillment of the requirements for the degree of

Master of Science in Mechanical Engineering

at the

MASSACHUSETTS INSTITUTE OF TECHNOLOGY

September 2011

Author .....
Department of Mechanical Engineering
August 19, 2011

Certified by .....
John G. Brisson
Professor of Mechanical Engineering
Thesis Supervisor

Accepted by .....
David E. Hardt
Chair, Committee on Graduate Students

Effect of fabrication parameters on thermophysical properties of sintered wicks

by

Francisco Alonso Domínguez Espinosa

Submitted to the Department of Mechanical Engineering
on August 19, 2011, in partial fulfillment of the
requirements for the degree of
Master of Science in Mechanical Engineering

Abstract

Porous wicks for use in a loop heat pipe were sintered from copper and Monel powder. These wicks were characterized in terms of their shrinkage, porosity, thermal conductivity, liquid permeability and maximum capillary pressure. The effect of fabrication parameters (particle size and sintering conditions) on these properties was studied. Shrinkage was found to increase with increasing sintering time and temperature. Porosity followed the opposite trend. For a given sintering temperature, thermal conductivity of the samples was found to increase as the sintering time increased. Permeability and capillary pressure were found to be independent of the sintering time as long as the wick stayed bonded to the walls of its container. In addition to measuring the properties of the wicks, a model for predicting their thermal conductivity was developed. First, the so-called 'two-sphere model' is used to relate the sintering conditions to the size of the connections between particles (referred as 'necks'). Then, a finite element simulation was used to determine the thermal resistance of diverse unit cells as a function of the neck size between the particles. Finally a `MATLAB` simulation program was written to generate a random 3D resistor network as means to model the multiple connections between spheres in a wick. The `MATLAB` code was used to calculate the effective thermal conductivity of the wick. Comparison of the model predictions with the experimental data showed good agreement.

Thesis Supervisor: John G. Brisson
Title: Professor of Mechanical Engineering

Acknowledgments

「この番組は、ご覧のスポンサーの提供でお送りしました」

I thank Professor Brisson who provided continuous encouragement, guidance and advice. I am indebted to Dr. Teresa Peters for all her support throughout the project. I also thank Professor Wang and Professor Lang for their valuable advice.

Thanks to Michael Demaree, who helped me a great deal preparing my experimental setup and to Tess Saxton-Fox, who performed many of the experiments. Thanks to my mates in the Cryogenics Lab and in the PHUMP team for their friendliness and support.

Lastly, I would like to thank my family and friends in Mexico for their support.

This research was funded by a DARPA grant (W31P4Q-09-1-0007), by the Mexican National Council for Science and Technology (CONACYT) and the General Direction of Foreign Affairs of the Mexican Ministry of Education (DGRI-SEP).

Contents

List of Figures

List of Tables

List of Symbols

Roman Letters

A_{cs}	Cross-sectional area of the wick
a	Particle radius / Constant
b	Grain boundary width
C	Constant
c	Concentration of species / Edge thermal conductance
c_p	Specific heat capacity
D	Diameter of sample
D_{GBD}	Grain boundary diffusion
D_{GBD_0}	Pre-exponential factor for grain boundary diffusion
D_{SD}	Surface diffusion
D_{SD_0}	Pre-exponential factor for surface diffusion
D_{VD}	Volume (crystal) diffusion
d	Thickness of sample
$\mathbf{f}$	Transport rate matrix
f	Transport rate matrix entry
h	Shrinkage parameter
i	Index variable
$\vec{J}$	Diffusion flux
j	Index variable
$\mathbf{K}$	Laplacian matrix
k	Boltzmann constant / Laplacian matrix entry

ℓ	Length of sample
l_{uc}	Length of the unit cell
M	Mobility of species / Molar volume
m	Mass / Exponent / Index variable
$\dot{m}$	Mass flow rate
N_A	Avogadro's number
n	Exponent
P	Pressure
$\dot{Q}$	Heat flux
Q_{GBD}	Activation energy of grain boundary diffusion
Q_{SD}	Activation energy of surface diffusion
R	Radius of curvature / Gas constant
R_{cube}	Thermal resistance of normalization cube
R_{cyl}	Thermal resistance of normalization cylinder
R_{th}	Thermal resistance
$R_{th,BCC}$	Thermal resistance of BCC-based unit cell
$R_{th,\text{across}}$	Thermal resistance between opposed bases
$R_{th,\text{bent}}$	Thermal resistance between perpendicular bases
$R_{th,eff}$	Effective thermal resistance of sinter
$R_{th,FCC}$	Thermal resistance of FCC-based unit cell
s	Size of the structural matrix
T	Temperature
t	Time
t^*	Reduced time
$\mathbf{U}$	Potential difference matrix
$\mathbf{u}$	Vector
V	Volume of sample
V_{sph}	Total volume occupied by particles
x	Neck radius
x^*	Dimensionless neck radius

x_0 Initial neck size

x_{exp} Experimentally measured neck radius

x_{TSM} Two-sphere model predicted neck radius

Greek Letters

α Thermal diffusivity

Γ Ratio of effective grain boundary diffusivity to effective surface diffusivity

γ Surface tension / Surface energy

δ Interatomic distance

δ_{GBD} Characteristic cross-sectional grain boundary diffusion length

δ_{SD} Characteristic cross-sectional surface diffusion length

ϵ Linear shrinkage

ϵ_{exp} Experimentally measured linear shrinkage

ϵ_{TSM} Two-sphere model linear shrinkage

κ Permeability of wick / Local curvature / Thermal conductivity

κ^* Dimensionless thermal conductivity

κ_{eff} Effective thermal conductivity

κ_{material} Thermal conductivity of the solid material

μ Viscosity of water / Chemical potential

ρ Density / Radius of curvature of neck

ρ_{wick} Density of wick

ρ_{material} Density of solid material

Φ Diffusion potential

ϕ Porosity

ϕ_0 Porosity at $t = 0$

φ Fraction of particles that guarantees percolation

Ω Atomic volume

Chapter 1

Introduction

Heat pipes were proposed in the 1960s as a possible solution to the ever increasing heat generation rates in high-performance electronic systems [19]. One of the key elements of this kind of heat transfer device is a porous wick, which drives the internal flow. A knowledge of the physical characteristics of the porous material is critical in the design and manufacture of the heat pipe since its thermophysical properties directly affect the overall performance of the heat pipe.

Porous wicks can be formed with controlled properties by sintering powdered metals. Unfortunately, data in existing literature for properties such as permeability and maximum capillary pressure of this kind of wick is scattered and incomplete. In addition, many researchers have attempted to relate thermal conductivity to the porosity of the sinter, something that has not given a satisfactory match between existing models and experiments. Hence, this thesis contributes a theoretical model and experimental data that illuminate the effect of sintering time and temperature on wicks.

1.1 Motivation

Current heat sinks used to cool high density power electronics consist of a baseplate in contact with the electronics and a set of fins on the opposite side. The fins effectively

increase the surface over which heat is transferred from the base to the atmosphere. Frequently, convection over the fins is enhanced by a blower mounted on the top or the side of the fins. Nevertheless, the cooling capability of actual air-cooled heat sinks will soon be inadequate, as it is being surpassed by the scaling trends of heat dissipation in high power electronics [11, 30].

To reduce the relatively high thermal resistance associated with air-cooling, state-of-the-art heat sinks incorporate heat pipes. This thesis is part of a current effort to build a lower thermal resistance heat sink based on a loop heat pipe, as part of the Microtechnologies for Air-Cooled Exchangers (MACE) program. This program is funded by the Defense Advanced Research Projects Agency (DARPA). The proposed heat sink integrates a multi-condenser loop heat pipe and a blower in a compact design, and strives to consume no more than 33 W of electrical power to dissipate 1000 W of heat from a surface maintained at 80 °C in a 30 °C environment. The thermal resistance of the proposed system is 0.05 °C/W, four times lower than current state-of-the-art heat sink resistance [14]. Discussions of the design and experimental testing of this system can be found in the articles of Kariya et al. [27] and McCarthy et al. [35].

General analysis of heat pipes and loop heat pipes will not be addressed in the current work as it is well documented elsewhere [19, 34, 46]. Nevertheless, information in existing literature about thermophysical properties of the wicks relevant for their application in heat pipes is rather scattered. The wick structure is a key component of the heat pipe as it drives the working fluid through the system. The maximum capillary pressure that the wick can sustain, the pressure drop associated with the circulation of working fluid through it, and its thermal conductivity are all crucial design parameters of a heat pipe because of the impact they have on the performance of the heat sink. Therefore, the present study aims to contribute experimental measurements of these properties, as well as a physical model that explains and predicts them.

1.2 Description of the System

The heat exchanger that motivates this sintering study is named 'PHUMP' and is shown schematically in Figure 1.1**a**. PHUMP is composed of an evaporator, a series of condensers or thermal stators, and rotating blades interdigitated between the thermal stators. The blades are connected to a shaft driven by a permanent-magnet synchronous motor. The working fluid in this heat pipe is water.

As the name suggests, the evaporator is the component of the heat pipe where the working fluid is converted from liquid to vapor. In doing so, the system takes advantage of the relatively large latent heat of vaporization as the mechanism to transfer substantial amounts of heat out of the device being cooled. The base plate of the evaporator, as well as the wicking structure in contact with this base is copper. The high thermal conductivity of copper effectively eliminates variations in the temperature of the object to be cooled. Water vapor travels through channels in the wick ('vapor channels' in Figure 1.1**c**) and is directed to the condensing section of the heat pipe.

In current heat sink designs based on heat pipes, the condenser section of the pipe intersects a group of fins which increase the area available for convective heat transfer from the system to the environment. In contrast, in the proposed design, the fins are themselves the condensing section of the heat pipe, thus eliminating the contact thermal resistance between the heat pipe and the fins. One of these condenser-fins is schematically shown in Figure 1.1**b**. Once water condenses, it flows through the condenser wick and under the subcooling area back to the evaporator. The subcooling area permits the liquid to cool down from its saturation temperature. In this manner, revaporization of the condensed liquid is avoided. More details about the subcooling area and the suppression of vaporization will be addressed in the next section.

The heat of the system is dumped to the ambient by convection. To increase the

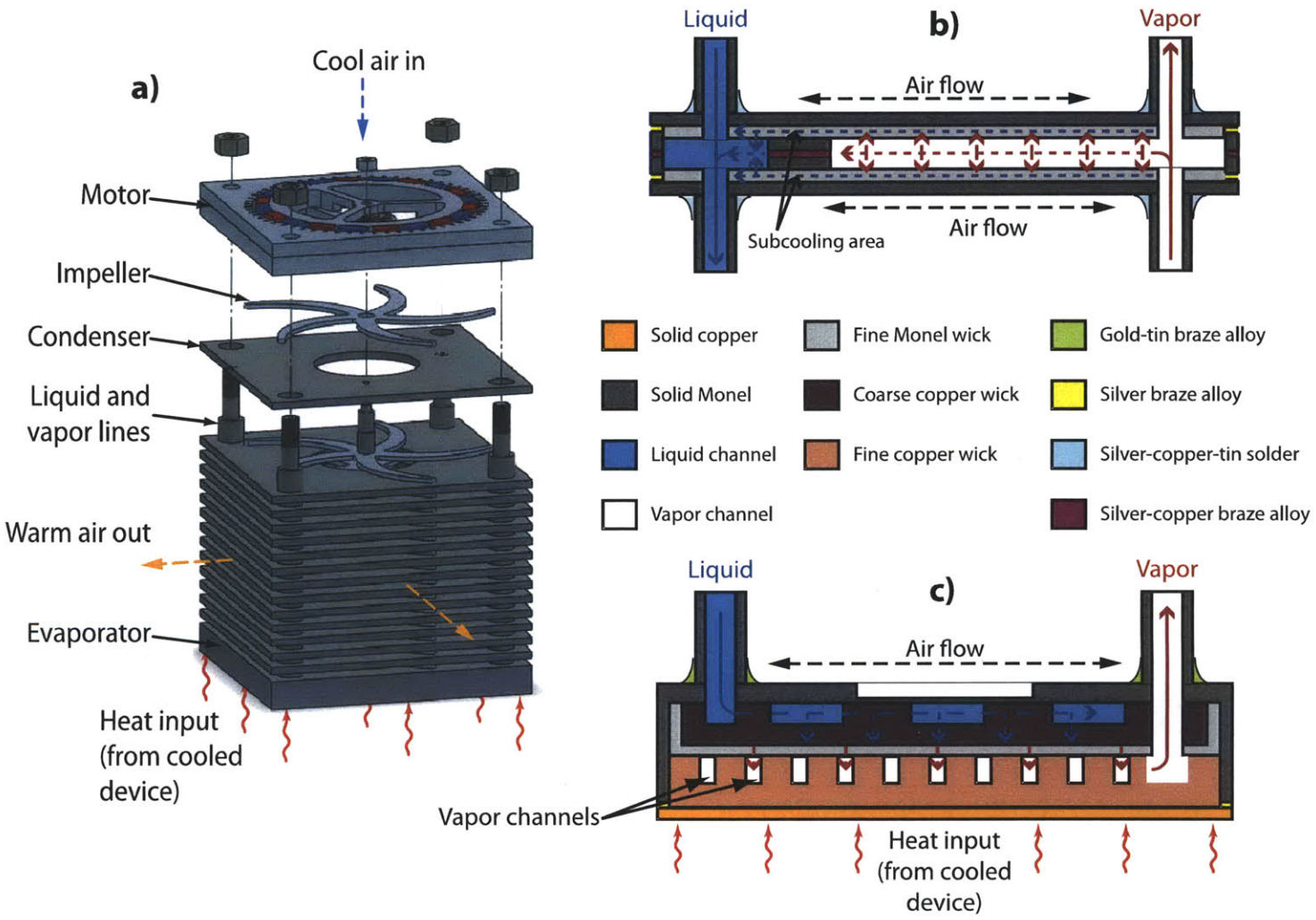

Figure 1.1: Schematic overview of PHUMP. **a)** Schematic drawing of PHUMP with labeled components. **b)** Schematic cross-sectional view of the interior of the condenser. **c)** Schematic cross-sectional view of interior of the evaporator.

heat transfer to the environment air is blown across the surfaces of the condensers by the interdigitated impellers. The rotating blades shear the thermal boundary layer off of the condensers, thereby decreasing the thermal resistance between the thermal stators and the ambient. The analysis of the air flow in this device, as well as the design of the impellers, is discussed by Allison [2]. The design and manufacture of the permanent-magnet motor are described in the work by Jenicek [24].

The evaporator and the condensers are connected by four pipes: two liquid and two vapor transport lines. The evaporator and condenser frames are sealed by brazing. The liquid and vapor lines are also brazed to the evaporator and the condensers.

1.3 Required Properties of the Wick Structure

The performance of a heat pipe is directly affected by the flow and thermal properties of its wick structure. This section presents a general discussion of the important properties of a wick and the way these properties are interrelated. Then, a more specific description of the properties required in the wicks of the evaporator and the condensers of PHUMP is presented. This description shows the need to balance conflicting properties in the condenser and evaporator wicks. Although PHUMP is a specific application of sintered wicks, the need to evaluate wick properties is common to all of the heat pipe based systems.

In heat pipe applications permeability, capillary pressure, thermal conductivity, mechanical strength and material compatibility are all important design parameters of the sintered wicks. The permeability of a medium is a measurement of the ease of fluid flow through it. At the same flow rate, a fluid traveling through a low permeability medium will experience a larger pressure drop than through a high permeability medium. In contrast to a low permeability medium, high permeability media have larger open spaces and hence fewer obstructions to fluid flow. Thus, the size (cross-sectional area and length) of the pores connecting the ends of the wick determines its

permeability and the pressure drop experienced by the fluid flowing through it.

Capillary pressure refers to the pressure difference across the interface between two fluids. The mathematical expression for this pressure difference is known as the Young-Laplace equation, given by

$$\Delta P = \gamma \left(\frac{1}{R_1} + \frac{1}{R_2} \right) \tag{1.1}$$

where ΔP is the capillary pressure across the interface or meniscus (the pressure in the concave side of the meniscus is higher); γ is the surface tension of the interface; and, R_1 and R_2 are the principal radii of curvature of the surface. Equation 1.1 shows that an interface with smaller radii of curvature can sustain a larger pressure difference. In a wick, the size of the pores determines the smallest radii of curvature of the menisci that can form in it. Thus, the capillary pressure that a wick can sustain depends on the size of the pores in the wick.

Thermal conductivity is a measurement of the ease with which heat is conducted through a material. Control over the thermal conductivity of a wick is desired in heat pipe design because it allows the wick to be used as a heat spreader (i.e. to make an area isothermal) or as an insulator. Because a sintered wick is a porous metal, the highest thermal conductivity that it can have is that of the solid (non-porous) metal. Numerous large voids in the wick effectively decrease its conductivity because of the lower thermal conductivity of air compared to the metal structure. Similarly, the mechanical strength of the wick decreases with a larger number and volume of pores in it.

The permeability, capillary pressure, thermal conductivity and mechanical strength of a wick are closely related to the number and size of pores in the wick. In some instances, it is possible to change one of these properties without negatively affecting the others at the same time. However, the opposite situation is commonly found in the design of heat pipe based systems. In many cases, desired characteristics of a wick

involve working with conflicting properties and the tradeoff between them has to be carefully evaluated. For example, capillary pressure is used to drive the working fluid through the system. As a consequence, it must balance the total viscous pressure drop in the system, which depends on the permeability of the wick. Nevertheless, as explained before, these properties are inversely related to the pore size in the wick. A small pore size is desired to increase the capillary pressure of the wick. However, decreasing the wick pore size also decreases its permeability, thereby increasing the pressure drop of the liquid as it travels through the wick. Thermal conductivity and flow properties are not independent from each other, either. A high thermal conductivity wick has to have low porosity, and as a consequence, it has high capillary pressure but low permeability and vice versa.

The need for specific and often conflicting properties of the wick structure calls for a flexible, controllable manufacturing process. For this reason, sintering of powdered metals was selected as the manufacturing process to fabricate the multiple wicks in PHUMP. Porous wicks can be formed with controlled properties by sintering powdered metals under different conditions, such as the sintering time and temperature.

Besides considering the flow and thermal properties of the wick, a requirement common to all of the components in PHUMP is that of material compatibility. Several authors [21, 45, 51] have studied hydrogen generation in heat pipes as a result of a chemical reaction between some metals and water. Hydrogen inside a heat pipe is a non-condensable gas that changes the pressure of the system, thereby changing its optimal operation point. In addition, non-condensable gases that collect over the cold condensation surfaces in the heat pipe impede the flow of the condensing gas. Hence, non-condensable hydrogen reduces the performance of the heat pipe. Gold, silver, copper and Monel^{TM} 400 (an alloy composed of 67% nickel and 23% copper) have been proven to generate no hydrogen when in contact with water [3, 46]. For this reason, copper and Monel 400 were selected as the manufacturing materials in PHUMP.

Finally, as part of the requirements set by DARPA, PHUMP has to be robust enough to sustain storage temperatures ranging from -54 °C to 100 °C. Then, the wick structure has to be able to sustain these extreme temperatures without a detrimental change in its properties.

1.3.1 Requirements in the Evaporator

One of the objectives of the wick in the evaporator is to drive the working fluid through the system. To draw the fluid from the condensers, the evaporator wick has to have a high capillary pressure, and thus, be of a fine pore size. In addition, the area inside the evaporator, where evaporation actually occurs, must be at uniform temperature so all of the evaporation area is used. To achieve this goal, a fine copper wick was selected for the evaporation area. The small pore size of this wick provides with the high capillary pressure used to move the liquid from the condensers to the evaporation area. Furthermore, the small pore size and the high thermal conductivity of copper ensure a vaporization area of uniform temperature, which is close to the temperature of the base of the evaporator due to the small thermal resistance of the wick.

However, using a fine pore wick has disadvantages as well. As previously discussed, a smaller pore size causes a large pressure drop in the working fluid moving through it. To reduce this pressure drop, vapor channels of large cross-sectional area are manufactured imbedded in the wick. The larger cross-sectional area of the channels compared to the wick pore substantially decreases the pressure drop of the vapor as it travels through them. A second disadvantage to fine wicks is the possibility of vaporization occurring at undesirable locations. A vapor bubble in the wick can obstruct the flow of the cold liquid coming from the condensers increasing the total pressure drop in the system. Thus, the rest of the evaporator has to be insulated from the nucleation area and from other high temperature spots in the system (e.g. vapor lines and the walls of the frame of the evaporator). This specification calls for a

layer of low thermal conductivity wick that shields the hot side of the evaporator from the rest of the component. The material selected for this wick is Monel, because its thermal conductivity is approximately 16 times lower than the conductivity of copper.

Figure 1.1**c** shows a schematic drawing of the design of the evaporator. The fine copper wick, shown with a light orange color, is the area where evaporation actually occurs. Vapor travels to the condensers via the vapor channels shown imbedded in this area. The vaporization area is insulated from the rest of the evaporator by a layer of Monel wick. In Figure 1.1**c** this Monel wick is represented by a thin gray layer just above the fine copper wick. To further reduce the possible formation of a vapor bubble above the Monel layer, a coarse copper wick is used to thermally connect this area with the top of the evaporator. The top of the evaporator is continually being cooled by one of the interdigitated impellers, thus the liquid side of the evaporator is actively being cooled. The relatively large pore size of the coarse copper wick decreases the pressure drop of the working fluid in this area.

1.3.2 Requirements in the Condenser

The wicking structure in the condensers is used to separate the liquid and vapor phases. In this manner, it is possible to set the pressure in the liquid and the vapor sides of the system independently from each other. In Figure 1.1**b**, vapor enters the condenser from the vapor lines, which connect the evaporator with the condensers. The pressure drop in the vapor due to viscous dissipation in the lines is negligible. Because of the small density of gas, the difference in the pressure of the vapor between the topmost condenser and the lowest condenser due to the gravity head is also negligible. However, this pressure difference is considerable for the liquid side. The meniscus in the condenser wick has to accommodate for this pressure difference to allow the same flow rate through all the condensers. The capillary pressure of the wick has to be able to sustain this pressure difference. The minimum capillary pressure required is 1 kPa for a 4" tall device. A capillary pressure of 1 kPa would be

enough to sustain the hydrostatic pressure of the column of water from the topmost condenser to the lowest one, but does not include a safety factor.

As the liquid travels through the sinter in the condenser to the liquid side of the system, it experiences a pressure drop. As explained before, the lower the permeability of the sinter, the higher the pressure drop in the liquid. However, the temperature of the liquid hardly drops below the saturation temperature as it stays in direct contact with the vapor in the condenser. Therefore, there exists a risk of forming a bubble of vapor in the liquid side of the system which would cavitate when it leaves the sinter and enters the (open) liquid line to the evaporator. To avoid cavitation in the liquid side of the system, the temperature of the liquid has to be decreased below the saturation temperature corresponding to the decreased pressure in the liquid (due to viscous pressure drop along the sinter). To achieve this reduction in temperature, the liquid is shielded from the vapor in the section labeled the 'subcooling area' in Figure 1.1**b**. The length of the subcooling area is related to the required temperature drop and hence it is related to the pressure drop experienced by the working fluid in the wick. If the pressure drop is larger, then the subcooling area has to be longer too, effectively decreasing the available area for condensation in the condenser.

The thermal conductivity of the wick in the condenser is also an important design parameter. The subcooling area has to be longer for a higher thermal conductivity wick, since the difference between the vapor temperature and the liquid temperature is lower for the same length of sinter. Therefore, a highly conductive wick in the condenser decreases the performance of the system because a larger portion of the condenser is dedicated to subcooling the liquid instead of condensing the working fluid. Although a low thermal conductivity wick also increases the resistance between the condensing vapor and the air flow outside the condenser, the wick is thin enough in this direction (0.5 mm) that its resistance becomes negligible compared to the convection resistance from the condenser outer surface to the air.

1.3.3 Requirements Due to the Manufacturing Process of the System

A critical process in the manufacturing of PHUMP is the brazing of all the components to achieve a vacuum seal in the system. Materials compatible with water-based heat pipes have high melting temperatures and thus, high brazing temperatures when used as filler metals. A desirable consequence of this high brazing temperature is that in general, the higher the melting temperature of the filler metal used, the higher the strength of the joint. However, common brazing temperatures for these materials and their alloys (from 270 °C up to 970 °C), fall in the range of temperatures used to sinter them. Additionally, many sintered wicks are exposed to multiple heating cycles as part of the manufacturing procedure of PHUMP. Then, it is important to define and characterize the impact, if any, of brazing in the properties of the sintered wick and ensure that any change in them will not have detrimental consequences on the performance of the system. For this reason, this section presents a general discussion of the construction process of PHUMP. It shows the need for multiple sintering steps for the wicks, some of them being sintered as much as four times. Details about the sintering procedures, as well as the properties of the wicks, are discussed in Chapter 2. Manufacturing of the impeller and the motor will not be addressed here, but can be found in the works by Allison [2] and by Jenicek [24].

Evaporator Manufacturing

The first step in the manufacturing of the evaporator is the machining of the Monel frame. This frame is shown in Figure 1.2**a**. Copper is sintered in graphite molds that create the vapor and liquid channels in the copper wick. These parts are called 'molded parts' since they are sintered first in a graphite mold and then sintered again inside the Monel frame. The vapor and liquid channels molded parts are shown in Figure 1.2**b** and 1.2**c**, respectively. This and all of the sintering and brazing process involved in the manufacturing of PHUMP are performed under a protective atmo-

sphere of 4% hydrogen, 96% nitrogen.

Due to manufacturing constrains, the sinter structure is built into the Monel frame starting from the fluid side. The first step is the attachment of the liquid channel wicking structure into the Monel frame. A fine layer of 10 μm copper powder between the molded part and the frame is used to bond these parts. A Monel powder layer is placed on top of the molded part. This Monel layer is sintered to create the thermally insulating layer. Then, the vapor channel molded part is placed on top of the sintered Monel layer and attached to the rest of the system with a thin layer of 10 μm copper powder between the Monel insulating wick and the molded part. A second sintering process is used here to bond the multiple layers of the internal structure of the evaporator. Then, the solid copper lid (which will be the base of the complete evaporator) is attached by sintering another thin layer of 10 μm copper powder between the vapor channel molded part and the copper lid. Finally, the copper plate and the Monel frame are sealed using Tungsten Inert Gas (TIG) welding.

Figure 1.2**g** shows a labeled schematic cross-sectional view of the finished evaporator. The Monel frame and the fine and coarse copper wicks are identified in the drawing.

Condenser Manufacturing

The condenser frame plates and the 'subcooling inserts' are chemically etched from a 0.020" thick sheet of Monel. The frame plates and the subcooling inserts are shown in Figure 1.2**d** and 1.2**e**, respectively. The attachment of these two parts is achieved by means of silver brazing at 970 °C for 12 minutes. The result is a half condenser frame as shown in Figure 1.2**f**.

The space between the subcooling area and the frame plate is filled with Monel powder. After this powder is sintered, two condenser halves are brazed together us-

ing a 0.002" thick 72% Ag, 28% Cu braze sheet cut to match the condenser profile. Brazing occurs at 720 °C for 12 minutes.

Figure 1.2**h** shows a schematic cross-sectional view of the finished condenser. The condenser frame plate and the subcooling insert are labeled in this figure.

Integration of PHUMP

The condensers are aligned in a jig and 0.375" ID rings of a 60% Ag, 30% Cu, 10% Sn braze alloy are placed around each of the vapor and liquid line joints (eight per condenser). Then, the vapor and liquid lines are slid through each condenser. This setup is heated to 740 °C for 12 minutes to melt the brazing alloy. This stack of condensers is placed on top of the evaporator and brazed to it at 320 °C for 12 minutes with a 80% Au, 20% Sn brazing alloy. Once the heat pipe is filled with degassed, distilled water, the heat pipe is sealed using a crimping tool. Finally, the impellers are attached as discussed in the work by Allison [2].

1.4 Literature Review

Several authors have measured the permeability, maximum capillary pressure and/or thermal conductivity of sintered metal wicks. Singh et al. [53] described many simple experimental methods to measure permeability, capillary pressure and thermal conductivity of water-saturated copper and polyethylene wicks. The principles of their experimental methodology are the same as the ones used in the present work and described in Chapter 2. Semenic et al. [52] measured the same properties for copper wicks with particle diameters in the ranges of 52-63 μm, 63-75 μm, 63-90 μm, 75-90 μm and 90-106 μm. The maximum capillary pressure they measured was found to be linear (with negative slope) with average particle size. The particle size range with the smallest particles, 52-63 μm, had a measured maximum capillary pressure of 12 kPa, while the largest particles, 90-106 μm, had an 8.5 kPa maximum capillary

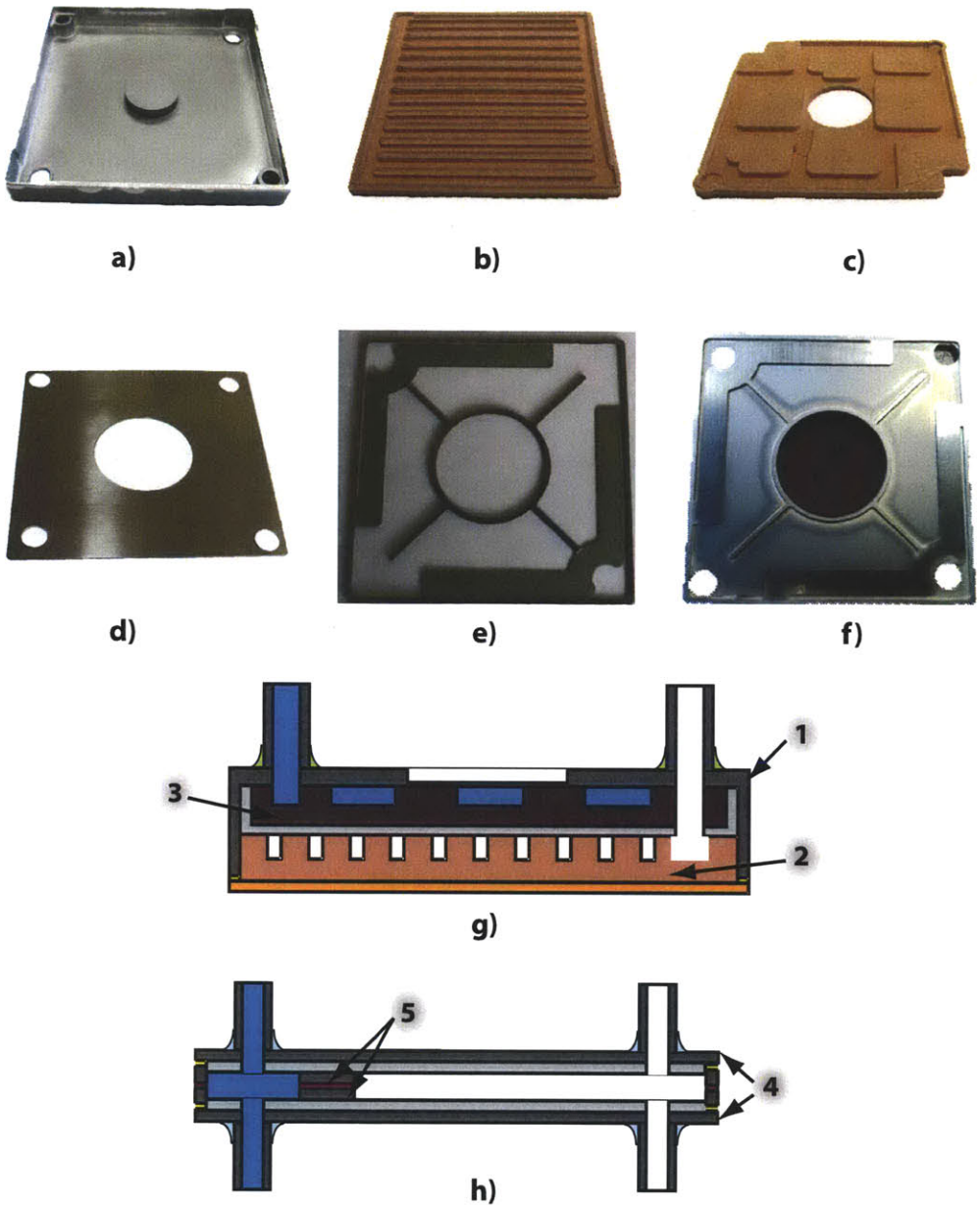

Figure 1.2: **a)** Machined Monel frame for the evaporator. **b)** Vapor channel molded part (10 μm copper powder). **c)** Liquid channel molded part (38-75 μm copper powder). **d)** Condenser frame plate. **e)** Subcooling insert of the condenser. **f)** Half of a condenser frame after silver brazing. **g)** Schematic cross-sectional view of the finished evaporator. The point labeled '1' shows the Monel frame (**a**), '2' shows the fine copper molded part (**b**), and '3' shows the coarse copper molded part (**c**). **h)** Schematic cross-sectional view of the finished condenser. The point labeled '4' shows the Monel frame plates (**d**), '5' shows the subcooling inserts (**e**).

pressure. Similarly, water permeability of the samples was found to be a linear function (with positive slope) of the average particle size, ranging from 1.5×10^{-12} m^2 for the smallest particles, down to 2.4×10^{-12} m^2 for the largest particles. Thermal conductivity of all the samples was very similar with an average of 142±3 W/m-K. The authors do not discuss the sintering parameters of fabrication of their samples.

Thermal conductivity of porous material has been an active area of research since the late 1800s. Peterson et al. [44] presented a summary of diverse expressions proposed to calculate the thermal conductivity of a porous material based on its porosity. Then, they compared these expressions with experimental values of their own and showed that all of the existing models are valid only in a very limited range of porosities. More recently, Atabaki et al. [5] performed a similar literature survey of expressions, finding the same problem as Peterson et al. Birnboim et al. [8] proposed a model based on two touching spheres as a unit cell used to predict thermal conductivity of a porous material. The authors assumed that the unit cell thermal conductivity is that of unit cell. Dan et al. [13], Devpura et al. [16], Ganapathy et al. [20] and Kanuparti et al. [25, 26], included the spatial connections between the high conductivity component imbedded in a low conductivity component by generating a random network of thermal resistors and then solving for its thermal conductivity. A similar model is used in this thesis and is described in Chapter 4.

Several authors [28, 56, 60] have studied the coalescence of two spherical particles (or a group of spheres) by surface diffusion, grain boundary diffusion and/or a combination of these mechanism. Missiaen [36] reviewed some of the major contributions to the modeling of sintering. Some authors have shown that, despite the many simplifications of the two-particle model, its predictions are fairly close to more complete and thus complicated models [28, 56]. The two-sphere model is described in Chapter 3.

1.5 Thesis Overview

This thesis focuses on the properties of the sintered wick inside the heat pipe described above. Chapter 2 describes the sintering process followed for the diverse wicks considered in this work. Additionally, the methodology of the measurements and the values of thermal conductivity, water permeability and maximum capillary pressure measured are presented in this chapter. Chapter 3 explains the fundamental principles of sintering, applies them to the two-sphere model and relates the values calculated for the neck size and shrinkage with the experimental measurements. Chapter 4 explains the model developed for thermal conductivity, including the unit cell approach and its inclusion in a 3D random thermal resistor network. The results of this model are compared to the experimentally measured thermal conductivities. Conclusions of this thesis are presented in Chapter 5.

Chapter 2

Experimental Measurements

This chapter shows the results of measurements performed on copper and Monel 400 sintered wicks. Shrinkage, thermal conductivity, permeability and capillary pressure are the properties measured as a function of the wick's particle size, sintering time and temperature. First, the process followed to prepare the sintered wick samples is presented. Then, the methodology followed to measure each property is discussed. The results of these measurements are presented and discussed. Additionally, the effect of multiple sintering procedures on the wick's properties is investigated. Finally, a test designed to assess the robustness of PHUMP when subjected to extreme storage temperatures is described and its results are discussed.

2.1 Sample Preparation

2.1.1 Powder Material and Particle Size

As mentioned in Chapter 1, copper and Monel were the materials selected for the sintered wicks in PHUMP. A fine powder was selected for the sections of the system where high capillary pressure was required and a large particle size was used elsewhere to control the liquid-vapor interface and thermal conductivity without inducing significant pressure drops. Given its lower thermal conductivity, Monel 400 was used instead of copper where a layer of thermal insulation was required. Copper

Table 2.1: Chemical composition of the metal powders

	Composition [%]			
Chemical	Copper 10 μm	Copper 38-106 μm	Monel -33 μm (spherical)	Monel -44 μm (non-spherical)
Cu	Balance	Balance	30-40	28
Ni	0.002	-	Balance	Balance
Ag	0.002	-	-	-
C	0.006	-	-	-
Fe	0.002 (max)	-	-	3
O_2	0.52	0.05 (max)	-	-
Si	0.003	-	0.5 (max)	-
Zn	0.002 (max)	-	-	-
Al	0.001 (max)	-	-	-
Pb	0.002 (max)	-	-	-
Sn	0.002 (max)	-	-	-
Mn	-	-	0.5 (max)	2

was used whenever an isothermal section was desired in the heat pipe. A summary of the compositions of the powders used in this work is shown in Table 2.1. The copper powder was supplied by Alfa Aesar [1], while the Monel was bought from Sandvik Osprey [33]. These powders were confirmed to be spherical using a scanning electron microscope. Non-spherical Monel powder was used in the multiple sintering procedure tests. This powder was supplied by Atlantic Equipment Engineers [17].

Three different particle size ranges were selected for each metal and sieved from the powder batches shown in Table 2.1. For copper, 10 μm, 38-75 μm and 75-106 μm were the ranges considered. For Monel, the size ranges were -22 μm, 22-33 μm and -33 μm. Following the convention used for mesh sizes, a '-' in front of a number means that every particle below that particle size is included in the range.

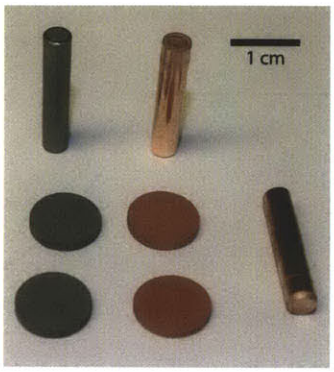

Figure 2.1: Picture of copper and Monel disk and tube samples.

2.1.2 Sintering Procedure

Two different types of samples were prepared. For the thermal conductivity tests, metal powder was poured into a graphite mold. The graphite mold contained right-circular cylindrical cavities 2.5 mm deep and 12.3 mm, 14.3 mm or 15.8 mm in diameter. These dimensions were selected to match the size of the sample holders of the laser flash machine used to measure thermal conductivity. For permeability and capillary pressure tests, powder was sintered inside 4.5 mm ID tubes. The height of the sintered plugs inside the tubes was approximately 30 mm. The samples were shaken for 5 minutes using an electric shaker table. The material of the tubes and the sinter was the same. Figure 2.1 shows examples of some of the samples prepared.

After the samples were prepared, they were loaded in a tube furnace. A Lindberg-Blue [32], 1.5 m long, 15 cm OD tube furnace was used to sinter the samples. To avoid oxidation of the samples a protective atmosphere was used during sintering. First, pure nitrogen was used to purge the furnace tube. The nitrogen was allowed to flow for at least 1.5 hours. This purge time allows some of the oxygen to diffuse out of the pores between powder particles. Once the nitrogen purging was finished, nitrogen flow was stopped and then forming gas was used as the protective atmosphere. The composition of forming gas used is 4% hydrogen, 96% nitrogen. At the same time that the forming gas flow was started, the sintering process was started.

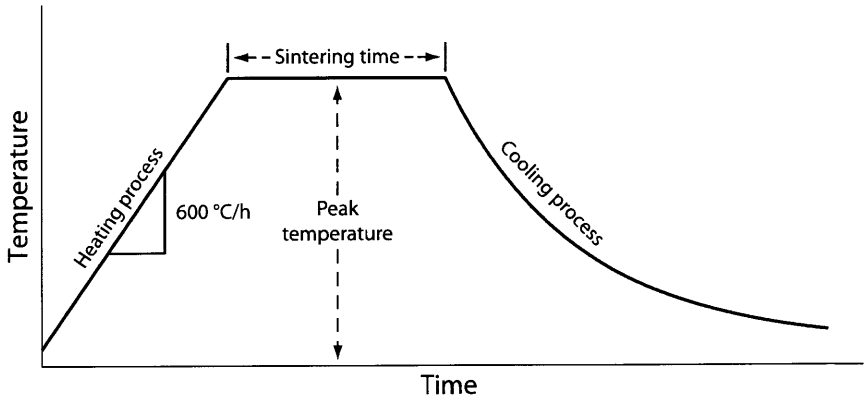

Figure 2.2: Time-temperature plot of the sintering process. All the samples were heated at 600 °C/h to reach the peak sintering temperature. The samples stayed at the peak temperature for different periods of time. The cooling of the samples followed the cooling of the furnace.

Figure 2.2 shows a time-temperature plot of the sintering process followed in this work. First, a heating ramp rate of 600 °C/h was used to reach the peak sintering temperature. The peak sintering temperatures were varied, with values of 450 °C, 550 °C, 650 °C, 750 °C, 850 °C and 950 °C. Depending on the specifics of the test run, the furnace was held at the peak sintering temperature for different periods of time (referred as 'sintering time' in Figure 2.2). These periods were 0 minutes (cooling of the sample started as soon as the furnace reached the peak temperature), 15 minutes, 45 minutes, 90 minutes and 180 minutes. Once sintering was finished, the sinter was cooled inside the furnace, while maintaining the flow of forming gas. When the furnace reached a temperature bellow 200 °C, the forming gas flow was stopped and switched back to pure nitrogen. Nitrogen flow was stopped once the sinter reached room temperature. Figure 2.3 shows the temperature profile of the furnace as it cools. In this thesis both the heating and cooling processes are included in the analysis, so a distinction is made between the overall sintering process (which includes the heating and cooling time) and the isothermal sintering process, which is the time that the samples spent at the peak temperature.

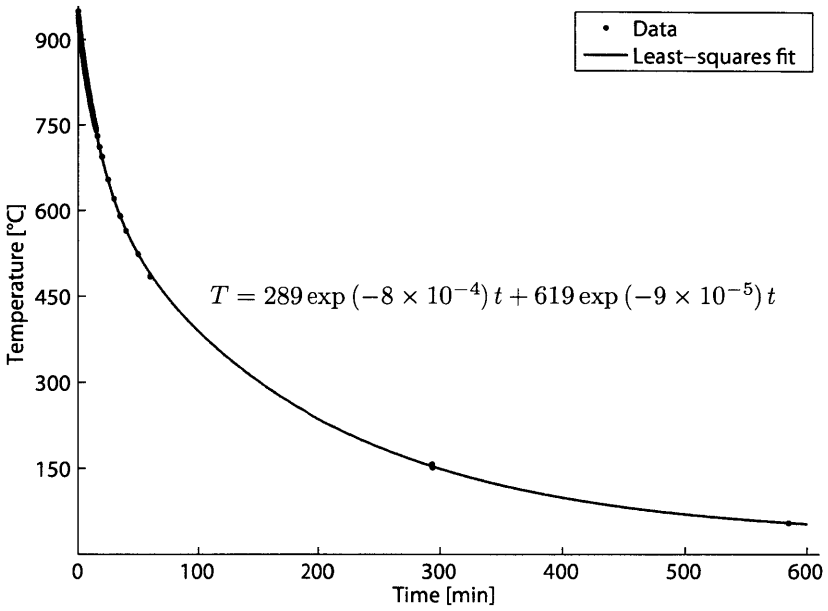

Figure 2.3: Temperature profile of the furnace as it cools. Equation of the least-squares fit for the furnace temperature, T, as a function of time, t, is also shown. Data points were taken using the same gas flow rates used to fabricate all the samples.

Copper 10 μm powder sintered for all peak temperatures and hold times considered in this thesis. 'Sintered' means that particles bonded together with enough strength to keep the shape of the wick even when gently tapped with a finger. Copper 38-75 μm and copper 75-106 μm samples held their shape only when the sintering temperature was above 650 °C. Even at this temperature, for hold times less than 45 minutes, some particles detached from the rest of the wick when gently tapped. Although thermophysical property results are shown for these samples, it is recommended that these size ranges are sintered at 750 °C or above. Spherical Monel powder sintered with structural rigidity at a minimum temperature of 850 °C and hold time of 90 minutes. However, non-spherical Monel first sintered at 820 °C for 15 minutes.

2.2 Geometric Measurements

Densification is an important characteristic of sintered objects. Densification refers to the reduction in the size and number of pores in a sintered object. As the number

and size of pores in a sintered wick decreases, its size also decreases. The change in dimensions of the disk samples due to sintering was measured and used to calculate the linear shrinkage and the porosity of the samples. The results of these measurements are shown in Figure 2.4 and Figure 2.5. Figure 2.4 shows the linear shrinkage (as a percentage) of the sintered disks as a function of holding time and peak temperature. Linear shrinkage was measured as the change in the diameter of the sintered disk samples as

$$\epsilon = \frac{\Delta D}{D_0} \tag{2.1}$$

where ϵ is the linear shrinkage of a sample; D_0 is the diameter of the sample before sintering (the diameter of the sample at room temperature); and, ΔD is the change in its diameter after sintering (measured at room temperature). A Tresna [57] caliper was used to measure the diameter of the samples. The uncertainty of the measured shrinkage was estimated at $\pm 1.0\%$. It is important to mention that in this work, shrinkage is measured based on the diameter of the sample at room temperature. As the sample is heated to the peak sintering temperature, both the graphite mold and the metal powder will expand. However, the thermal expansion coefficient of the graphite mold is lower than the thermal expansion of either copper or Monel. Thus, the mold limits the expansion of the sintering powder. This effect and its impact on the measurements of shrinkage measurements performed in this thesis are discussed in the next section. This effect is accounted for in the error bars in Figure 2.4. For this reason, the error bars at the higher temperatures (650 °C and above) are asymmetric.

Figure 2.5 shows the porosity (as a percentage) of the sintered disks as a function of holding time and peak temperature. The porosity of the samples is calculated as

$$\phi = 1 - \frac{\rho_{\text{wick}}}{\rho_{\text{material}}} \tag{2.2}$$

where ϕ is the porosity of a sample; ρ_{wick} is the density of the sintered sample; and, ρ_{material} is the mass of the non-porous metal. The density of the porous sample was calculated by dividing the mass of the sample by its volume. The mass of the sample

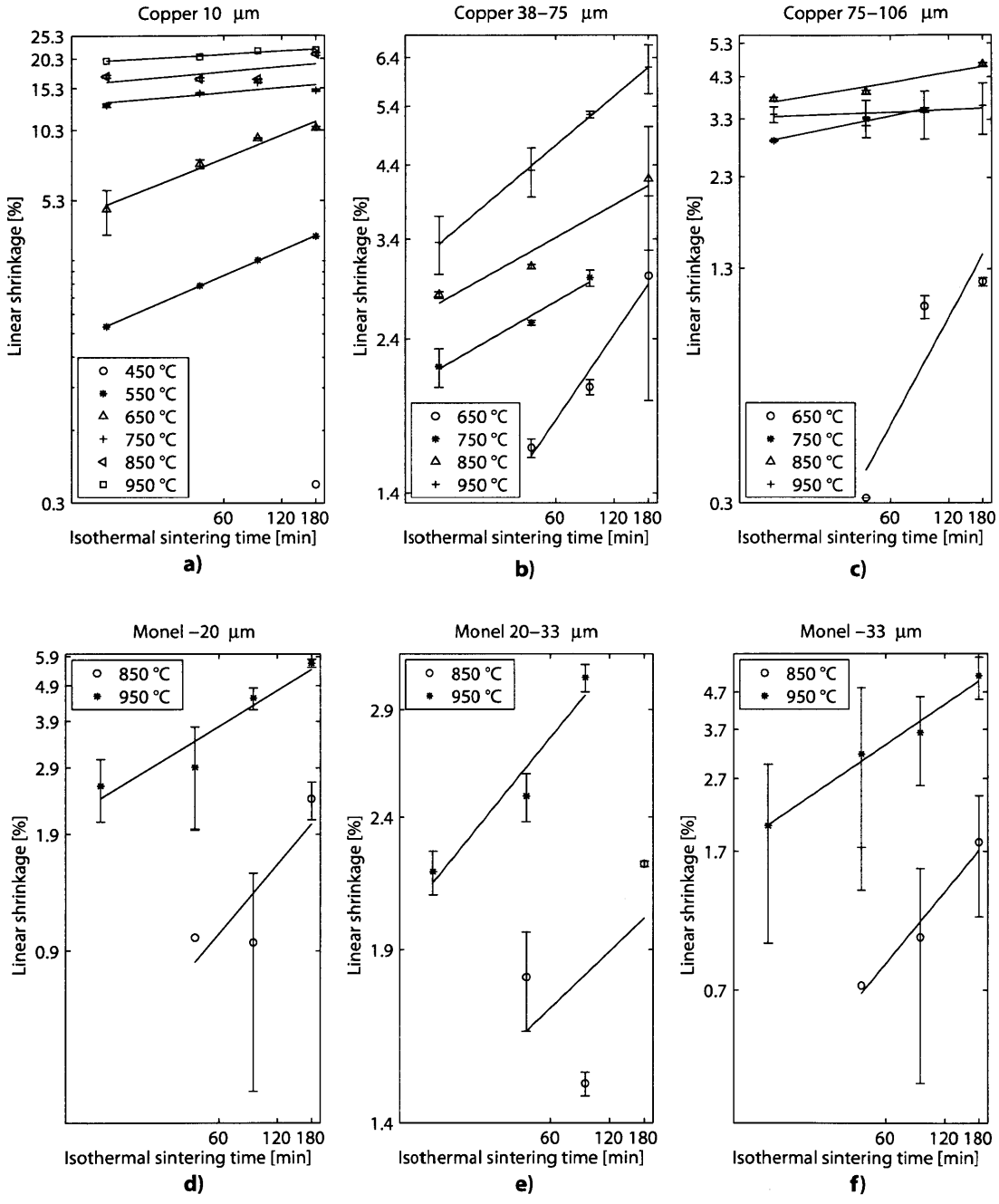

Figure 2.4: Sample densification expressed as linear shrinkage of the diameter of the sample for **a)** copper 10 μm, **b)** copper 38-75 μm, **c)** copper 75-106 μm, **d)** Monel -22 μm, **e)** Monel 22-33 μm, and **f)** Monel -33 μm sintered wicks. The effect of the mismatch between the thermal expansion of the graphite mold and the metal powders is shown as asymmetric error bars. Detail about this effect can be found in the next section of this work.

was measured using a Sartorius [49] digital weighting balance. The uncertainty of the measured porosity was estimated at $\pm 1.0\%$.

As expected, the higher the sintering temperature and the longer the sintering time, the larger the shrinkage of a sample. It can also be seen that at low temperatures the samples shrank rapidly, but the rate of densification decreased at higher temperatures. The fact that the data points follow a linear trend in a log-log plot confirms the characteristic power-law behavior of densification as a function of sintering time [18]. A similar trend was obtained for the porosity of the samples. Nevertheless, porosity did not change appreciably for 38-75 μm and 75-106 μm copper samples at 650 °C and 750 °C, which could be attributed to the fact that these were the temperatures where the samples were barely sintered to keep their shape. At these relatively low sintering temperatures, changes in shrinkage were too small to be discernible.

In the case of the tube samples, the metal powder bonds to itself as well as to the tube wall. The bonds between the wall and the sinter inhibited shrinkage of the samples for the lower peak sintering temperatures. When the sintering temperature was large enough, separation of the wick from the pipe walls happened in some locations. This was the case for the copper 10 μm samples, where separation occurred when sintered at 650 °C or above. Separation began as early as 820 °C in some of the Monel samples. Taking into account this separation is important when selecting a sintering procedure, because a gap between the wick and its container larger than the largest continuous pore in the sinter will decrease the maximum capillary pressure the wick can sustain. Figure 2.6 shows an example of a gap between the tube wall and the sinter observed under an optical microscope.

2.2.1 Effect of Graphite Mold on Shrinkage Measurements

For this work shrinkage was measured for a powder that is constrained by a graphite mold as it sinters. The mold has a lower thermal expansion coefficient than either

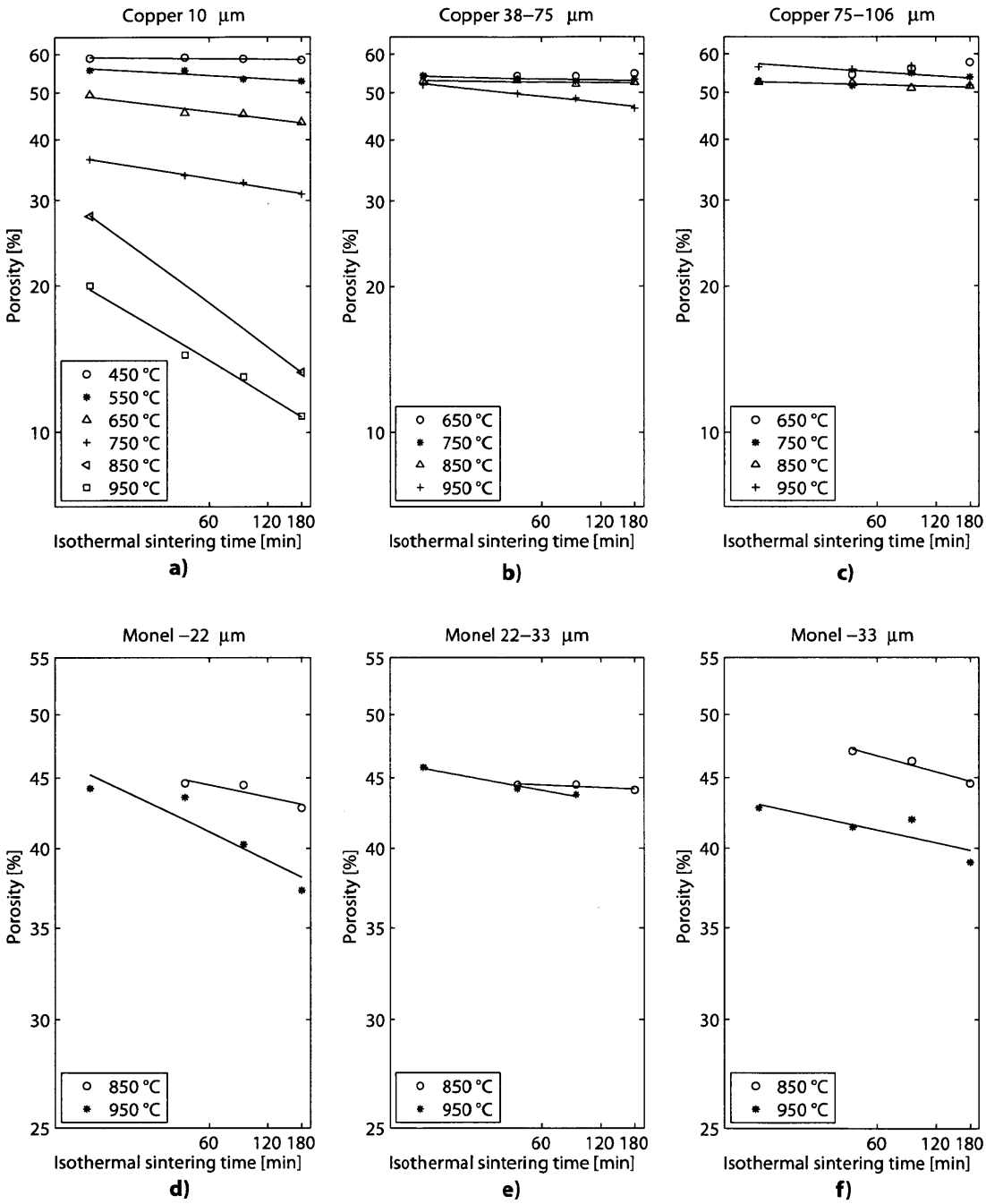

Figure 2.5: Sample densification expressed as porosity for **a)** copper 10 μm; **b)** copper 38-75 μm; **c)** copper 75-106 μm; **d)** Monel -22 μm; **e)** Monel 22-33 μm; and, **f)** Monel -33 μm samples.

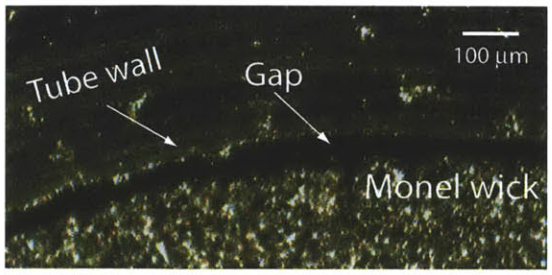

Figure 2.6: Separation of non-spherical Monel sintered wick from the wall of a Monel tube. The sample was sintered at 820 °C for 15 minutes.

copper or Monel. Thus, as the temperature increases, the mold limits the expansion of the sintering powder. The thermal expansion of graphite is anisotropic, with a coefficient of 7.5×10^{-7} °C^{-1} parallel to the grain and 2.7×10^{-5} °C^{-1} perpendicular to the grain [58]. Based on the minimum thermal expansion coefficient, the change in the diameter of the 15.8 mm mold is approximately 10 μm when heated to 950 °C. This change in dimension is less than the uncertainty of the measurement of the diameter of the samples, which is approximately ± 0.04 mm. Thus, within the uncertainty of the measurement, the graphite mold does not expand during the sintering of the samples. Therefore, the metal particles of the samples are constrained by the graphite mold and may rearrange to accommodate the thermal expansion of the metal. Assuming that the particles can freely rearrange themselves to accommodate for the difference in the thermal expansion until the peak temperature is reached, and neglecting the shrinkage derived from sintering, the resulting samples would have a smaller diameter at room temperature after the sintering process, because their diameter at the higher temperature is smaller than the diameter of a sinter that is not constrained by the mold. Table 2.2 gives the calculated results for the starting diameter (i.e. an effective diameter) of an unconstrained copper sample that would result in the same final diameter as a constrained sample, assuming both constrained and unconstrained samples are subject to the same thermal history. In generating Table 2.2 the thermal expansion coefficients of the copper sinters are assumed to be the same as that of solid copper.

Table 2.2: Effective room temperature diameter of sinter after rearrangement due to graphite mold constraints

Peak sintering temperature	Actual starting diameter of sinter at room temperature	Effective diameter at room temperature due to rearrangement
450 °C	15.8 mm	15.69 mm
550 °C	15.8 mm	15.66 mm
650 °C	15.8 mm	15.64 mm
750 °C	15.8 mm	15.61 mm
850 °C	15.8 mm	15.59 mm
950 °C	15.8 mm	15.56 mm

At the lower sintering temperatures (all of the 450 °C and 550 °C samples, as well as the samples sintered at 650 °C for 0 and 15 minutes) the change in diameter due to thermal expansion effects is on par with the measured shrinkage. Thus, at low temperatures, this effect could account for much of the measured shrinkages. At 450 °C, the shrinkage due to this thermal expansion effect is 0.7%, compared to the measured shrinkages that are all below 0.4%. A similar situation is found at 550 °C and at 650 ° for sintering times of 0 minutes and 15 minutes. In these cases, the shrinkage expected due to thermal expansion is larger than the shrinkage measured based on the diameter of the mold. This behavior suggests that the effect of thermal expansion is overestimated. As the sintering temperature increases, the effect of shrinkage due to sintering becomes more important, thus the effect of shrinkage due to thermal expansion effects becomes smaller than the shrinkage derived from sintering. The difference between the shrinkage calculated assuming the initial diameter is that of the graphite mold at room temperature, and the shrinkage calculated assuming that the initial diameter is the effective diameter shown in Table 2.2 is at most 10%. Using the diameter of the mold instead of the diameter of Table 2.2 results in a systematic overestimation of the shrinkage.

The effect of the graphite mold constraints results in a systematic deviation of the measured shrinkage. At low sintering temperatures (450 °C and 550 °C samples, as well as the samples sintered at 650 °C for 0 and 15 minutes), this systematic error could account for the observed shrinkages in the samples. At higher temperatures, the overestimation is at most 10%. To account for this overestimation, the error bars in Figure 2.4 were adjusted to show the possibility that the actual measurement of shrinkage is 10% below the average value reported at the higher sintering temperatures. This change in the error bars was not made for the lower sintering temperatures, where the data uncertainty could be as large as 100%.

It is important to mention that the 10% systematic deviation discussed in this section was calculation using the smallest thermal expansion coefficient of graphite. In addition, since connections begin to form between the particles during the ramping process, these connections will cause some shrinkage of the samples even during ramping that will inhibit the rearrangement of the particles. It is possible that some of the thermal expansion mismatch generate internal stresses instead of the displacement of the particles. Therefore, the simple model used to estimate the effect of the thermal expansion mismatch between the mold and the metal powder is expected to be an upper bound on the measured shrinkages. Finally, because the molded parts used during the manufacturing of PHUMP are sintered in graphite molds, the definition of shrinkage used here is based on the diameter of the graphite mold at room temperature. In this manner, the final dimension of the molded part is easily calculated using the results generated in this work.

2.3 Thermal Conductivity Measurements

Thermal conductivity of the samples was measured using a NETZSCH-Gerätebau [37] Microflash laser flash apparatus. The laser flash technique was first proposed as an accurate experimental measurement of the thermal diffusivity of small, thin samples. The laser flash apparatus has been suggested as an accurate measurement

of the thermal conductivity of sintered samples [12]. This technique is based on the temperature evolution of the rear surface of the sample after a pulse of radiant thermal energy is uniformly shot at the front surface [41]. A simple relation for the thermal diffusivity of the sample, α is given by [41]

$$\alpha = \frac{1.38\, d^2}{\pi^2\, t_{1/2}} \tag{2.3}$$

where d is the thickness of the sample; and, $t_{1/2}$ is the time required for the rear surface to reach half the value of its maximum temperature rise. The heat capacity of the sample, mc_p, is obtained by comparing its thermal response with that of a reference sample for which properties are known. This reference sample (and the value of its properties) is supplied by NETZSCH-Gerätebau. For the present work, thermal conductivity was measured at least five times for each sample. Each fabrication condition (sintering time-temperature profile) had three samples. The results of the measurements are shown in Figure 2.7. In this and all the plots in this thesis, the error bars represent the standard deviation of the measurements.

In general, the thermal conductivity increased as the sintering temperature and/or time increased, but only the 10 μm copper samples have a regular pattern. Some of the measurements for the larger particle copper samples and Monel samples showed an anomalous decrease in thermal conductivity with an increase in sintering time. This behavior can be attributed to the lack of a uniform particle size in these cases. If two large particles of similar size are in direct contact, then the growth of the neck connecting them will ultimately be limited by the size of the spheres. On the other hand, if those spheres are not in direct contact, but connected through a chain of smaller particles, then the size of the connection between the larger spheres will be limited by the size of the smaller ones. The neck between the small particles will stop growing once it reaches a size approximately equal to that of the particles. It is not until shrinkage of the sample allows the two large particles to touch each other that the connection between them can continue to grow. In samples with a larger particle

size range the heat flow path has random length due to the tortuosity of the sample, but also the cross-sectional area of this path depends on the position and size of the particles in the sinter.

2.4 Water Flow Measurements

The experimental setup used to measure permeability and capillary pressure of the wicks is schematically shown in Figure 2.8. An upstream tank was pressurized with nitrogen and used to drive water through a filter, a volume flow meter [50], a pressure transducer [4] and the sample itself. The filter used was rated for 5 μm particles, as a means to avoid clogging the sinter with solid impurities suspended in the water. The pressure of the tank was controlled by means of a gas pressure regulator [39]. Both volume flow and pressure drop across the sinter were recorded and used to compute the permeability and capillary pressure of the sinter samples. The pressure transducer was located near the sample so that the measurement is not affected by the pressure drop in the valves and in the volume flow meter. The maximum pressure drop due to viscous flow in the lines and due to the meniscus before the pressure transducer was estimated at 100 Pa, which is less than 4% of the minimum pressure read in the transducer during the measurements.

Water was flushed through the sample for 10 minutes before beginning the measurements to remove any air bubbles trapped in the wick. For each measurement, readings of the volume flow meter and pressure transducer were recorded and used to calculate the permeability, κ, according to Darcy's law

$$\kappa = \frac{\ell\mu}{A_{cs}\rho}\left|\frac{\mathrm{d}\dot{m}}{\mathrm{d}P}\right| \tag{2.4}$$

where ℓ is the length of the wick; μ is the viscosity of water; A_{cs} is the cross-sectional area of the sinter; ρ is the density of water; and, $\dot{m}$ is the mass flow rate resulting from a pressure drop of P across the wick. Each sample was measured three times,

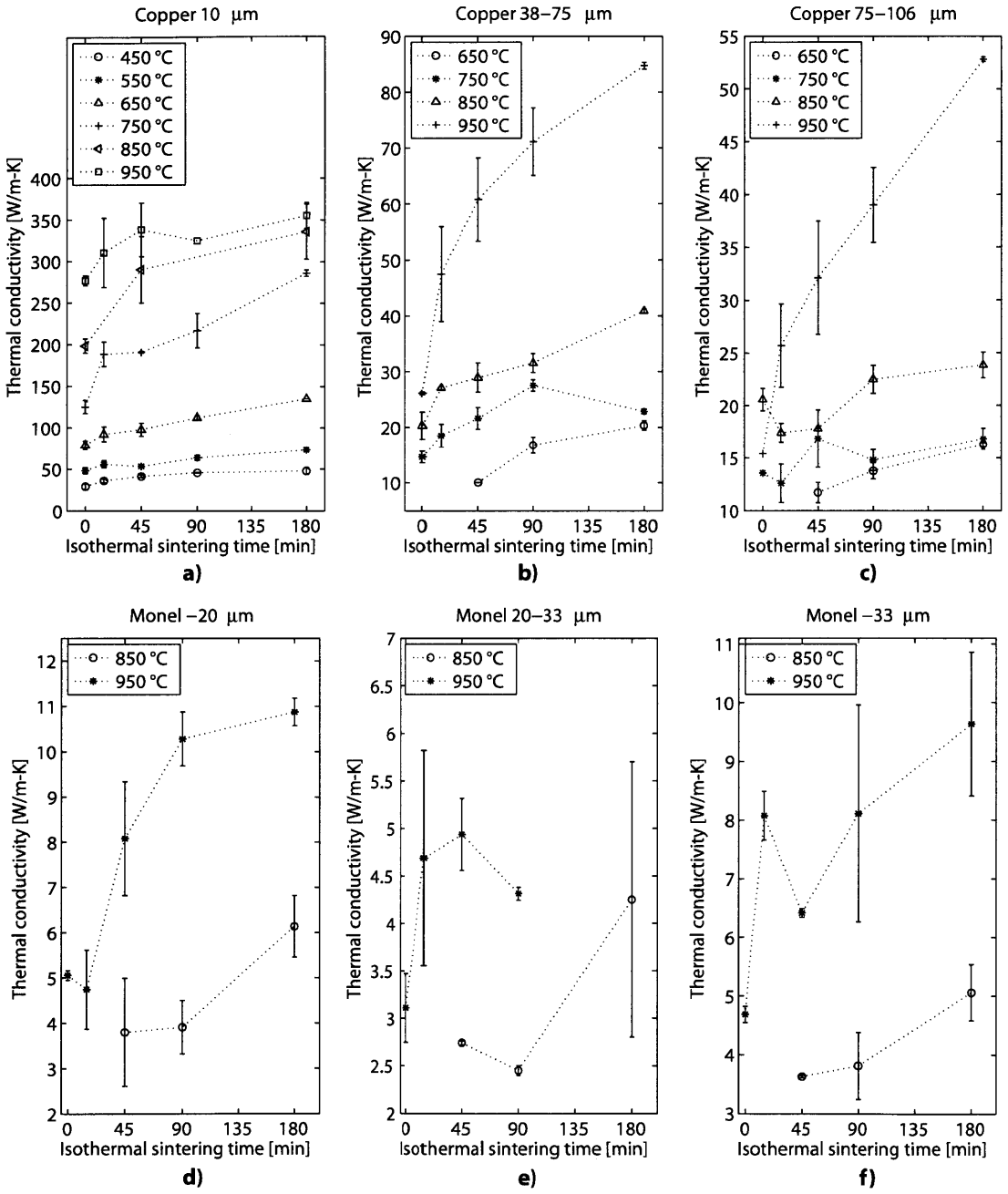

Figure 2.7: Thermal conductivity of the sintered wicks as a function of the isothermal sintering time. **a)** Copper 10 μm. **b)** Copper 38-75 μm. **c)** Copper 75-106 μm. **d)** Monel -22 μm. **e)** Monel 22-33 μm. **f)** Monel -33 μm.

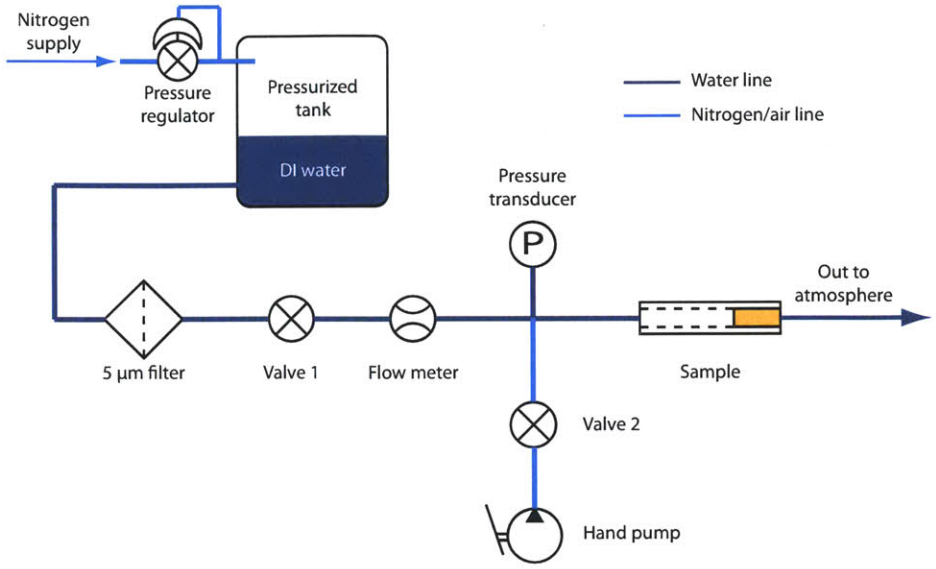

Figure 2.8: Apparatus used to measure permeability and maximum capillary pressure of the samples. The tank was pressurized with nitrogen and used to drive the flow through the system. The pressure drop in the sample was measured using a pressure transducer just upstream of the sample. The pressure downstream of the wick was assumed to be atmospheric. Viscous pressure drop from the pressure transducer to the wick was neglected.

and three different samples were measured for each fabrication condition (pairs of sintering time and temperature).

Results of the measurements are shown in Figure 2.9. For the three size ranges of copper, the average permeability increased with particle size. The permeability varied in a small range of values, but a clear trend with time or temperature was not seen for the fabrication conditions considered. This variation suggests that the random structure of the wicks has a larger effect on the flow properties of the samples than the sintering parameters. It is important to mention that shrinkage impeded measurements when a gap between the tube walls and the sinter formed (e.g. 10 μm samples above 650 °C). Increasing values of permeability and decreasing capillary pressure were measured (not shown), but these measurements are probably strongly affected by the gap between the sinter and the wall.

The same apparatus as shown in Figure 2.8 was used to measure the maximum capillary pressure that the wicks can sustain. The methodology used is as follows. First, the sinter and liquid line were flooded with water. Then, with valve 1 closed and 2 open, an air bubble was introduced in the line upstream of the wick using a hand pump. Then, valve 2 was closed and valve 1 was opened. The pressure in the tank was incremented to approximately 5 kPa. The bubble was pushed through the line until it reached the sinter and stopped due to the formation of many small menisci at the sinter surface. At this point, the mass flow reading quickly decreased to zero and the pressure reading slowly increased. Pressure in the upstream tank was then gradually increased until the pressure at the transducer decreased and the flow rate increased again, both of which are signs that the bubble had penetrated the porous wick. The maximum pressure read from the transducer was recorded as the maximum capillary pressure for the sinter. Each fabrication condition (sintering time-temperature profile) had three samples and each sample was measured at least two times, though most measurements were repeated five times. The results of this measurement are shown in Figure 2.10.

For copper, maximum capillary pressure followed the same trend as permeability, staying constant for the manufacturing conditions considered. Figure 2.10**a** shows that capillary pressure for copper 10 μm sintered at 650 °C is lower than in the 450 °C and 550 °C samples. This behavior can be explained in terms of shrinkage. The bulk of the sinter itself has a maximum capillary pressure as large as (or larger than) the lower temperature cases, but the gap between sinter and container becomes larger than the largest pore size in the wick, and thus dominates the measurement of capillary pressure.

Monel samples showed a larger variability in the capillary pressure than the copper samples did. Even samples prepared under the same conditions had markedly different capillary pressures. For some of the samples a gap between the walls of the

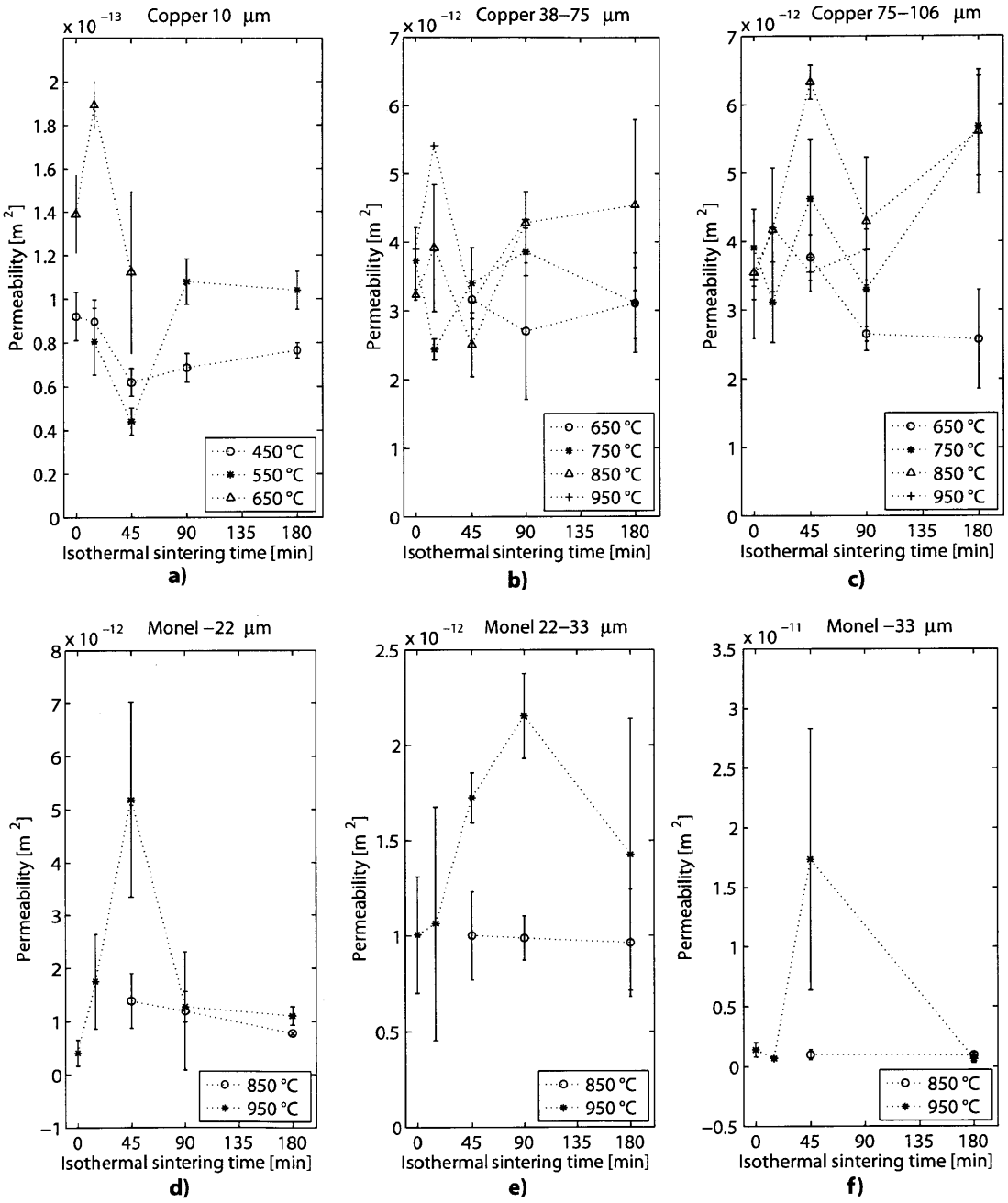

Figure 2.9: Results from permeability measurements as a function of isothermal sintering time for **a)** copper 10 μm; **b)** copper 38-75 μm; **c)** copper 75-106 μm; **d)** Monel -22 μm; **e)** Monel 22-33 μm; and, **f)** Monel -33 μm samples.

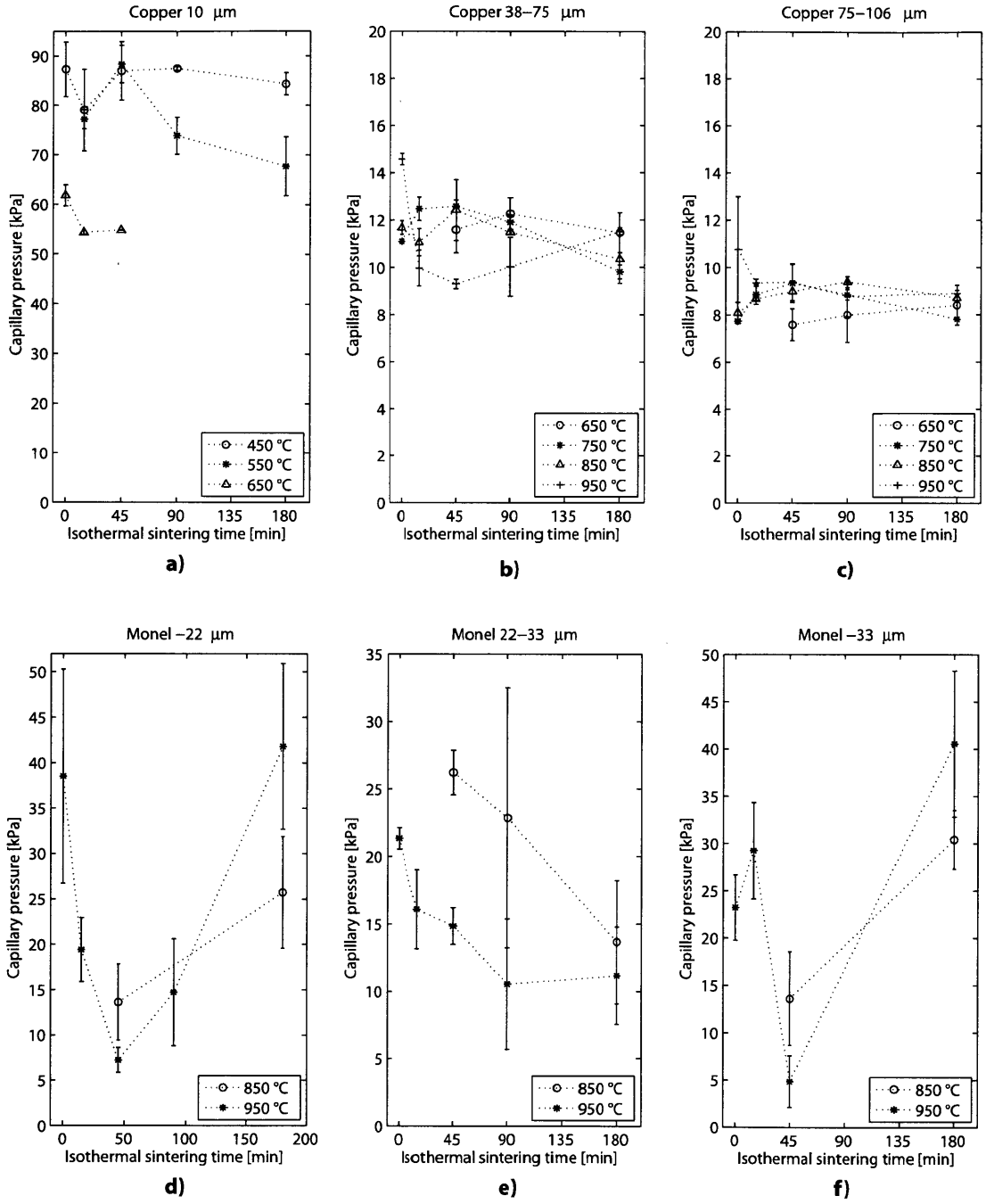

Figure 2.10: Maximum capillary pressure measured for **a)** copper 10 μm, **b)** copper 38-75 μm, **c)** copper 75-106 μm, **d)** Monel -22 μm, **e)** Monel 22-33 μm, and **f)** Monel -33 μm sintered wicks.

tube and the wick was observed under an optical microscope (Figure 2.6). Whenever a gap was visible in the wick, the capillary pressure the wick was able to sustain was substantially lower. However, the capillary pressure that these samples could sustain was larger than the capillary pressure calculated from the Young-Laplace equation (Equation 1.1) based on the wall-wick gap dimension. This behavior suggests that the gap seen was not a continuous one and that along the length of the wick, there was a smaller gap between the sinter and the tube wall. In these cases, some measured samples could sustain a high capillary pressure, while others could not. Thus, the variability of these measurements was large and can be seen as data points with larger error bars in Figure 2.10.

2.5 Multiple Sintering Procedures

Part of the manufacturing process of PHUMP involves multiple heating cycles. As described in Chapter 1, the first sintering step is the sintering of the evaporator liquid and vapor channels using a graphite mold. For the liquid channels, copper 38-75 μm powder and copper 75-106 μm powder was sintered at 850 °C for 15 minutes. For the vapor channels, 10 μm copper powder was sintered at 550 °C for 30 minutes. The coarse copper molded part was placed in the evaporator Monel frame. The Monel powder insulating layer (1 mm) was sintered on top of the coarse copper molded part. This step happened at 850 °C for 30 minutes. Then, a thin layer (0.5 mm) of 10 μm copper powder was spread over the sintered Monel and the fine copper molded part was placed on that powder layer. The thin layer of 10 μm copper powder was sintered for 30 minutes at 550 °C. Finally, a solid copper lid was attached to the evaporator using another layer of 10 μm copper powder between the copper lid and the fine copper molded part. This last step happened at 450 °C for 30 minutes.

Once the manufacture of the evaporator is complete, the coarse copper molded part will have been sintered at 850 °C for 15 minutes, then at 850 °C for 30 minutes,

at 550 °C for 30 minutes and, finally, at 450 °C for 30 minutes. The fine copper molded part will have been sintered at 550 °C for 30 minutes twice and, finally, at 450 °C for 30 minutes. To test for the effect of these multiple sintering steps on the properties of the sintered wicks, disk and tube samples were prepared and sintered according to these sintering conditions. Permeability, capillary pressure and thermal conductivity were measured after each sintering heating cycle.

There are some differences in the sintering procedure used for fabricating the samples of the present section compared to the procedure explained in the previous section. First, the samples were not shaken in a shaker table because it is not practical to shake the wide, thin PHUMP geometries. Second, the sintering heating ramp rate was not constant, because it was based on the maximum capability of the furnace used. A process diagram of furnace temperature and time is shown in Figure 2.11 for each metal powder and size. Figure 2.11**a** shows the process followed for the fine copper sintered at 450 °C for 30 minutes. The samples were first heated at 1833 °C/h from room temperature to 300 °C. Then the samples were heated at 643 °C/h up to 450 °C. The samples stayed at 450 °C for 30 minutes. Cooling (Figure 2.3) started after this period of time.

Figure 2.11**b** shows the process followed to sinter samples at 550 °C for 15 minutes. The samples were first heated at 1833 °C/h from room temperature to 300 °C. Then the samples were heated at 1000 °C/h up to 450 °C. The procedure continued heating the samples at 600 °C/h to 550 °C. The samples stayed at this temperature for 30 minutes. Cooling (Figure 2.3) started after this period of time.

Figure 2.11**c** shows the sintering process followed to sinter samples at 850 °C. The first steps up to a temperature of 450 °C is the same as that of Figure 2.11**b**. Then, the samples were heated from 450 °C to 600 °C at a heating rate of 1286 °C/h. The samples were then heated at 1200 °C/h to 700 °C. They were heated at 1000 °C/h to 800 °C and, finally, to 850 °C at 600 °C. The samples stayed at this temperature

Table 2.3: Description of the entire sintering cycle for each powder material and size

Wick material and size	Entire sintering cycle description
10 μm copper	550 °C for 30 minutes, 550 °C for 30 minutes & 450 °C for 30 minutes
38-75 μm copper	850 °C for 15 minutes, 850 °C for 30 minutes, 550 °C for 30 minutes & 450 °C for 30 minutes
75-106 μm copper	850 °C for 15 minutes, 850 °C for 30 minutes, 550 °C for 30 minutes & 450 °C for 30 minutes
-25 μm Monel	850 °C for 30 minutes, 550 °C for 30 minutes & 450 °C for 30 minutes
25-45 μm Monel	850 °C for 30 minutes, 550 °C for 30 minutes & 450 °C for 30 minutes
-45 μm Monel	850 °C for 30 minutes, 550 °C for 30 minutes & 450 °C for 30 minutes

for 15 or 30 minutes. Cooling (Figure 2.3) started after this period of time.

Figure 2.12 shows the evolution of permeability, capillary pressure and thermal conductivity of the 10 μm (Figure 2.12**a**, 2.12**b**, 2.12**c**), 38-75 μm (Figure 2.12**d**, 2.12**e**, 2.12**f**), and 75-106 μm (Figure 2.12**g**, 2.12**h**, 2.12**i**) copper wicks as they are sintered multiple times as part of the manufacturing of PHUMP. As it can be seen, flow properties varied along the multiple sintering processes involved in the fabrication of PHUMP. Table 2.3 describes the entire sintering process for each powder material and size. This process is referred as 'All sintering cycle' in Figure 2.12.

Average permeability increased slightly (approximately 5%) in the 10 μm copper samples from the first to the last step of the manufacturing. Average capillary pressure decreased 4% for these samples. This variation in permeability and capillary pressure suggests an increase in the average pore size of the wick. A similar behavior is seen in Figure 2.10**a** at a sintering temperature of 550 °C with sintering times above 45 minutes. A possible reason for this counterintuitive behavior is separation

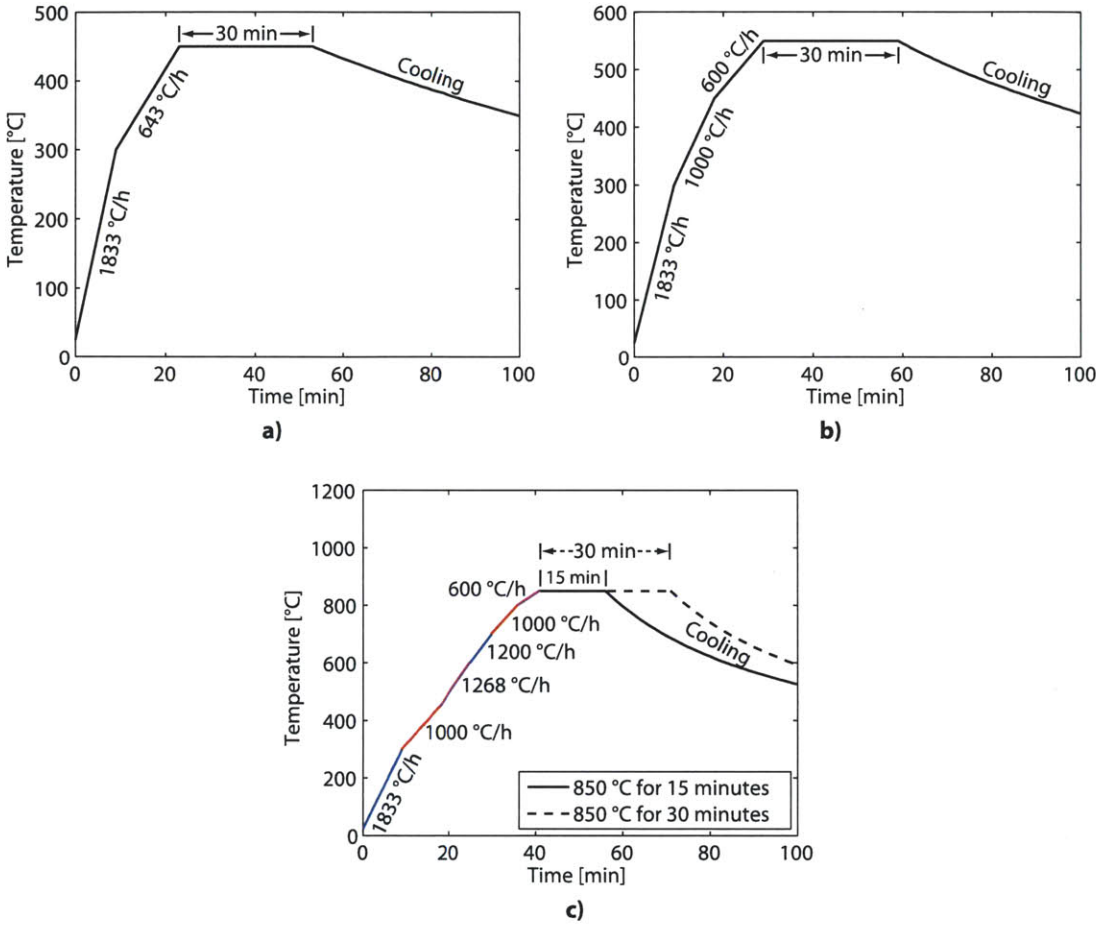

Figure 2.11: Temperature-time profile for different sintering processes. These profiles were used to test for the effect of multiple sintering processes on the properties of sintered wicks. Profiles for **a)** 10 μm copper samples sintered at 450 °C; **b)** 10 μm copper samples sintered at 550 °C; and, **c)** coarse copper and Monel powder samples sintered at 850 °C. The coarse copper samples were sintered for 15 minutes, while the Monel samples were sintered for 30 minutes.

of the wick from the wall of the tube, causing a low resistivity path to open parallel to the wick. 38-75 μm copper samples showed a considerable decrease in permeability, having an average change in this property of -19%. For these samples, capillary pressure stayed fairy constant within the uncertainty of the measurement, with an average change of around 2%. Strangely, the 75-106 μm powder samples showed the largest increase in permeability (29%). However, capillary pressure did not change significantly (3%) for this size range.

Average thermal conductivity varied appreciably for 10 μm copper samples. It changed from 59 W/m-K to 69 W/m-K after the second time it was sintered. By the time the entire sintering cycle was finished, thermal conductivity reached an average of 84 W/m-K. After the entire sintering process the average of this property increased by 42%. In contrast, thermal conductivity changed by 7% and 3% in the 38-75 μm and the 75-106 μm powder samples, respectively.

Figure 2.13 shows the evolution of permeability and capillary pressure of the non-spherical Monel wicks as they are sintered multiple times as part of the manufacturing of PHUMP. Permeability decreased considerably for every particle size from the first sintering process to the last one. The average decrease in permeability is 53%. The largest variation is observed in the particle range with the smallest particles (-25 μm), with an average decrease in permeability of 50%. The range that included the larges particles, -44 μm, had the lowest decrement in permeability with a -30% change. Capillary pressure increased for all the samples. The average increase in capillary pressure was approximately 30%. The average change in capillary pressure was 46% for the -25 μm particles; 25% for the 25-44 μm powder; and 18% for the largest particle range.

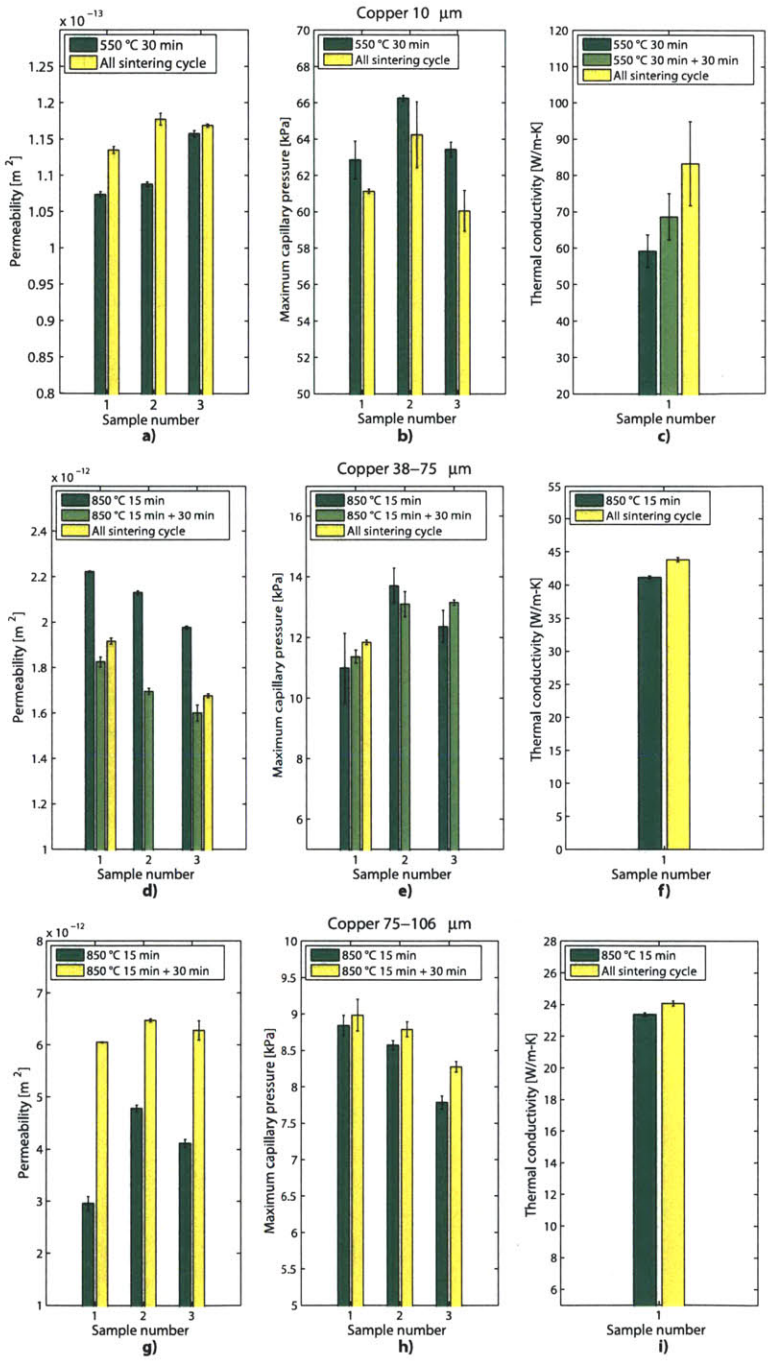

Figure 2.12: Effect of multiple sintering processes on the permeability, capillary pressure and thermal conductivity for **a)**, **b)**, **c)** 10 μm copper; **d)**, **e)**, **f)** 38-75 μm copper; and **g)**, **h)**, **i)** 75-106 μm copper samples.

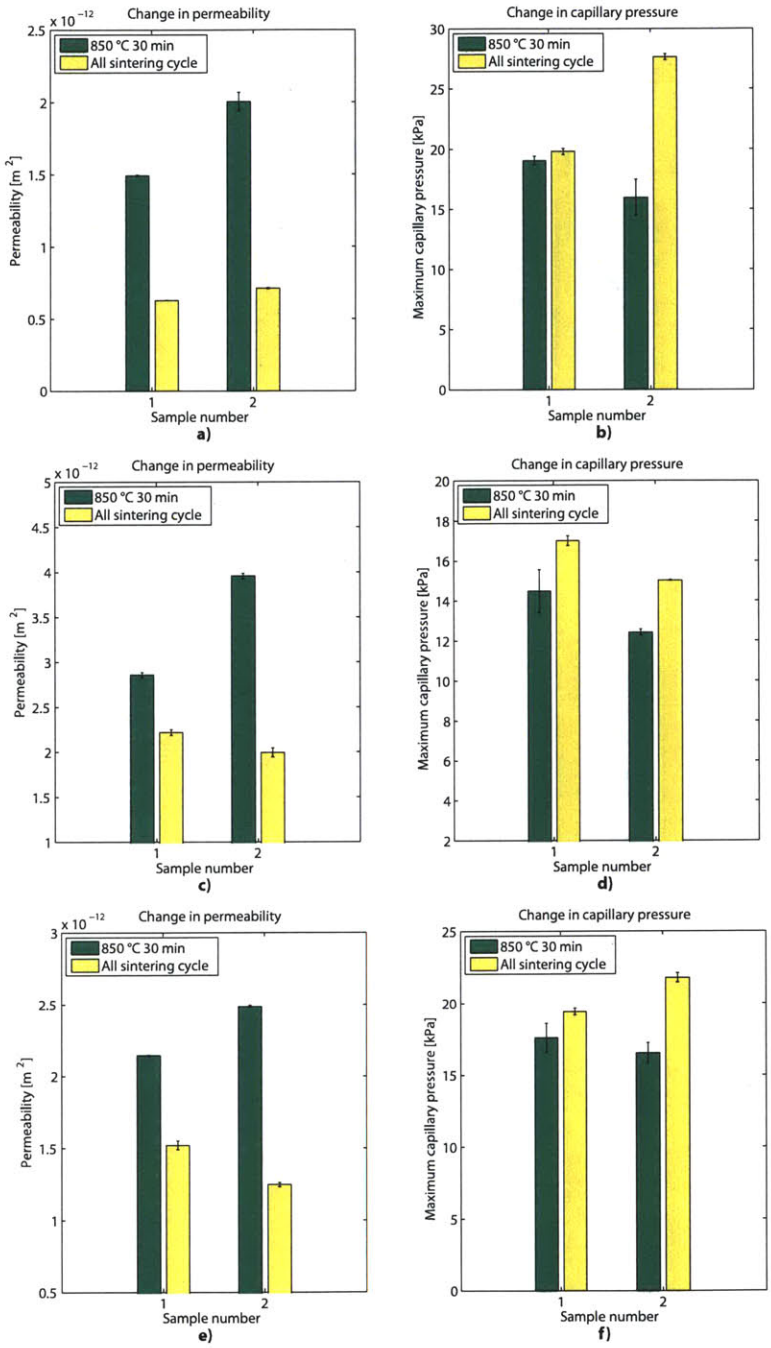

Figure 2.13: Effect of multiple sintering processes as explained in this section for Monel sinters: **a)** permeability of -25 μm; **b)** maximum capillary pressure of -25 μm; **c)** permeability of 25-44 μm; **d)** maximum capillary pressure of 25-44 μm; **e)** same as **c** but for -44 μm; and **f)** same as **d** but for -44 μm.

Table 2.4: General description of the samples tested for temperature cycling tests

Sample number	Description
1	Monel -44 μm. All the sintering cycle
2	Monel -44 μm. All the sintering cycle
3	Copper 38-75 μm. All the sintering cycle
4	Copper 75-106 μm. All the sintering cycle
5	Copper 10 μm. All the sintering cycle

2.6 Freezing-Thaw Test

As mentioned in Chapter 1, PHUMP has to be robust enough to sustain storage temperatures ranging from -54 °C to 100 °C. Although no damage is expected to occur in the sinter derived from these temperatures, a test was performed to assess the durability of the water saturated sinters when subjected to temperature cycling. Five of the multiple heating cycle samples were saturated with water and then frozen and thawed 50 times. The temperature of the water saturated sample was cycled from -30 °C to 30 °C. The sinter samples were placed in a cast aluminum box. The box was partially filled with distilled water and sealed using an O-ring between the lid and the rest of the box. The volume of water occupied 75% of the volume available inside the box at room temperature, so water was allowed to expand upon freezing. In the real system water will also be allowed to expand upon freezing, because not all of the volume in the heat pipe is occupied by water. After the temperature cycling, capillary pressure and permeability were measured and compared with the values measured before the cycling. Approximately eight months had passed between the first measurement (before the freezing test) and the measurement after the test. A general description of the samples tested can be found in Table 2.4. Reference to 'All the sintering cycle' means that the sample went through every manufacturing procedure as explained in the previous section. The results of the test are shown in Figure 2.14.

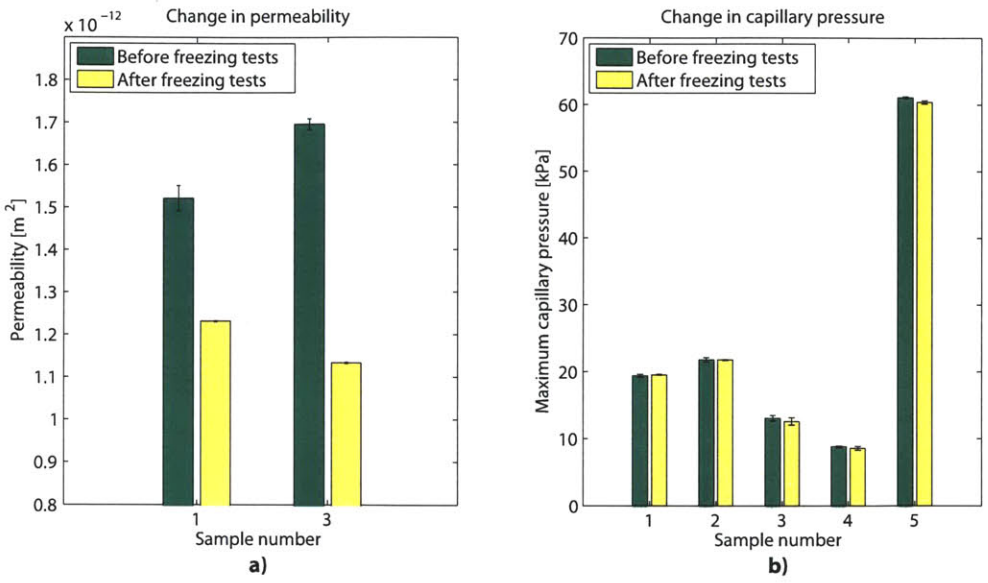

Figure 2.14: Effect of freeze-thaw cycling on **a)** the permeability; and **b)** the maximum capillary pressure of six samples. Note that only sample 1 and 3 were tested for permeability changes. Refer to Table 2.4 for more information regarding the samples tested.

Figure 2.14**a** shows the measured values of permeability before and after the freeze-thaw test. Permeability decreased for the samples tested, but still remained in an acceptable range for the proper operation of PHUMP. This change in permeability is not consistent with damage derived from freezing, in which case permeability would be expected to increase. However the decrease in permeability could be caused by contamination of the sinter. Said contamination could have happened during storage and handling between the first and second measurements. Figure 2.14**b** shows the measured capillary pressure before and after the freeze-thaw cycle. The capillary pressure did not change significantly. The maximum deviation was 4%, which is on par with the uncertainty of the measurement. Additionally, observation of the wick under an optical microscope revealed no evident damage.

2.7 Chapter Summary

Measurements of shrinkage, permeability, capillary pressure and thermal conductivity were conducted in copper and Monel sintered powder of different particle size ranges and for different sintering times and temperatures. Sinter samples shrank by up to 20%, causing in some of the samples, detachment of the wick from the walls of its container. If shrinkage of a sintered wick is excessive, then water can flow through the gap between the wick and the wall, in parallel to the sinter. This situation thwarted accurate measurement of the flow properties of the wick itself. For the range where shrinkage did not thwart accurate measurements, permeability and capillary pressure were found to be related to the particle size, but did not change systematically with sintering time and temperature. This behavior is related to the strong dependence of permeability and capillary pressure on the geometry of the wick. If detachment of the wick from the wall is to be avoided, then a low value of shrinkage is preferred. As a consequence, the average wick pore will undergo a relatively small change in size and capillary pressure and permeability will show no appreciable variation.

As expected, thermal conductivity of a sintered wick depended on the thermal conductivity of the material being sintered. For the same sintering time and temperature, larger particles had lower thermal conductivity. In contrast with permeability and capillary pressure, thermal conductivity showed a clearer increasing trend with increasing sintering time and temperature. Broad particle size range samples showed greater variability in this measurement, suggesting that randomness associated with their size plays an important role in defining their thermal conductivity.

It was found that multiple sintering procedures noticeably change the permeability and capillary pressure of the coarse copper powder (38-75 and 75-106 μm). Nevertheless, the value of these properties after multiple sintering procedures still fall in the range of values shown in Figure 2.9 and 2.10. It was found that the change in permeability and capillary pressure of the 10 μm copper samples is relatively small. In the

case of capillary pressure, this change is close to the uncertainty of the measurement.

The model described in Chapter 4 is based on the sintering procedure described in the present chapter and will explain the reasons behind the behavior of the measured sintered wick's thermal conductivity. As an introduction to this model, the next chapter presents a general discussion on the topic of sintering.

Chapter 3

Principles of the Two-Sphere Sintering Model

Sintering is a manufacturing process that consolidates a mass of particles together. The particles are heated to a temperature below the melting point of the material or alloy being sintered, but high enough to bond the particles together by means of diffusional processes. Properties of the consolidated piece depend on multiple fabrication parameters including particle material and shape, sintering time, temperature and atmosphere. In this chapter, the theoretical foundation of sintering applied to the 'two-particle model' is described. This model provides an understanding of the link between the fabrication conditions and the final properties of the sinter.

3.1 Sintering Mechanisms

Sintering is driven by the reduction of surface energy. Atoms diffuse from surfaces of high curvature to neighboring areas where the curvature is lower. This movement of atoms is expressed in the well-known relation between the diffusion potential in the surface for species i, Φ_i^S, and the local curvature, κ. The lattice-constrained diffusion potential, assuming that vacancies are in equilibrium, is [6]

$$\Phi_i^S = \mu_i^\circ + \gamma\kappa\Omega_i \tag{3.1}$$

where μ_i° is the chemical potential at the reference state (free energy per atom in a flat surface); γ is the surface tension of the interface; and, Ω_i is the atomic volume of component i. Because κ is positive in a convex region and negative in a concave surface, the diffusion potential of a convex region is larger than the one associated with a concave surface [6].

The empirical force-flux law for the diffusion of component i is the modified Fick's law

$$\vec{J}_i = -M_i c_i \nabla \Phi_i \tag{3.2}$$

where $\vec{J}_i$ is the diffusion flux of component i; M_i is the mobility (the velocity of component i induced by a unit force); and, c_i is the concentration of component i. Combining Fick's law with Equation 3.1, the diffusional flux of component i is

$$\vec{J}_i = -M_i c_i \gamma \Omega_i \nabla \kappa \,. \tag{3.3}$$

Thus, a flow of atoms will spontaneously arise from the convex zone to the concave one. The local diffusion potential (Equation 3.1) produces a flux of atoms (Equation 3.3) along the surface, through the bulk (since the atoms in the bulk are imbedded in a zero curvature region) and also via evaporation/condensation. The latter originates from the difference in vapor pressure in equilibrium with a curved surface ($\kappa \neq 0$) and in equilibrium with a flat surface ($\kappa = 0$). The resulting flux of atoms will move from the convex region to the concave zone by means of evaporation-condensation [6]. When two particles are in contact during sintering, as shown in Figure 3.1, regions with different curvatures are inevitably present. In Figure 3.1, it is easily seen that atoms will flow to the interface between the particles, causing the connection between them (the 'neck') to grow.

Certain transport mechanisms will move matter from the bulk of the crystal to the neck, causing the centers of the sphere to approach each other. These processes cause shrinkage and are referred as 'densifying mechanisms'. All of the mechanisms

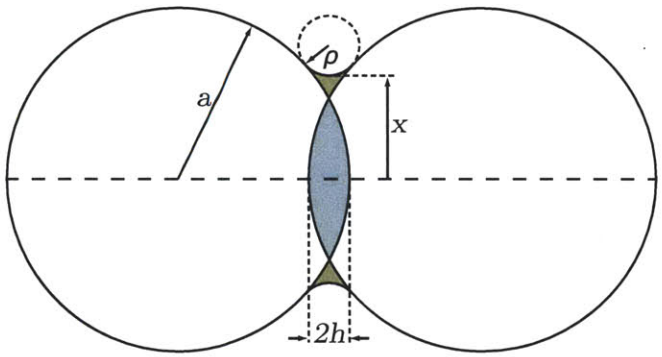

Figure 3.1: Geometry in the two-sphere model. a is the radius of the spheres, x is the radius of the neck. The neck is assumed to be an arc of a circle of radius ρ delimited by the points where it touches both spheres. Thereby, the radius of curvature of the neck is ρ. h is a measurement of the overlap between the spheres to account for densification during sintering.

relevant to the sintering of refractory metals are described in Table 3.1 [6].

3.2 The Two-Sphere Model

Sintered wicks are complex three-dimensional (3D) structures. During the course of sintering new connections between particles will form. As these connections grow, the size of the pores in the wick decreases. Nevertheless, rupture of existing connections can also occur and as a consequence some of the pores will increase in size [18]. The exact geometry of the neck between two particles actually depends on all of the connections that these particles have. As an example, it has been experimentally shown that the evolution of three bonded particles depends on the initial angle that the centers of the spheres form [18]. This angle can increase, decrease or stay approximately constant during the sintering process. Then, in order to precisely define the geometry of the wick a 3D model that follows each of the connections in the whole structure has to be constructed. It is clear that such a model would be prohibitively expensive in computational terms. To overcome the difficulties involved in a full simulation of the sinter structure, simpler geometries are considered here. These models are used

Table 3.1: Sintering mechanisms in refractory metals

Densifying mechanisms	
Mechanism	Description
Boundary-surface crystal diffusion	Diffusion through the lattice from the grain boundary to the surface
Boundary-surface boundary diffusion	Diffusion along the grain boundary to the surface
Non-densifying mechanisms	
Mechanism	Description
Surface-surface crystal diffusion	Diffusion through the lattice from positive curvature surface regions to lower curvature regions
Surface-surface surface diffusion	Surface diffusion from positive curvature surface regions to lower curvature regions
Evaporation-condensation	Evaporation from larger-curvature regions and condensation at lower-curvature regions

as the basis for inferring the expected behavior of the overall structure.

3.2.1 Geometric Description of the Two-Sphere Model

The parameters that fully define the two-sphere model (referring to Figure 3.1) are the radius of the particles, a; the radius of the neck, x; and the distance between the center of the particles, $2(a-h)$. The most common geometric simplification for this model is to consider the neck as the arc of a circle. Then, the radius of curvature of the neck, ρ, can be obtained by simple geometry in terms of the aforementioned parameters as

$$\rho = \frac{(x-h)^2}{2(a-x)}. \tag{3.4}$$

Conservation of mass relates x and h because all of the volume encompassed in the region where the spheres overlap has to be the same as the volume of the neck (gray and brown regions in Figure 3.1). However, an analytical expression of h as

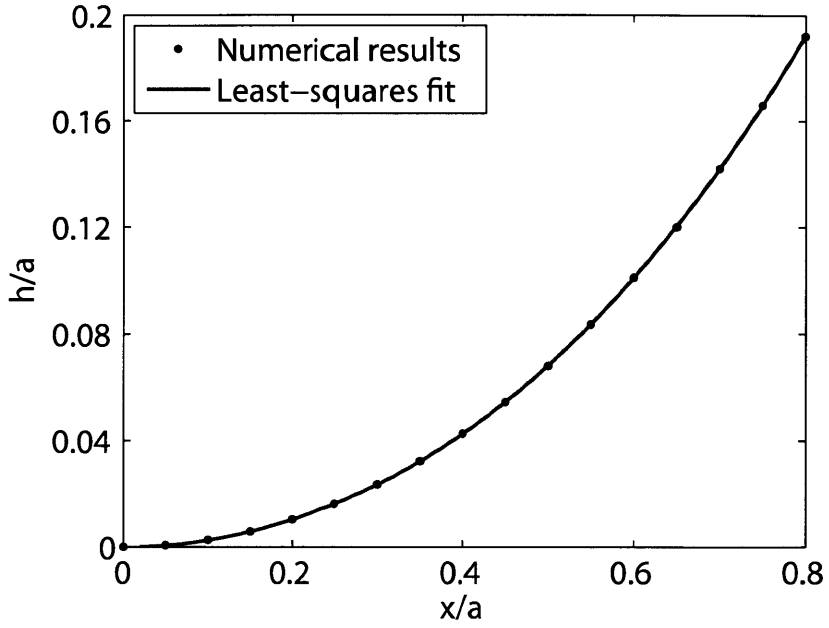

Figure 3.2: Numerical results of h/a as a function of x/a, and least square polynomial fit for the numerical results.

a function of x or vice versa does not exist. Exner [18] used a numerical procedure to obtain h/a for some values of x/a. Those values are plotted in Figure 3.2. A least-squares fit for the numerical results is also shown in Figure 3.2. This fit is a sixth degree polynomial and is used in this thesis to obtain the value of h for any value of x considered.

3.2.2 Neck Growth in the Two-Particle Model

The radius of the neck as a function of temperature and time, $x(T,t)$, can be obtained by first defining the diffusion potential (Equation 3.1) for the geometry of Figure 3.1. Then, Equation 3.3 is used to define a flux of atoms to the neck area. Each mechanism will have its own value of mobility, since the mobility is related to the diffusion coefficient of each mechanism. Finally, the diffusional flux is related to the geometry of the neck. This relation is obtained by considering the amount of matter that is being moved and the change in volume that it will produce in the neck. The functional form of $x(T,t)$ is the same for all the mechanisms because the

Table 3.2: Values for m, n and $C(T)$ in equation 3.5

Sintering mechanism	m	n	$C(T)$
Boundary-surface crystal diffusion	3	5	$\frac{16D_{VD}\gamma M}{RT}$
Boundary-surface boundary diffusion	4	6	$\frac{48D_{GBD}\gamma bM}{RT}$
Surface-surface crystal diffusion	3	4	$\frac{20D_{VD}\gamma M}{RT}$
Surface-surface surface diffusion	4	7	$\frac{23D_{SD}\gamma M\Omega^{1/3}}{RT}$

mass transport is governed by diffusional processes. This functional form is given by

$$x^n = \frac{C(T)}{a^{m-n}}t \tag{3.5}$$

where the value of the exponents m and n and the factor $C(T)$ for the most important transport mechanisms can be found in Table 3.2 [18].

In Table 3.2, D_{VD} is the volume diffusion coefficient; γ is the material surface energy; M is the molar volume; D_{GBD} is the grain boundary diffusion coefficient; b is the grain boundary width; Ω is the atomic volume; R is the gas constant; and, T is the sintering temperature. It can be seen from this table that the factor $C(T)$ depends on the diffusion coefficient of each mechanism. $C(T)$ is determined from the solution of Equation 3.3 and the particular conditions in the flow of atoms for each mechanism. For example, for surface diffusion, the mobility, M_i, is related to the surface self-diffusion coefficient, D_{SD}, by the Nernst-Einstein equation [6]

$$D_{SD} = M_i kT \tag{3.6}$$

where k is the Boltzmann constant and T is the temperature. The concentration of species i in the first atomic layer is one atom per atomic volume, hence $c_i = 1/\Omega_i$ [6]. The Boltzmann constant is related to the gas constant by Avogadro's number, N_A,

such that $k = R/N_A$. Thus, Equation 3.3 becomes

$$\vec{J}_i = -\frac{D_{SD} N_A \gamma}{RT} \nabla \kappa \,. \tag{3.7}$$

Equation 3.7 gives a flux of atoms per unit area per unit time. Each atom that flows to the neck between two sintering particles will increase the volume of the neck by the volume of an atom. Rockland has shown that the relation between the neck size, x, and the flux of species i, $\vec{J}_i$, is given by [47]

$$\frac{\mathrm{d}x}{\mathrm{d}t} \propto \frac{\Omega_i^{4/3} \vec{J}_i}{\rho^3 \nabla \kappa} \tag{3.8}$$

where ρ is the curvature of the neck. Thus, substitution of Equation 3.7 in Equation 3.8 gives

$$\frac{\mathrm{d}x}{\mathrm{d}t} \propto \frac{D_{SD} \gamma M \Omega^{1/3}}{\rho^3 RT} \tag{3.9}$$

where $M(= N_A \Omega)$ is the molar volume of the diffusing element. The general form of $C(T)$ for surface diffusion $\left(C(T) \propto \frac{D_{SD} \gamma M \Omega^{1/3}}{RT}\right)$ can be found in Equation 3.9.

An analytical solution for the neck size as a function of sintering temperature and time, $x(T, t)$, that includes all of the mechanisms has not been found, because the mechanisms are coupled. The coupling results from the fact that all the mechanisms affect the geometry, which drives all of the mechanisms. One possible solution to overcome this difficulty is to numerically solve the equation in small steps of x/a [18]. A different approach consists of considering the solution of the dominant mechanisms. A first step in determining the relative importance of the mechanisms in Table 3.2 to the overall sintering rate is to analyze the paths that the diffusing material travels towards the neck region. Diffusion along the surface and along the grain boundary can be seen as 'short-circuit diffusion paths' with diffusion rates orders of magnitude larger than those associated with diffusion across the bulk of the particle [6]. Vacancies facilitate diffusion because the activation energy associated with an atom jumping into a vacant site is smaller than the energy associated with jumping

into an interstitial or occupied site. Both the free surface and the grain boundary are efficient sources and sinks of vacancies. It is for this reason that, traditionally, sintering models consider surface diffusion and grain boundary diffusion as the only mechanisms involved in the sintering process.

3.2.3 Surface Diffusion and Grain Boundary Diffusion as Dominant Mechanisms

Given the complexity of describing the neck shape with precision, especially when considering coupled transport, it is customary to take into consideration only the dominant sintering mechanisms. In general, diffusion in copper sintering is dominated by grain boundary diffusion at low temperatures and by surface diffusion at higher temperatures. The exact value of the temperature at which the dominant mechanism transitions from grain boundary diffusion to surface diffusion depends on the particle size and the sintering time. It is common in sintering literature to refer to a dimensionless parameter, Γ, which compares the effective diffusion rate of grain boundary diffusion to the rate of surface diffusion

$$\Gamma = \frac{\delta_{GBD} D_{GBD}}{\delta_{SD} D_{SD}} \tag{3.10}$$

where δ_{GBD} and δ_{SD} are characteristic cross-sectional diffusion lengths for grain boundary and surface diffusion, respectively; and D_{GBD} and D_{SD} are their respective diffusion coefficients. Although more precise measurements of δ_{GBD} and δ_{SD} exist (e.g. [22]), it is customary to assume that δ_{GBD} is equal to two interatomic distances [56] and δ_{SD} is equal to one interatomic distance [6]. Given the fact that D_{GBD} and D_{SD} depend on temperature, Γ also depends on temperature. Figure 3.3 shows this dependence for copper.

At low temperatures, grain boundary diffusivity dominates. Grain boundary diffusion is a densifying mechanism, and thus, high shrinkage rates can be expected at

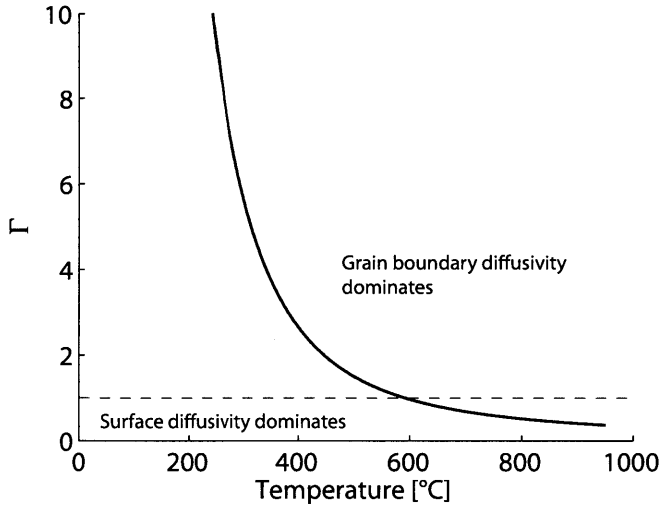

Figure 3.3: Γ as a function of temperature for copper. The dashed line marks $\Gamma = 1$. Grain boundary diffusion rate dominates at lower temperatures. It is expected that at lower temperatures densification is more important than at higher temperatures.

lower temperatures. At higher temperatures, surface diffusion dominates. This mechanism moves matter from one part of the surface to the lower curvature zone without changing the distance between the centers of the particles. Therefore, shrinkage rates are expected to be lower at higher temperatures.

Consider first the case when $\Gamma \ll 1$. Surface diffusion is the only active mechanism, so no shrinkage occurs during sintering. From Table 3.2 and Equation 3.5, the governing differential equation for the neck growth is

$$\frac{\mathrm{d}x}{\mathrm{d}t} = \frac{23 D_{SD} \gamma M \Omega^{1/3} a^3}{7 x^6 R T} \tag{3.11}$$

where x is the neck radius; D_{SD} is the surface self-diffusion of the material being sintered; γ is the material surface energy; M is the molar volume; Ω is the atomic volume; a is the radius of the particle; R is the gas constant; T is the sintering temperature; and, t is the sintering time. Integration of equation 3.11 with respect

to time, when the temperature is itself a function of time yields

$$x^7 - x_0^7 = \frac{23 D_{SD_0} \gamma \Omega^{1/3} M a^3}{R} \int_0^t \frac{\exp\{-\frac{Q_{SD}}{RT}\}}{T} \, \mathrm{d}t \tag{3.12}$$

where x_0 is the neck size at time $t = 0$; D_{SD_0} is the pre-exponential factor of the Arrhenius-type equation for the surface diffusivity; and, Q_{SD} is the activation energy of surface diffusion. Equation 3.12 will be used to account for the change in the neck size during the heating and cooling of the samples.

The case for $\Gamma \gg 1$ is not analogous to the previous case when $\Gamma \ll 1$. These cases are not equivalent because Γ only compares the diffusion rates, not the sintering rates between particles. As grain boundary diffusion moves atoms along the grain boundary to the surface, the curvature in the middle of the neck will rapidly go to zero, removing the driving force for further diffusion. Matter in the middle of the neck has to be redistributed by surface diffusion to nearby areas of lower curvature. Thus, even when the grain boundary diffusivity rate is larger than the surface diffusion rate, the growth of the neck is limited by surface diffusion. In the opposite case, when $\Gamma \ll 1$ surface diffusion is capable of redistributing all of the material coming to the neck from more distant parts of the surface. When grain boundary diffusion is the dominant mechanism and surface diffusion is capable of redistributing all the material transported by grain boundary diffusion then, from Table 3.2 and Equation 3.5, the sintering rate is

$$\frac{\mathrm{d}x}{\mathrm{d}t} = \frac{8 D_{GBD} \gamma b M a^2}{x^5 RT} \tag{3.13}$$

where x is the neck radius; D_{GBD} is the grain boundary self-diffusion of the material being sintered; γ is the material surface energy; M is the molar volume; b is the grain boundary width ($b = \delta_{GBD}$); a is the radius of the particle; R is the gas constant; T is the sintering temperature; and, t is the sintering time. The integration of equation 3.13, when the temperature is a function of time yields

$$x^6 - x_0^6 = \frac{48 D_{GBD_0} \gamma b M a^2}{R} \int_0^t \frac{\exp\{-\frac{Q_{GBD}}{RT}\}}{T} \, \mathrm{d}t \tag{3.14}$$

where D_{GBD_0} is the pre-exponential factor of the Arrhenius-type equation for the diffusivity; and, Q_{GBD} is the grain boundary diffusion activation energy. Equations 3.12 and 3.14 do not have closed-form solutions for arbitrary temperature profiles but can be integrated numerically.

When $\Gamma \approx 1$ neither sintering mechanisms can be disregarded and the coupling between them must be modeled. Once material has diffused to the neck, the curvature of this region becomes larger than the surrounding area. Then, surface diffusion stops moving material to the center of the neck and instead, it redistributes material to the surrounding areas. It is possible to find many sintering models in the literature that take into account this coupling (e.g. [9, 56, 61]). When working with the case $\Gamma \approx 1$ in this thesis, the results of the model of Zhang et al. [61] were used. This model matches the flux of material from the grain boundary to the surface diffusion flux at the intersection of the grain boundary with the free surface [61]. It is important to mention that results from the model of Zhang et al. are available for specific values of Γ. The available results are for $\Gamma = 0$, $\Gamma = 0.1$, $\Gamma = 1$ and $\Gamma = 10$. Different values of Γ were rounded to the closest value of Γ for which solutions are available.

3.3 Two-Sphere Model Results

3.3.1 Sintering of Fine Copper Powder

The governing differential equations for grain boundary diffusion, surface diffusion and the results from Zhang et al. [61] were used to determine the neck size between particles for the experimental sintering processes described in Chapter 2. Results from the model for the neck size will be given after the heating process (point marked with an 'a' in Figure 3.4), after the isothermal sintering at the peak temperature (point marked 'b' in Figure 3.4) and after the cooling down (point marked 'c' in Figure 3.4).

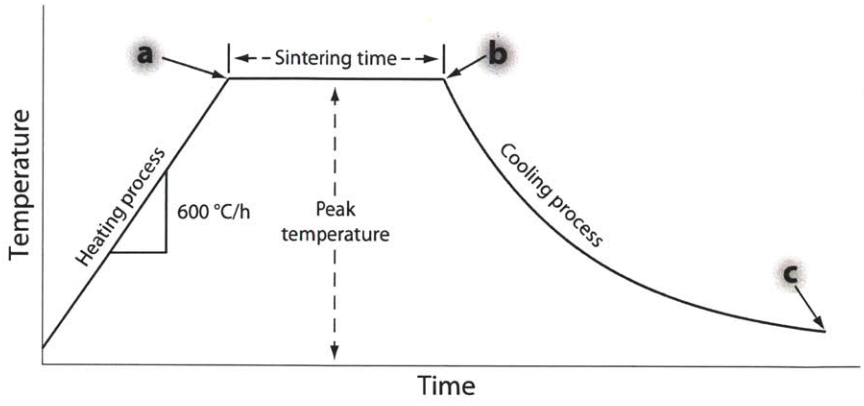

Figure 3.4: Time-temperature plot of the sintering process. Results from the model of this chapter are given for the points marked in the plot. Point 'a' marks the end of the heating process, point 'b' marks the end of the isothermal sintering at the peak temperature and point 'c' marks the end of the cooling process.

First, the neck size was calculated at the end of the heating process ('a' in Figure 3.4). The heating ramp rate, 600 °C/h, was used to define a relation of $T = T(t)$ in Equation 3.12 and 3.14. The initial conditions were $T(t = 0) = 25$ °C and $x(t = 0) = 0$. For the heating process, temperature was increased in steps of 0.01 °C. At every step Γ was calculated and used to determine the dominant mechanism. The differential equation for the appropriate mechanism was integrated, and the neck size resulting from this integration was used as the initial condition for the next step. Table 3.3 shows the values of the constants in Equation 3.12 and 3.14. Figure 3.5 shows the neck size and shrinkage parameter for the 10 μm copper samples at the end of the heating process as a function of the final temperature of the process. The cusps in the plot of x/a are numerical artifacts related to the transitions between mechanisms.

As seen in Figure 3.3, surface diffusion dominates at high temperatures. Sintering by surface diffusion is attractive because of the low associated shrinkage rates. A faster ramp rate was tested as a manner of reaching high temperatures while spending a small period of time in the grain boundary diffusion dominated area. A ramp rate of 2000 °C/h was simulated and is also shown in Figure 3.5. This ramp rate was the highest heating rate that the furnace used in this study could attain according

Table 3.3: Material data

Property	Copper	Nickel	Ref.
Atomic volume (Ω) [m^3]	1.18×10^{-29}	1.09×10^{-29}	[56]
Interatomic distance (δ) [m]	2.56×10^{-10}	2.49×10^{-10}	[56]
Surface energy (γ) [J/m^2]	1.72	2.00	[56]
Molar volume (M) [m^3/mol]	7.31×10^{-6}	6.59×10^{-6}	[38]
Pre-exponential factor for surface self-diffusion (D_{SD_0}) [m^2/s]	3.57×10^{-4}	-	[10]
Surface self-diffusion activation energy (Q_{SD}) [kJ/mol]	128.42	-	[10]
Pre-exponential factor for grain boundary self-diffusion (D_{GBD_0}) [m^2/s]	1.55×10^{-6}	-	[55]
Grain boundary self-diffusion activation energy (Q_{GBD}) [kJ/mol]	78.61	-	[55]
Pre-exponential factor for grain boundary diffusion in Monel (D_{GBD_0}) [m^2/s]	1.13×10^{-4}	2.8×10^{-5}	[42, 43]
Activation energy for grain boundary diffusion in Monel (Q_{GBD}) [kJ/mol]	165.80	156.70	[42, 43]

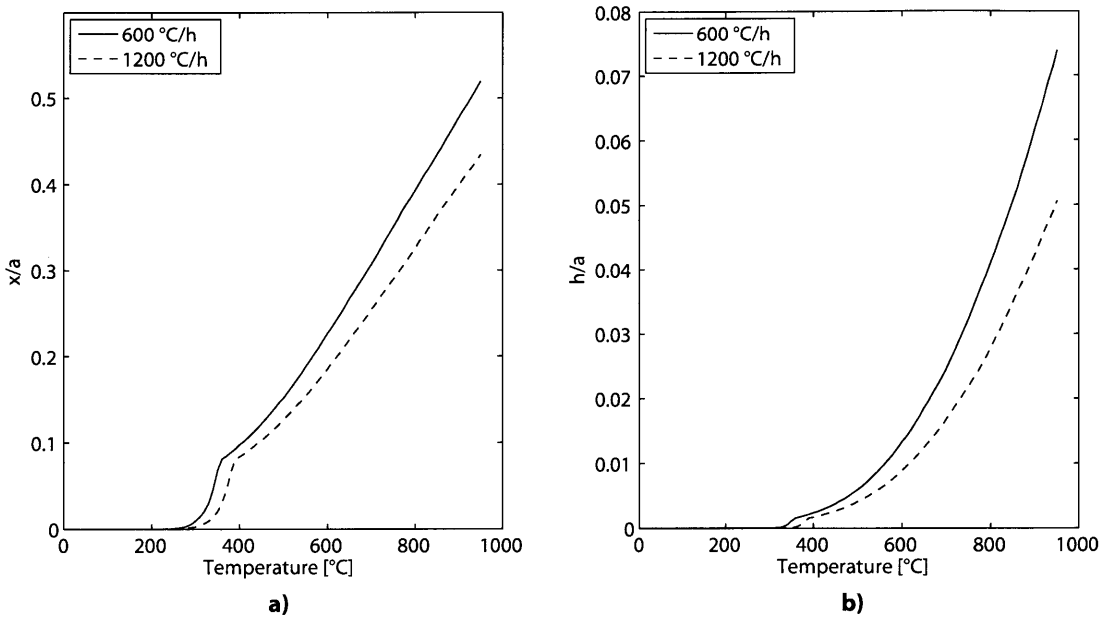

Figure 3.5: **a)** Relative neck size, x/a; and, **b)** densification, h/a, due to the heating process for a ramp rate of 600 °C/h and 2000 °C/h. The cusps in the plot are numerical artifacts related to the transition between mechanisms.

to the thermocouple that controls it. However, the local heating rate of the samples is expected to be slower due to the thermal capacity of the samples, especially when sintering more massive samples, such as actual PHUMP components. Figure 3.5 shows that smaller shrinkage results from less time spent at each temperature during heating up. However, it is important to consider the result of the full sintering process before evaluating the actual benefit of a faster ramp.

Once the heating process was over, the samples stayed at a constant temperature for different amounts of time, from zero to three hours ('b' in Figure 3.4). For the 10 μm copper samples, Figure 3.6 shows the evolution of the neck during sintering for different isothermal hold temperatures (from 450 °C to 950 °C). The initial neck size at each temperature comes from Figure 3.5. It can be seen in Figure 3.6 that as the isothermal sintering time increases, the neck size increases, but the rate of this growth also decreases. Shrinkage follows the same trend.

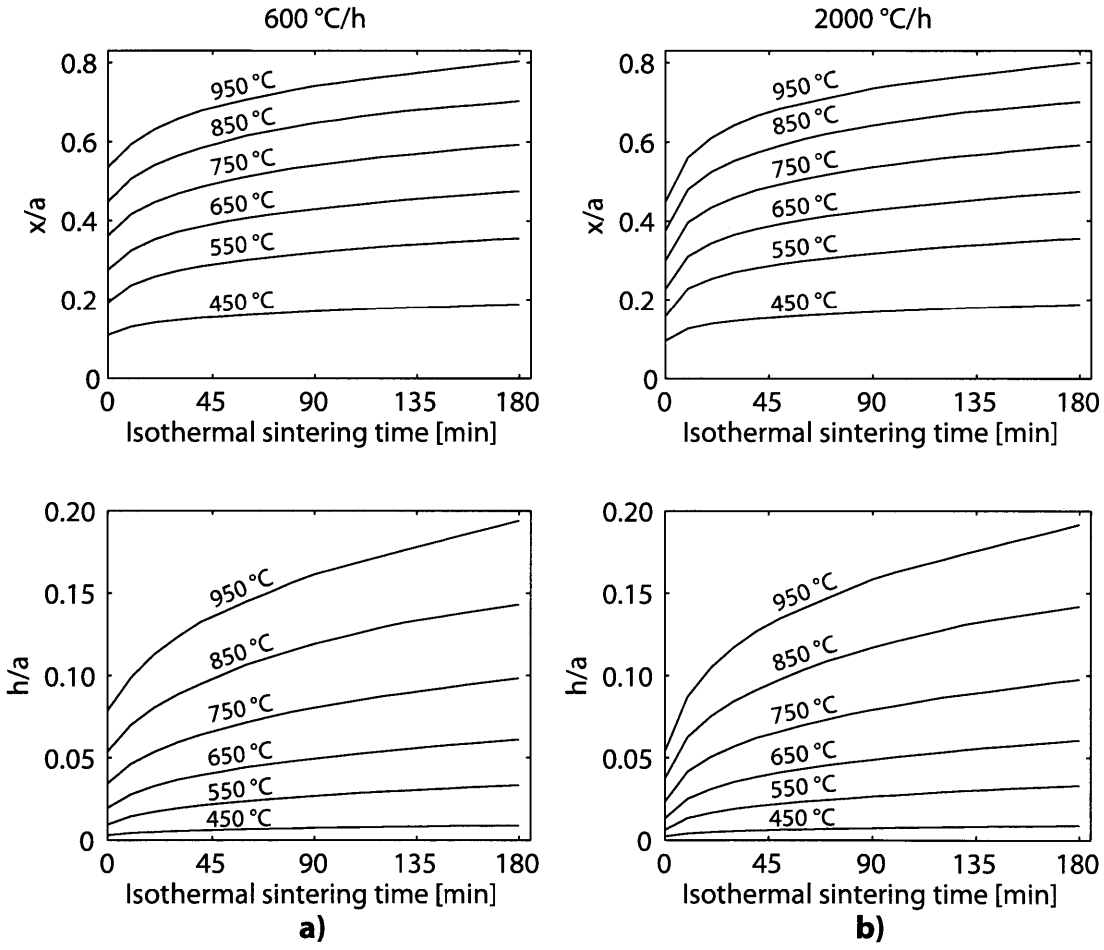

Figure 3.6: Isothermal sintering process for 10 μm copper. Neck size and densification evolution during sintering as a function of time and temperature for a heating ramp rate of **a)** 600 °C/h; and, **b)** 2000 °C/h.

Figure 3.6 shows that the benefit of a faster ramp rate is rapidly lost. After approximately 15 minutes of isothermal sintering, the neck size for both ramp rates is practically the same. Although the neck size is smaller at the start of the isothermal hold time for a higher ramp rate, the smaller neck has a larger curvature and therefore driving force to increase its size. The neck growth in the first minutes of isothermal sintering will be faster for the sample with the higher ramp rate. This behavior can be seen in the first 10 minutes of isothermal sintering in Figure 3.6 as a clearly steeper slope for the 2000 °C/h ramp.

The last step is cooling of the samples as the furnace cools ('c' in Figure 3.4). The final neck size during cooling depends on the neck size at the end of the isothermal sintering, and thus depends on the isothermal sintering time. Figure 3.7, shows the final neck size as a function of the isothermal hold temperature and the neck size at the start of cooling. The temperature profile used follows the furnace cooling profile shown in Figure 2.3.

Figure 3.7 shows the final neck size as a function of isothermal hold temperature, for different neck sizes at the beginning of the cooling process (x_0/a). As expected, the cooling process increases the neck size most significantly for cooling from higher isothermal temperatures and smaller neck sizes. For example, for $x_0/a = 0.5$, the neck size only increases during cooling from 600 °C or higher. Given the fact that during isothermal sintering the neck has been growing for a certain period of time, a negligible change in the neck size is expected during cooling down. This explains the small effect of heating and cooling ramps in multiple-sintered samples, as the actual change in the neck size depends more on the sintering time than on the number of ramps. However, for the shortest sintering times, ramping up and cooling are expected to have a larger effect on the final neck size, because the ramps and the sintering durations are comparable. This situation can be seen in Figure 3.8. This figure shows the final neck size considering the complete sintering process (ramp up, isothermal sintering and cooling) for the group of temperatures considered in this

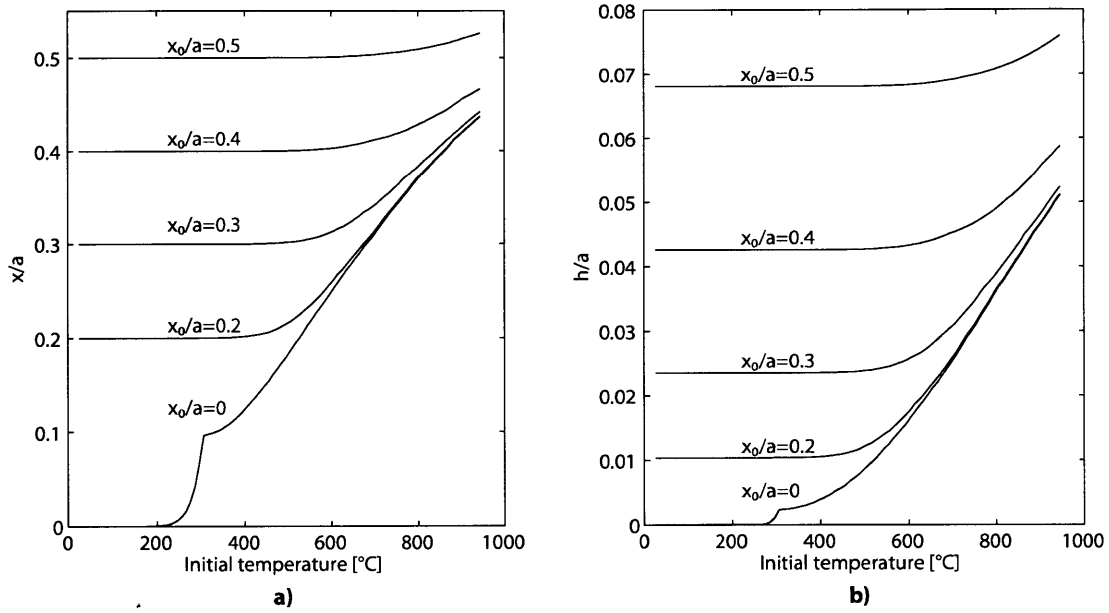

Figure 3.7: **a)** Neck size; and, **b)** densification parameter for fine copper samples during the cooling process. A family of curves for different initial neck size (x_0/a) is shown. The temperature profile used follows the furnace cooling profile shown in Figure 2.3. The cusps in the plot for $x_0/a = 0$ is an artifact related to the transition between mechanisms.

study. Comparison of Figure 3.6 and 3.8 reveals the effect of cooling at the shortest periods of isothermal sintering. The initial slope of the curves in Figure 3.6 is larger than in Figure 3.8, because there is neck growth during cooling. This neck growth is significant at the shortest isothermal sintering times since the time spent at the peak temperature is comparable to the time spent at relatively high temperatures during cooling. However, as the sintering time increases, the effect of cooling decreases. It is for this reason that the difference in slopes in the curves between Figure 3.6 and Figure 3.8 is notable only for the shortest sintering times.

3.3.2 Relationship between the Sintering Model and the Experimental Porosity and Shrinkage

Porosity and shrinkage are properties that depend on the structure of the wick. Clearly the structure of the actual wick is more complex and random than the simple cubic structure that is used in the model described in this chapter. However, it is possible to find a relationship between the sintering model and the experimental measurements for shrinkage and porosity. A fit between the model geometric parameters and the experimentally measured geometry of the wick accounts for the randomness associated with the packing of the spheres in the sample and its impact on the kinetics of sintering. Figure 3.9 shows the relation between the experimental linear shrinkage, ϵ_{exp}, and the shrinkage of the two-sphere model (TSM) of Figure 3.1, ϵ_{TSM}, for the 10 μm copper powder samples. As explained in Chapter 2, the linear shrinkage was measured using a caliper with a precision of ± 0.05 mm and calculated according to Equation 2.1. The shrinkage reported in Figure 3.9 is for the disk samples, where there is no bonding between the mold and the metal powder.

At low levels of shrinkage ($\epsilon_{\text{TSM}} < 10\%$) the relationship is fairly linear, but as the sintering temperature increases, the experimental value grows more slowly than the predicted values and thus the slope decreases as seen in Figure 3.9. One possible rea-

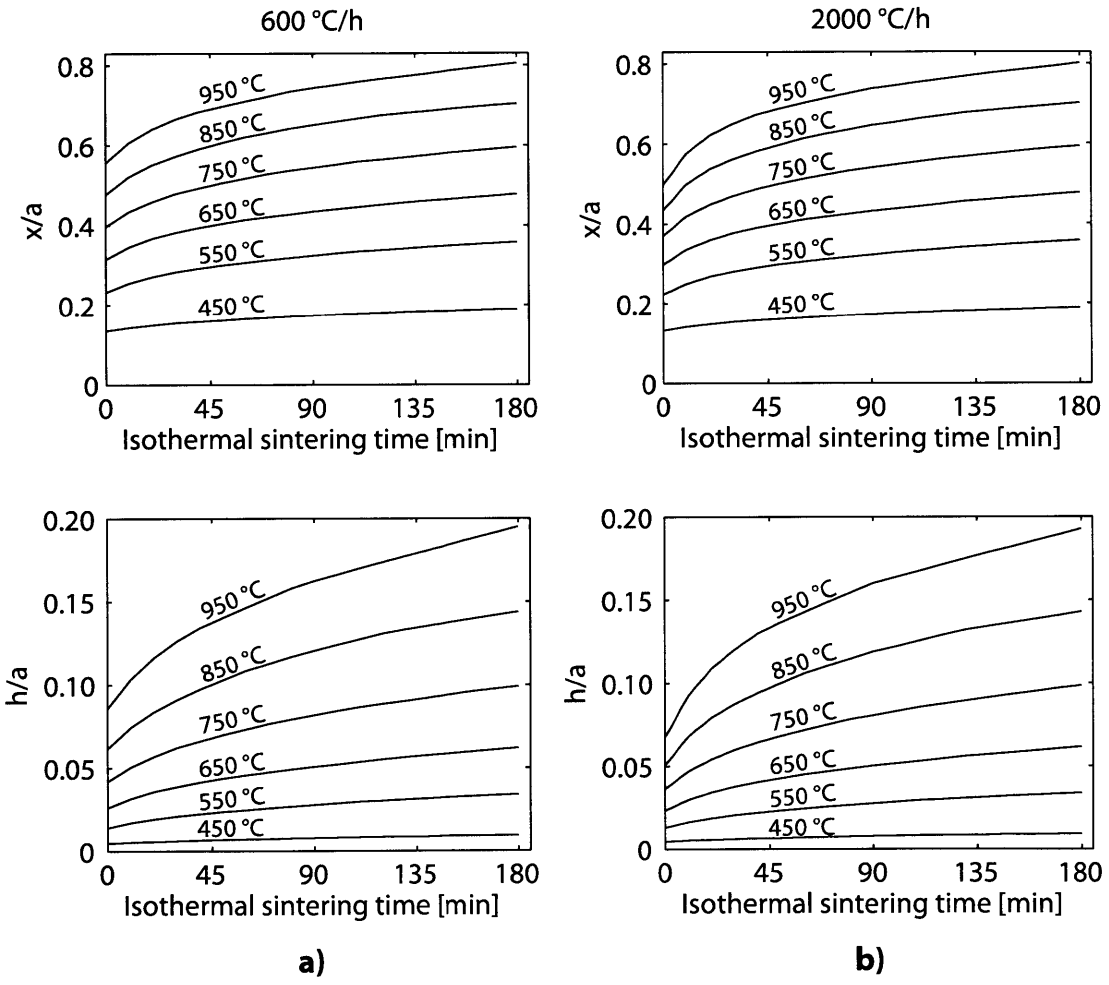

Figure 3.8: **a)** Neck size growth; and, **b)** densification evolution for fine copper samples after the complete sintering process.

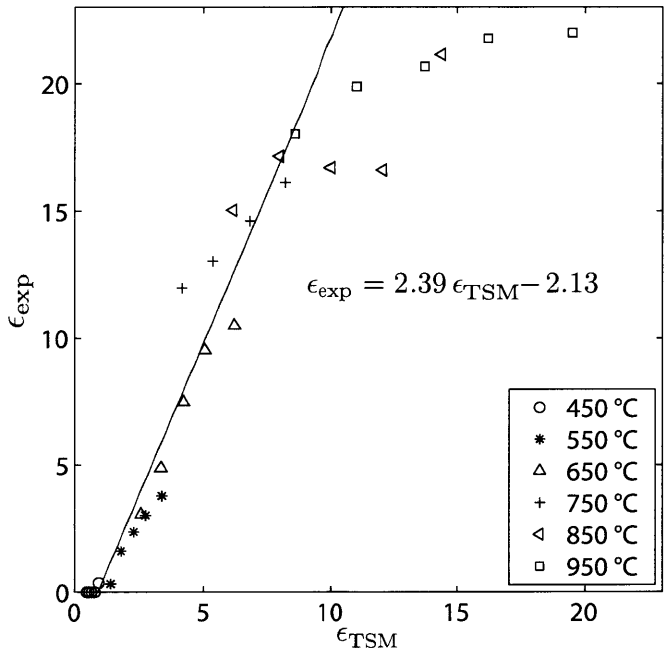

Figure 3.9: Relation between unit cell shrinkage, ϵ_{TSM}, and experimental shrinkage, ϵ_{exp}. The solid line is the best linear fit (with $r^2 = 0.95$) between the variables for $\epsilon_{TSM} < 10\%$.

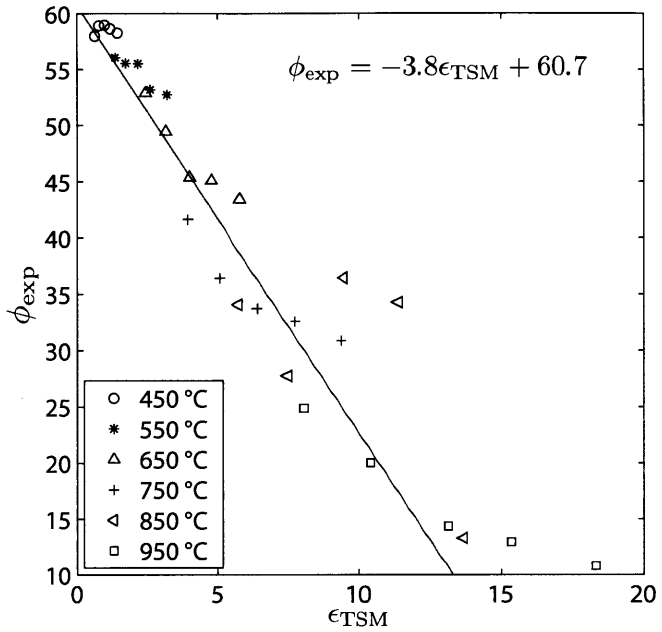

Figure 3.10: Relation between unit cell shrinkage, ϵ_{TSM}, and experimental porosity, ϕ_{exp}. The solid line is the best linear fit between the variables ($r^2 = 0.90$).

son for this change in the slope between the experimental and the predicted unit cell shrinkage resides in the approximations of the sintering models. All of these models assume that $h/a \ll 1$, a condition that becomes less valid as the sintering temperature increases. Nevertheless, it is possible to conclude that the unit cell shrinkage is related to the over-all shrinkage of a sample. Hence, the model and the fit of Figure 3.9 can be used to predict the shrinkage of 10 μm copper sinter.

Figure 3.10 shows the relation between the experimental porosity, ϕ_{exp}, and the shrinkage of the unit cell, ϵ_{TSM}, for the 10 μm copper powder samples. To prepare the samples, metal powder was poured in the graphite molds. The samples were shaken for 5 minutes in an electric shaker table before sintering. However, some samples were prepared without any special packing procedure ('loose-sintered'). The effect of shaking on the properties of the samples (porosity, permeability, capillary pressure, and thermal conductivity) was found to be minimal.

For this case, the linear relation between the variables is preserved along for all the data points. However, there is more dispersion in the data points at larger values of calculated shrinkage. Although many other factors can affect the porosity of the sample during sintering, Figure 3.10 shows that there is a correlation between the shrinkage and the wick porosity.

Porosity of the wick is an important parameter of the thermal conductivity model described in the next chapter. One of the input parameters of this model is the wick's porosity after the heating and cooling procedures, ϕ_0. ϕ_0 is a consequence of the packing of the particles before sintering and the geometric changes that occur during the heating and cooling of these spheres. Although Figure 3.10 was constructed using data for a specific particle size (10 μm), the porosity of a different sample should be independent of the particle size if all the particles have a similar size and shape. Note also that the relation is between two geometric measurements. Thus, under certain conditions, not only is porosity particle-size independent, but also the shrinkage of the sample is scale-independent. The first of these conditions is that of a static wick structure. If all the changes that happen in the wick during sintering are assumed to be a result of neck growth, and thus of shrinkage, then shrinkage dictates the way in which the wick porosity changes. Accordingly, the effect of particle rearrangement on the porosity of the sample is assumed to be negligible.

The second condition is that the static structure is similar within different samples. Because porosity is a scale-independent parameter, similar structures can be assumed between wicks of different particle size if the wicks are prepared similarly. Given the random nature of the initial packing, it is reasonable to expect the porosity of the wicks before sintering to be similar. The veracity of this assumption is confirmed by examining Figure 3.11, a plot of the initial porosities of the samples prepared in this study. All the initial porosities of the samples lie between 55% and 65%.

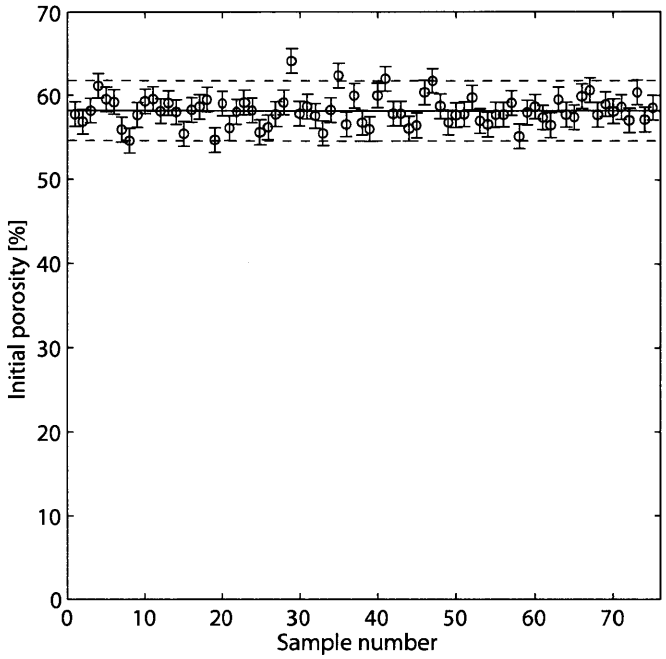

Figure 3.11: Porosity of 75 disk samples of 10 μm copper powder before sintering. The solid horizontal line is the average of the porosities of the samples and the dashed lines encompass a 95% confidence interval in the average porosity. The average porosity of these samples is approximately 53%.

It is important to mention that the average porosity measured in these samples is considerably larger than the average porosity of a randomly packed bed of spheres reported in the literature. When the bed is large enough (as measured by the so-called 'critical bed-size parameter'), the expected porosity is approximately 37% [7]. The samples of this thesis, with a bed-size parameter of more than 27 times the critical bed-size, can safely be considered a large bed. However, the measured porosity in these samples is 40% larger than the one expected for a randomly packed bed. Nevertheless, porosities around 50% to 65% have been reported before in the sintering literature. Peterson et al. [44] reported porosity values of 59%, and 52% for 100-150 μm and 75-100 μm copper sintered wicks, respectively. These values of porosity reported in the work by Peterson et al. were measured after sintering [44]. Yech-Ju Lin et al. [31] showed that the roughness of the particles play an important role in determining the porosity of sintered wicks. They report porosities of 41% for very smooth

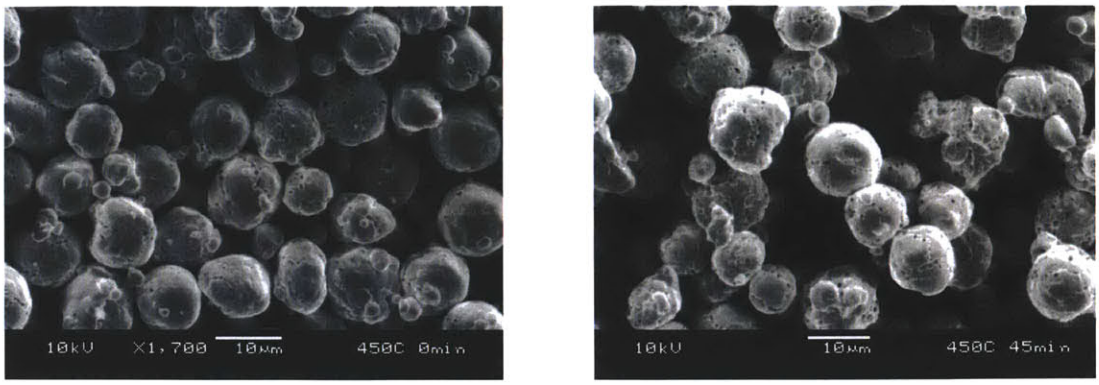

a) b)

Figure 3.12: SEM photographs of sintered wicks in this work. The 10 μm powder was sintered at 450 °C for **a)** 0 minutes; **b)** 45 minutes.

copper spheres, and 66% for rougher, water-atomized powder [31]. The roughness of the particles of this thesis lies between these two powders (Figure 3.12). Thus, roughness can cause open packing due to bridging between groups of spheres.

3.3.3 Sintering of Coarse Copper Powder and Monel Powder

The main difference between the fine copper powder and the coarse copper powder samples is the lack of a unique particle size in the latter. The neck between two small particles will grow faster than the one between two larger spheres. In addition, when two particles of different sizes are in contact, there is not a unique final equilibrium state [61]. The final equilibrium state that the system reaches depends on the relative sizes of the spheres and the relative importance of each of the sintering mechanisms [40]. Thus, the over-all sintering rate becomes strongly dependent on the position of the powder particles. The same behavior can be expected in the Monel samples. As an approximation in modeling the coarse copper and Monel samples sintering behavior, an average particle size was calculated and used in the two-sphere model. However, it is important to mention that the behavior of the actual system will deviate from the results obtained by this approximation, as it has been seen in

Chapter 2 that a broader range of particle size results in a wick with larger variability in its properties.

Figure 3.13 shows the neck size and the densification of the 38-75 μm and 75-106 μm copper samples calculated using the model of this chapter. In this figure, the whole sintering process (ramp up, isothermal sintering and cooling) was considered for different isothermal sintering times and temperatures. As expected, the larger the particles are, the slower the sintering rate (neck growth and densification). Nevertheless, all of the conclusions regarding the ramping up, isothermal sintering and cooling processes for the 10 μm copper powder are valid for the larger particles sizes. Hence, isothermal sintering time dominates the neck growth except for the shortest holding times, where both the ramping up and down effects are comparable to those of isothermal sintering. Therefore, heating up at a faster ramp rate to avoid excessive shrinkage is only beneficial for the shortest sintering times.

Monel is a solid solution of copper in nickel. During sintering, both copper and nickel diffuse in the Monel matrix. Because copper diffuses faster in Monel than nickel, the composition of the alloy will change as sintering progresses. Kuczynski et al. [29] showed that, at least during the first stages of sintering, the faster diffusing metal will precipitate in the neck. Hence, the concentration of the more mobile species will increase in the neck until its concentration gradient causes this species to stop diffusing to the neck. As the slower component diffuses to the neck, the local curvature in this region decreases, decreasing the diffusion of the faster component. The kinetics of the sintering of Monel is more complex than in the case of copper, because now diffusion depends not only on geometry (the curvature gradient) but also in the composition of the system (the concentration gradient).

Figure 3.14 shows the diffusivities of copper and nickel in Monel 400 in the temperature range of interest [42, 43]. In this range, the diffusivities of copper and nickel in Monel are within a factor of 1.6 of each other. For this reason, it was assumed

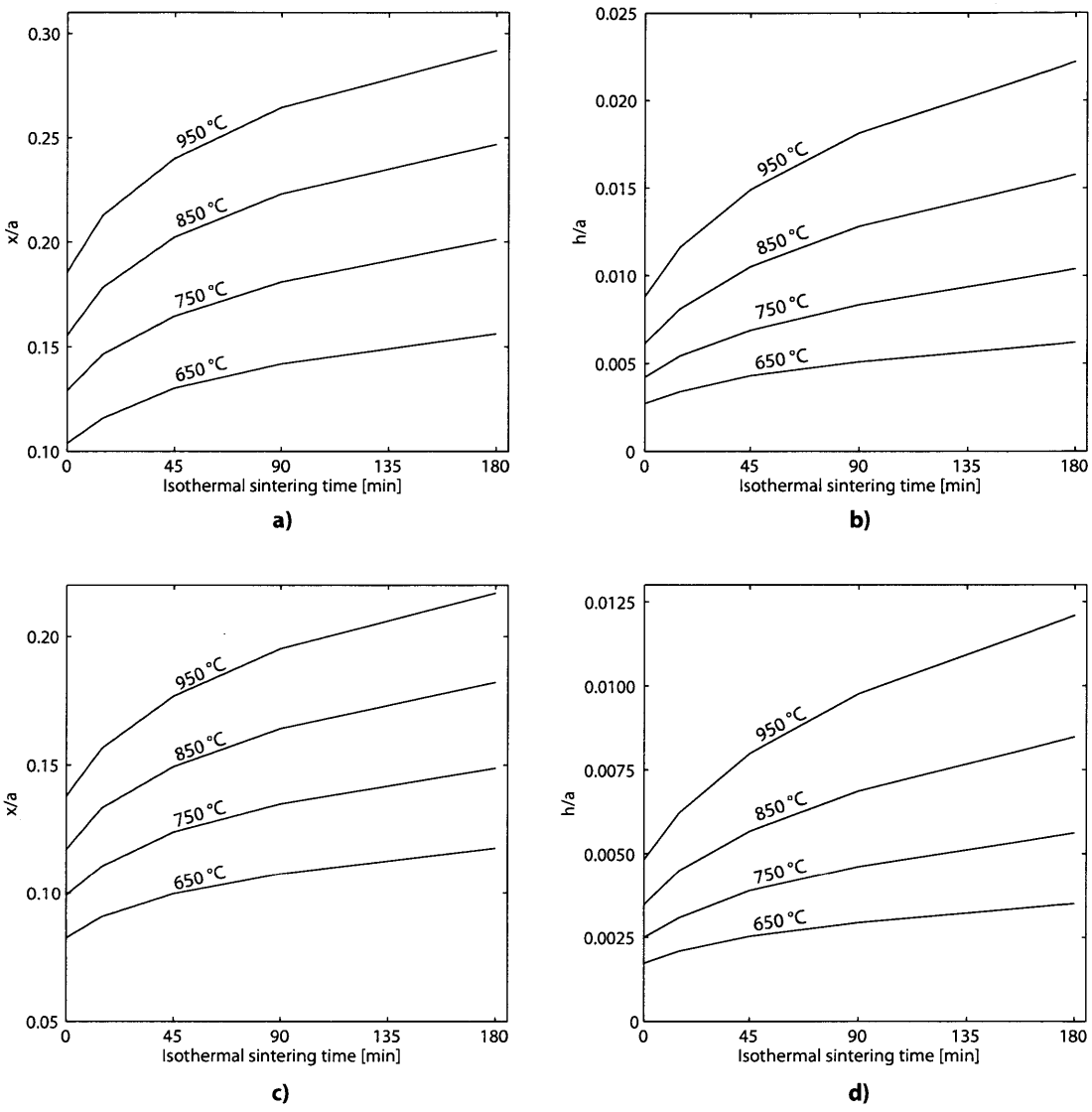

Figure 3.13: Neck growth and densification calculated using the model discussed on the text after all of the sintering process for: **a)** and **b)** 38-75 μm copper samples; and, **c)** and **d)** 75-106 μm copper samples.

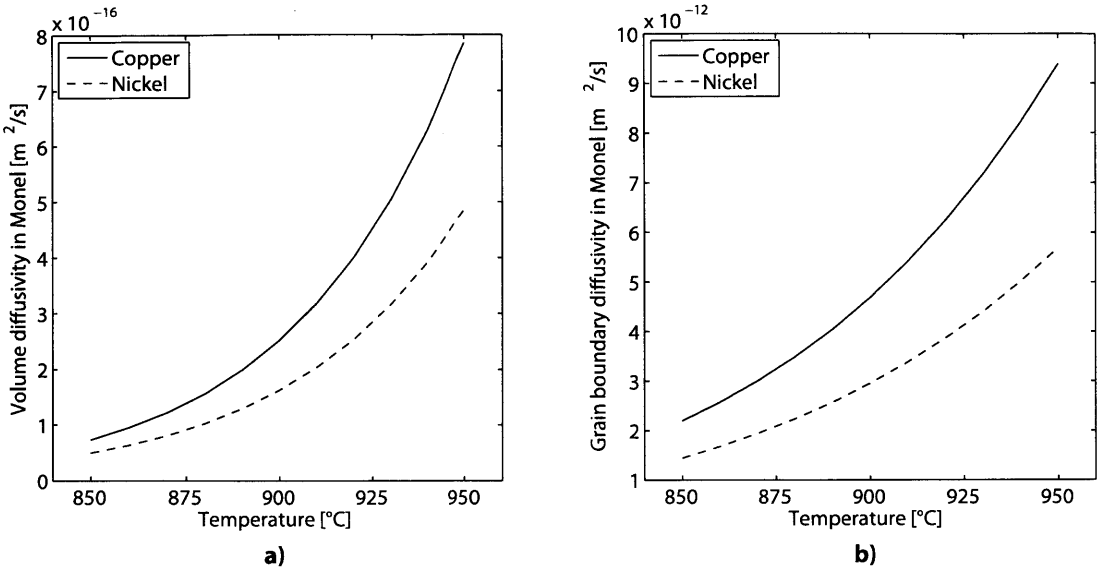

Figure 3.14: **a)** Volume diffusivities (diffusion through the bulk) of copper and nickel in Monel 400. **b)** Grain boundary diffusivities of copper and nickel in Monel 400.

that the composition of the alloy stayed the same during sintering. This assumption is equivalent to stating that the diffusivities of nickel and copper will be treated as the same.

Because copper and nickel have a similar atomic size, diffusion of copper and nickel in nickel-copper alloys occurs by a vacancy exchange. The probability of a copper atom jumping to a vacant site is roughly the same as that of nickel since the mobility of both nickel and copper are roughly equal. Furthermore, because only the material data for diffusion through the grain boundary was readily available, it was considered that only grain boundary diffusion plays a role in the sintering of Monel. Finally, given the complexity determining the surface energy of an alloy, it was assumed here that the surface energy of Monel is the same as that of copper. It has been shown that due to the difference in surface energy of copper and nickel, a spontaneous segregation of elements near the surface occurs [48]. It is common to observe a higher concentration of copper at the surface than in the bulk [48]. Thus, it is not unreasonable to assume Monel surface energy equal to that of copper.

With the assumptions mentioned above, the grain boundary sintering model (Equation 3.13 and 3.14) was used to calculate the neck size between two particles as a function of sintering temperature and time considering the entire sintering cycle (heating process, isothermal sintering at peak temperature and cooling process following the cooling profile of the furnace). Results can be found in Figure 3.15, which shows the neck size and densification of Monel for the different sintering times analyzed in this work.

3.4 Chapter Summary

A general overview of the kinetics of sintering was presented. Sintering arises from a difference in the diffusion potential of surfaces with different curvatures. Various transport mechanisms can be active concurrently, moving material from the larger curvature to the lower curvature zones.

Generalized charts of nondimensional time and neck growth exist in the literature (e.g. [18, 61]). In this chapter, the specific cases of copper and Monel were studied. Heating and cooling processes were also included. It was found that any effect caused by a faster heating rate is lost in the first minutes of isothermal sintering. For multiple sintering processes, the effect of heating and cooling was found to be negligible, except when the time spent during heating/cooling is comparable with the isothermal sintering time. Thus, multiple sintering processes can be approximated by a single sintering at the same hold temperature but for a longer period of time. The time spent at the peak temperature being the summation of the time spent at this temperature in the multiple sintering routes.

The next chapter relates the neck radius and length of two sintered spheres to the effective thermal conductivity of a wick assumed to be composed of multiple unit cells randomly connected.

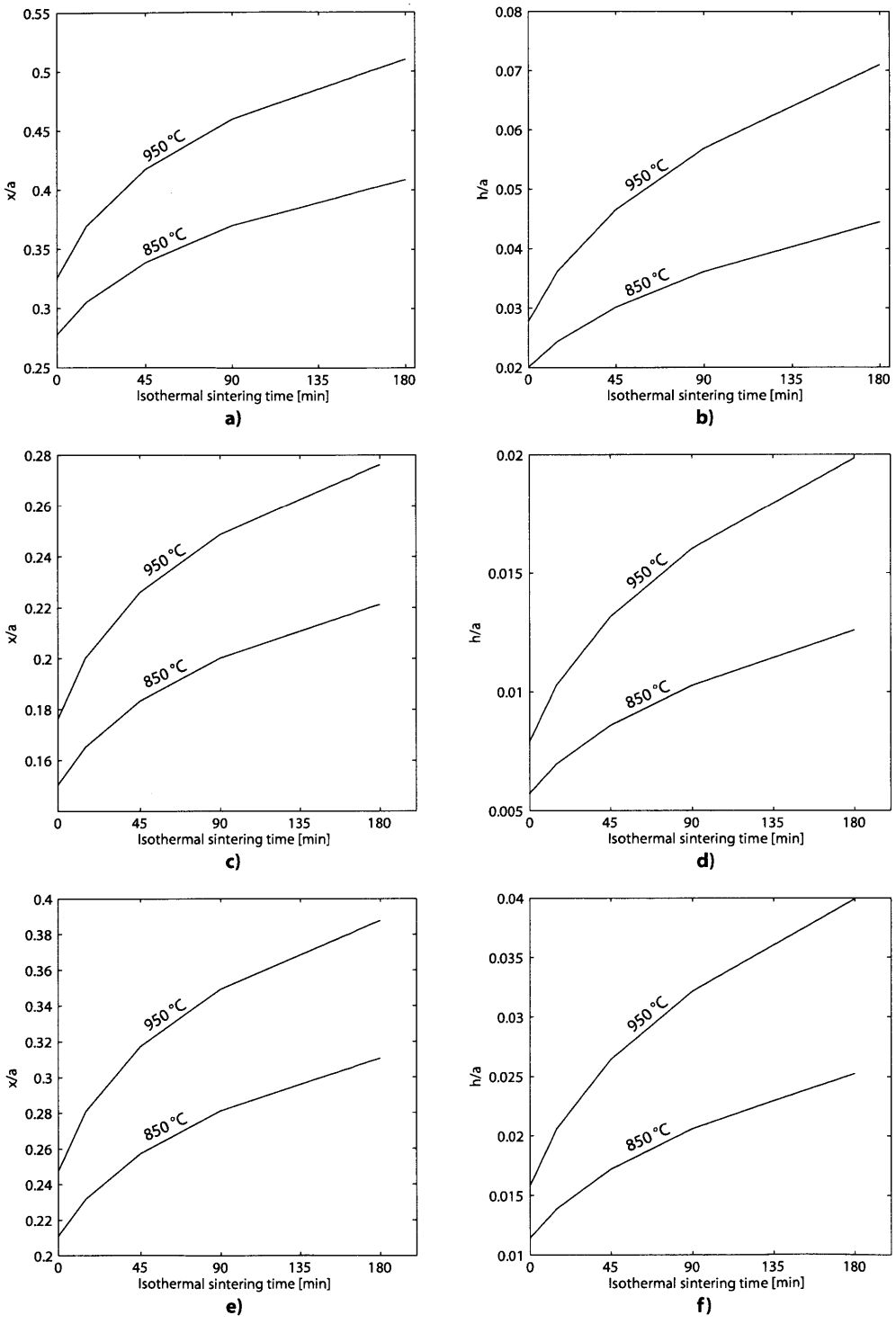

Figure 3.15: Neck growth and densification after the complete sintering process for Monel powder based on the model described in the text. **a)** and **b)** -22 μm; **c)** and **d)** 22-33 μm; and, **e)** and **f)** -33 μm particles.

Chapter 4

Thermal Conductivity Model

This chapter describes a model used to explain and predict thermal conductivity of sintered wicks. The model is based on the thermal resistance of the unit cell introduced in Chapter 3. This unit cell takes into account the so-called thermal constriction resistance due to the neck between the two particles. Then, an effective wick thermal resistance was obtained by simulating the unit cell in a finite element analysis software (COMSOL). Finally, the unit cell resistance was included in a random thermal resistor network as a means to simulate a sintered wick and thus, obtain its effective thermal conductivity.

4.1 Thermal Resistance of the Two-Sphere Model

A unit cell composed of two half spheres bonded by a neck was modeled in a finite element analysis software (COMSOL), and is shown in Figure 4.1. All the boundaries of the unit cell, except for the bases of the hemispheres, were assumed to be adiabatic. The adiabatic boundary condition is represented with gray color in Figure 4.1. Different temperatures were specified at the remaining surfaces of the unit cell. One of these surfaces was held at a constant temperature of 273 K (blue surface in Figure 4.1), while the other was held at 283 K. The total normal outward heat flux across one of these surfaces, $\dot{Q}$, was calculated in COMSOL and used to obtain the unit cell

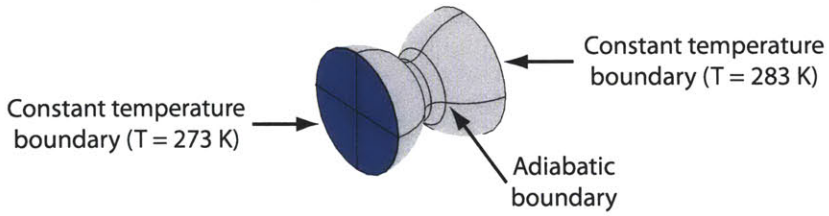

Figure 4.1: COMSOL model constructed to obtain the effective thermal resistance of the unit cell. A gray surface represents an adiabatic boundary condition. Temperature of the blue surface was specified as 273 K, while temperature of the other surface was set at 283 K.

thermal resistance, R_{th}, according to

$$R_{th} = \frac{\Delta T}{\dot{Q}} \tag{4.1}$$

where $\Delta T(= 10)$ K is the temperature drop across the unit cell.

Six different neck sizes were simulated and fitted to obtain an expression relating the neck size and the thermal resistance of the unit cell. The results are plotted in Figure 4.2. The abscissa in this figure is normalized by the thermal resistance of a cylinder, R_{cyl}, of radius a and length equal to that of the unit cell ($l_{uc} = 2(a - h)$). The insert in Figure 4.2 shows the temperature profile in two different unit cells. As expected, the neck is the largest resistance in the unit cell, since practically all the temperature drop in the unit cell happens in this region.

The equation imbedded in Figure 4.2 is a normalized relation between the thermal resistance of the unit cell and the radius of the neck. Normalization of variables makes this equation a general expression valid for the unit cell shown, regardless of the thermal conductivity of the material considered.

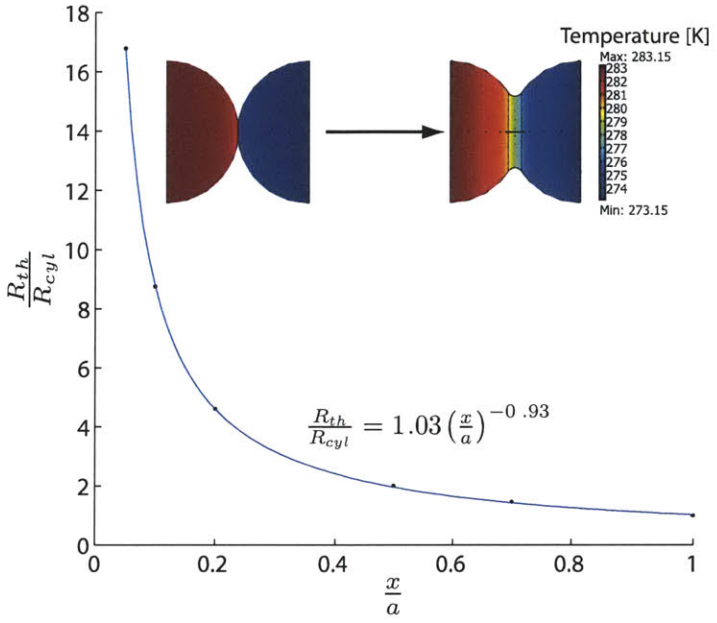

Figure 4.2: Normalized thermal resistance of a unit cell as a function of its neck size. The blue line shows the least-squares fit for the data. The least-squares fit equation expresses the normalized thermal resistance, $\frac{R_{th}}{R_{cyl}}$, in terms of the normalized neck radius, x/a. Insert shows the thermal profile in two unit cells.

4.2 Random Resistor Network Model

4.2.1 Description of the Model

The unit cell approach described above does not address the multiple connections between the particles that can be formed in a sintered wick. These connections form a continuous chain of metal particles connecting the opposite faces of a sintered wick. The spatial relationship among the particles becomes important in the determination of the sinter's thermal conductivity because it defines the heat flow path. This path is longer and more convoluted than a single column of unit cells connecting the opposite faces of the wick because there may be holes that heat must flow around.

To model the random positioning of the particles and the connections between particles in a wick, a randomized thermal resistor network was constructed. The wick was modeled by a three-dimensional cubic array (which will be referred to as the 'structural matrix'). Each cell of the structural array represents a node in a thermal resistor circuit. Every cell of the structural matrix was randomly assigned a number '0' or '1'. A cell with a '1' represents a node in the resistor network occupied by a particle, while a '0' represents a gap in the network. A binomial probability distribution was used to assign these numbers. The probability of obtaining a '0' from the binomial distribution was selected so the porosity of the modeled wick matches the experimental porosity of the wick samples for $t = 0$ (i.e. ϕ_0).

Every node in the circuit was connected to its closest six neighbors in the matrix's orthogonal directions (at the right and left of the node, above and below it, and in front and at the back of the node) by a 'weighted edge'. The weight of an edge was set to be equal to the inverse of the thermal resistance (the thermal conductance) connecting two nodes. The edge weight depends on the number assigned to the nodes connected by that edge. Two adjacent '1's in the structural matrix were connected by the thermal conductance of two particles bonded by a neck. A '1' next to a '0' was connected by the conductance between a sphere and an air gap.

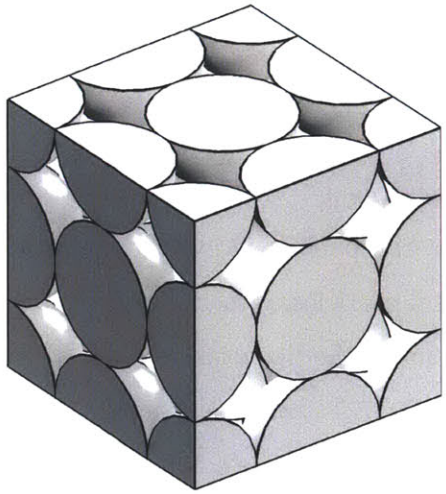

Figure 4.3: A $3 \times 3 \times 3$ representation of the modeled wick. The particles were assumed to be packed as a simple cubic crystal.

Figure 4.3 shows a $3 \times 3 \times 3$ schematic representation of the modeled sinter. In this example there are no missing particles. The model takes into account the difference in the thermal conductance of complete and incomplete spheres.

From the geometry of the model (e.g. Figure 4.3), the porosity of the modeled wick, ϕ, is given by

$$\phi = 1 - \frac{V_{sph}}{[2(s-1)(a-h)]^3} \tag{4.2}$$

where V_{sph} is the total volume occupied by the particles; s is the size of the structural matrix (in 3D the size of the matrix is $s \times s \times s$); a is the radius of the particles; and, h is the shrinkage parameter (see Figure 3.1).

A simple cubic (SC) crystal has a low packing factor and, as a consequence, high porosity. A wick structure of unconsolidated particles packed in a simple cubic crystal has a porosity of 47.64%. All of the initial porosities, ϕ_0, that are higher than 47.64% can be modeled by increasing the fraction of '0's (gaps) in the structural matrix. However, lower porosities will be impossible to match using an SC array. Specifically,

for the 10 μm copper powder the model will not be able to match the low initial porosities observed above 650 °C, which results in an overestimation of the thermal resistance. This effect becomes more pronounced as the sintering peak temperature increases. To overcome this increase in the calculated thermal resistance, structures with larger packing factors were also considered. The effective thermal resistance of unit cells based on body-centered cubic (BCC) and face-centered cubic (FCC) crystals were also obtained. As expected, for a similar neck size, the thermal resistance of these structures is lower than the SC resistance. However, a model based on these structures overpredicts the over-all thermal resistance due to an overlap of the unit cells. Details about this overlap are explained in Appendix B.

4.2.2 Effective Thermal Conductivity Calculation

The structural matrix and the thermal conductance of the edges connecting the nodes of this matrix were used to assemble the weighted Laplacian matrix, $\mathbf{K}$, of the random resistor network. Each entry, $k_{i,j}$, in the Laplacian matrix was calculated in the following manner [54]:

$$k_{i,j} = \begin{cases} \sum c_n \text{ on the edges meeting at node } j & \text{if } i = j \\ -c_m & \text{if } i \sim j \text{ via edge } m \\ 0 & \text{otherwise} \end{cases} \tag{4.3}$$

where $k_{i,j}$ is the entry in the position (i, j) in $\mathbf{K}$; c is the conductance of an edge connecting a pair of nodes i and j; $\sum c_n$ is the summation of the conductances of all the edges n meeting at node j; $i \sim j$ means that node i is adjacent to node j; and, c_m is the conductance of edge m between node i and j.

The Laplacian matrix records the connections between nodes and the thermal conductance of the edges connecting them. This thermal conductance matrix is part

of Ohm's law in matrix form

$$\mathbf{KU} = \mathbf{f} \tag{4.4}$$

where $\mathbf{U}$ is the potential difference matrix and $\mathbf{f}$ is the transport rate matrix. In the case of a thermal circuit, $\mathbf{U}$ contains the difference in temperature across the edges of a network and $\mathbf{f}$ contains the net heat transfer rate out of each node.

The weighted Laplacian matrix, $\mathbf{K}$, is singular. A vector, $\mathbf{u}$, having the form $\mathbf{u} = (a, a, a, \ldots, a)$, with a being any constant, is in the nullspace of $\mathbf{K}$. It is necessary to ground at least one node so $\mathbf{K}$ becomes invertible. For the present model all the nodes in the first row of the structural matrix were grounded and the potential (temperature) of the nodes in the last row was set at 10 °C with respect to the grounded nodes. With these conditions, Ohm's law (Equation 4.4) was solved to obtain the net heat flow rate out of every node, $f_{i,j}$. The total heat flow rate coming to the nodes of the last row of the structural array was used to calculate the thermal resistance of the sinter, $R_{th,eff}$, as in Equation 4.1. The relation between the random network thermal resistance and its effective thermal conductivity, κ_{eff}, is given by

$$\kappa_{eff} = \frac{1}{2(s-1)(a-h)R_{th,eff}}. \tag{4.5}$$

The `MATLAB` code used to calculate the effective thermal conductivity of a three-dimensional random resistor network can be found in Appendix C.

4.2.3 Effect of the Structural Matrix Characteristics

Percolation is a common characteristic of random resistor networks such as the one explained in the previous section. In systems composed of high and low conductivity elements, percolation refers to a sudden, considerable change in conductivity when the fraction of high conductivity elements is larger than a certain threshold (the percolation threshold). This high conductivity results from the formation of a continuous

chain of low resistivity resistors that connects the opposite sides of the network. However, if the fraction of low resistivity elements is lower than the percolation threshold, then these elements form isolated 'islands' of high conductivity. So that in this case, the over-all conductivity of the network is low [59].

Sintered wicks are always percolated. Thus, there exists a minimum fraction of particles that needs to be present in the modeled wick to ensure that the system is percolated. This minimum fraction can be calculated by considering a situation in which all but one of the planes (horizontal or vertical) of the structural matrix are fully occupied by particles and there is at least one additional particle in the plane that is not completely occupied. Thus, the fraction of particles, φ, that guarantees percolation is given by

$$\varphi = \frac{(s-1)s^2 + 1}{s^3} \tag{4.6}$$

where s is the size of the structural array. Note that φ is not the complementary function of the porosity of the wick, ϕ, of Equation 4.2 (i.e. $\varphi \neq 1 - \phi$), because the latter takes into consideration whether the spheres are complete or not and thus, depends on the position of the particles. However, Equation 4.6 imposes a condition on the maximum value of porosity that can be modeled without having a sudden change in thermal conductivity derived from percolation.

In addition to the fraction of high and low thermal conductivity elements, the actual structure of the random network is another parameter that has a significant impact on the value of the calculated conductivity. Because of the law of large numbers, meaningful predictions of thermal conductivity result from averaging multiple random networks. Therefore, different structural matrices have to be constructed. Every time a new structural matrix is generated, the average value of the predicted thermal conductivity changes. If few networks are averaged, then the value of the predicted thermal conductivity can change dramatically with each new network generated. Once enough networks have been considered, the addition of a new network

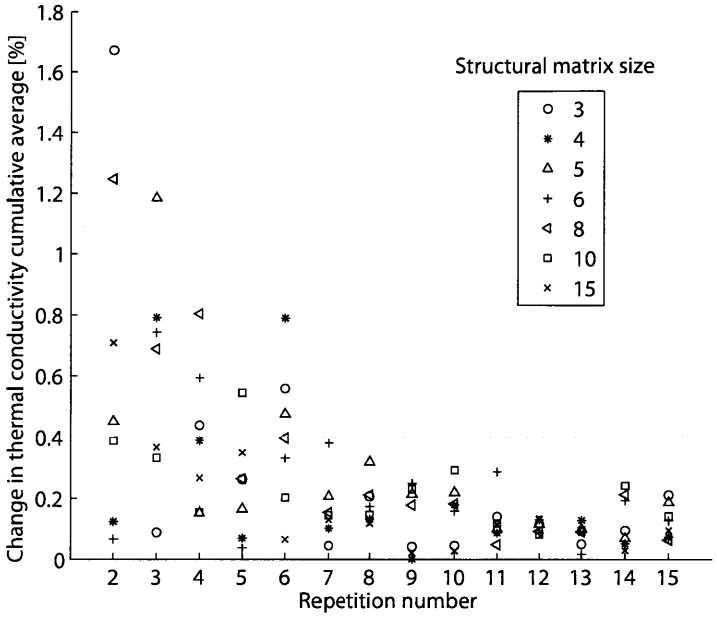

Figure 4.4: Change in the thermal conductivity cumulative average due to the number of networks averaged for different structural matrix sizes. The porosity of all the matrices was kept constant at 50%. The dashed line marks a change in the thermal conductivity cumulative average of 0.4%. Above six repetitions the change in cumulative average is below 0.4% for any structural matrix size.

will not significantly change the average value of the predicted thermal conductivity. Figure 4.4 shows the change in the cumulative average of the calculated thermal conductivity as a function of the number of averaged networks and the size of the structural matrices averaged. To construct Figure 4.4, at least two different random structural matrices were generated and the average of the conductivity of these matrices was calculated. A third random network was constructed and the change due to this third network in the average thermal conductivity was calculated. Additional networks were generated and the change in the thermal conductivity cumulative average was computed and plotted in Figure 4.4. All the matrices generated had the minimum number of particles of Equation 4.6.

It can be seen in Figure 4.4 that averaging seven or more different networks will not change the mean value of the thermal conductivity by more than 0.4%.

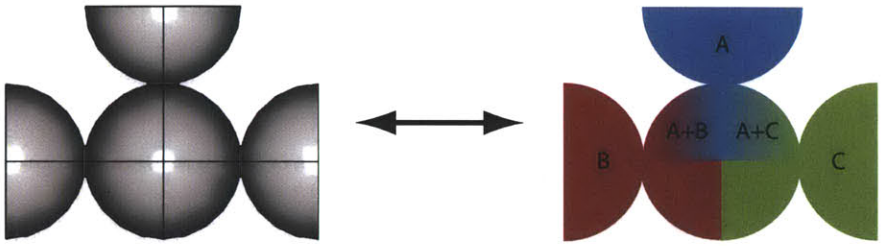

Figure 4.5: A central node with a particle connected to three other nodes with particles. There are three unit cells, labeled 'A', 'B' and 'C' and differentiated by color. Unit cells 'A' and 'B', and 'A' and 'C' overlap in the regions shown.

4.3 Comparison between the Random Network Model and COMSOL Simulations

A consequence of defining the unit cell of the thermal conductivity model based on the two-sphere model as shown in Figure 4.1 is an overlap of the unit cells in the nodes. Figure 4.5 shows a simple geometry constructed with three unit cells, 'A', 'B' and 'C', where the overlap between them can be seen. As more unit cells are connected to a single node, more overlap will exist in that node, the worst case being that of six connections to a single node. Overlapping of unit cells means that the effective thermal resistance predicted from the model will be larger than in a real wick.

A second consequence of defining the unit cell as that of Figure 4.1 is that a node is always in the center of a sphere. This constraint in the model forces the heat flux to travel to the node in the center of a particle, and then to move from there to the rest of the particles connected to that node. In reality, the heat flux lines are free to curve before reaching the center of the particle. For this reason, the model is expected to overestimate the thermal resistance when the heat flux travels between nodes that are not directly connected by a unique unit cell.

In order to check the effect of the overlap of unit cells, as well as the effect of the position of the nodes, the geometry of Figure 4.6 was constructed. For this ge-

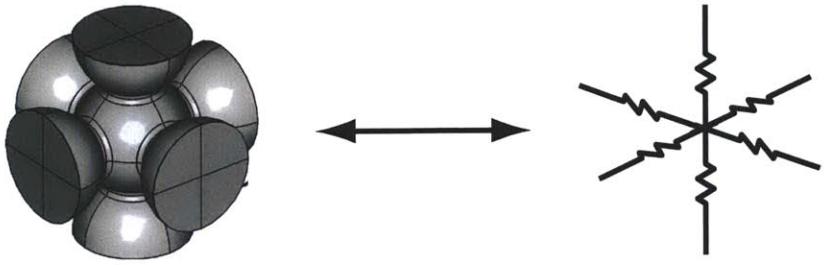

Figure 4.6: COMSOL and resistor network representations of a particle connected to its six closest neighbors. For this geometry, $x/a = 0.5$.

ometry, the effective thermal conductivity was calculated using the random resistor network and a COMSOL simulation. In Figure 4.6 a particle is connected to its six closest neighbors, which represents the worst case of overlapping between unit cells. In the resistor network model, this intersection is represented by six unit cell thermal resistances connected to a central node.

The temperature difference between two of the nodes of Figure 4.6 was set to 10 °C. The rest of the surfaces were set to be adiabatic. The total normal heat flux through one of the non-adiabatic surfaces was calculated and used to compute the equivalent thermal resistance using Equation 4.1. Two cases were considered. In one case, the temperature difference was set in faces opposed to each other. The effective thermal resistance calculated in this case is designed $R_{th,\text{across}}$. In the second case, the faces considered were perpendicular to each other and the resistance calculated is called $R_{th,\text{bent}}$. In both cases the resistor model overestimates the effective thermal resistance as expected. $R_{th,\text{across}}$ calculated from the network model is 1.4% larger than the COMSOL result. $R_{th,\text{bent}}$ from the resistor network is 7.9% larger, because of the additional effect of forcing the heat flux to reach the node in the middle of the particle before being allowed to change direction. However, the solutions of the random network were obtained more than 3000 times faster than the COMSOL solutions.

In summary, the error in the model results derived from the overlapping of unit cells and the position of the network nodes is an underprediction in the thermal con-

Table 4.1: Initial porosities for 10 μm copper wicks

Sintering temperature	Initial porosity
450 °C	58%
550 °C	56%
650 °C	53%
750 °C	42%
850 °C	34%
950 °C	25%

ductivity of approximately 10%. Nevertheless, the computation time spent solving the network model is considerably shorter than the time involved in the full-field finite element simulations.

4.4 Results of the Thermal Conductivity Model

4.4.1 Fine Copper Sintered Wick Thermal Conductivity

The model described in this chapter was used to calculate the thermal conductivity of 10 μm copper powder sintered wicks. The size of the structural matrix was $4 \times 4 \times 4$ and eight different networks were averaged to compute the thermal conductivity. The sintering process simulated is the same as the one explained in Chapter 2. Results are show in Figure 4.7 as solid lines. In this figure, thermal conductivity is plotted as function of isothermal sintering time from 0 minutes to 180 minutes. Plots are shown as level sets of sintering peak temperatures from 450 °C to 950 °C. The initial porosity of the modeled wick for each sintering temperature was matched with the experimentally measured porosity. Values of the initial porosities are shown in Table 4.1. Markers in Figure 4.7 show the experimental measurements of Chapter 2.

As expected, the thermal conductivity model overestimates the thermal resistance

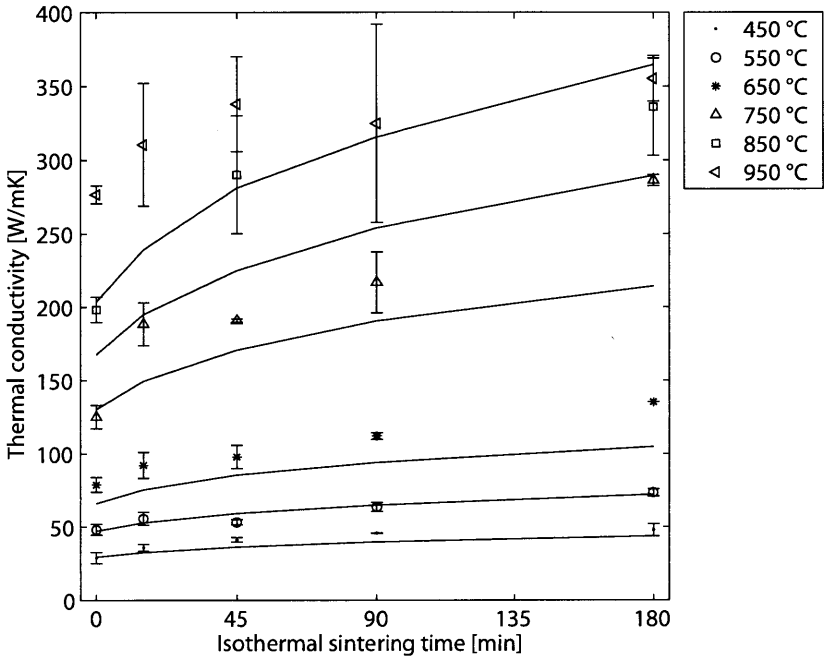

Figure 4.7: Predicted and experimental thermal conductivity for 10 μm copper powder. The initial porosity of the modeled wicks was matched to the experimental porosity results of Chapter 2 (Table 4.1). The calculated thermal conductivity is shown as a solid line for each peak temperature, from 450 °C to 950 °C. Markers show experimental measurements also from 450 °C to 950 °C.

of the wick and, thus predicts a lower thermal conductivity than that observed experimentally. The model becomes less accurate as the sintering hold temperature increases, because the difference between the modeled wick porosity and the experimentally measured porosity also increases. Additionally, at high temperatures and consequently, low porosities, more spaces are occupied by particles and there exists more overlap between unit cells. However, the model captures the trend of increasing thermal conductivity with both increasing peak sintering temperature and hold time. For sintering temperatures below 750 °C, the change in thermal conductivity as the hold time increases is relatively small, and thus, the slope of these curves is small. For sintering temperatures above 750 °C, the slope of the curves increases, which represents a larger change in thermal conductivity with sintering time than in the lower temperature cases. The model captures this change in slope.

The accuracy of the thermal conductivity prediction decreases as the sintering temperature increases. The largest error in the prediction of the thermal conductivity is approximately 26%, but it is below 15% for most of the cases. The model is especially useful to predict thermal conductivity in the temperature range where shrinkage is low. This temperature range is also characterized by low shrinkages. Therefore, good connection between the wick and its container is expected, and thus, the system can sustain high capillary pressures. At high temperatures, the error becomes larger than in the lower temperature case, with more instances where the error is above 20%.

The thermal conductivity model and the experimental results can be used to create a chart of thermal conductivity as a function of sintering temperature and time. This chart will show different combinations of sintering time-temperature that can be followed to achieve a similar thermal conductivity in 10 μm copper powder wicks. Figure 4.8 shows a contour plot of thermal conductivity against sintering time and temperature. The x-axis in Figure 4.8 spans from 0 to 300 minutes. The black dashed line in this plot marks the maximum value of shrinkage before separation

between the sinter and the wall of its container (copper tube) occurs (the 'critical shrinkage'). As can be seen in Figure 4.8, below the critical shrinkage level it is possible to reach a higher thermal conductivity by sintering at a high temperature for a shorter period of time. The opposite is not possible. For example, it is possible to reach a conductivity of 75 W/m-K by sintering at 650 °C for 0 minutes, but is not possible to reach that conductivity at 550 °C without first reaching the critical shrinkage.

4.5 Generalized Charts

A thermal conductivity chart such as the one shown in Figure 4.8 is valid only for 10 μm copper powder sintered wicks. A chart that is valid for any particle size of any material would be extremely useful when designing systems based on the thermal conductivity of a sintered wick. Therefore, this section generalizes the model of Chapter 3 by means of dimensionless parameters. The relevant parameters are then used as inputs in the thermal conductivity model. The result is a generalized design chart of thermal conductivity as a function of sintering time and temperature.

4.5.1 Dimensionless Parameters

As explained in Chapter 3, the functional form of the neck radius as a function of sintering temperature and time, $x(T,t)$, is the same regardless of the mechanism considered. This functional form is given in Equation 3.5. From this equation, it is possible to define two dimensionless parameters. The first one, called the reduced time, t^*, is given by

$$t^* = \frac{C(T)}{a^m} t \,. \tag{4.7}$$

The reduced time of Equation 4.7 depends on the mechanism considered, since each mechanism has its own form of $C(T)$ and its own value of the exponent m. In surface diffusion controlled sintering models, such as the one described in Chapter

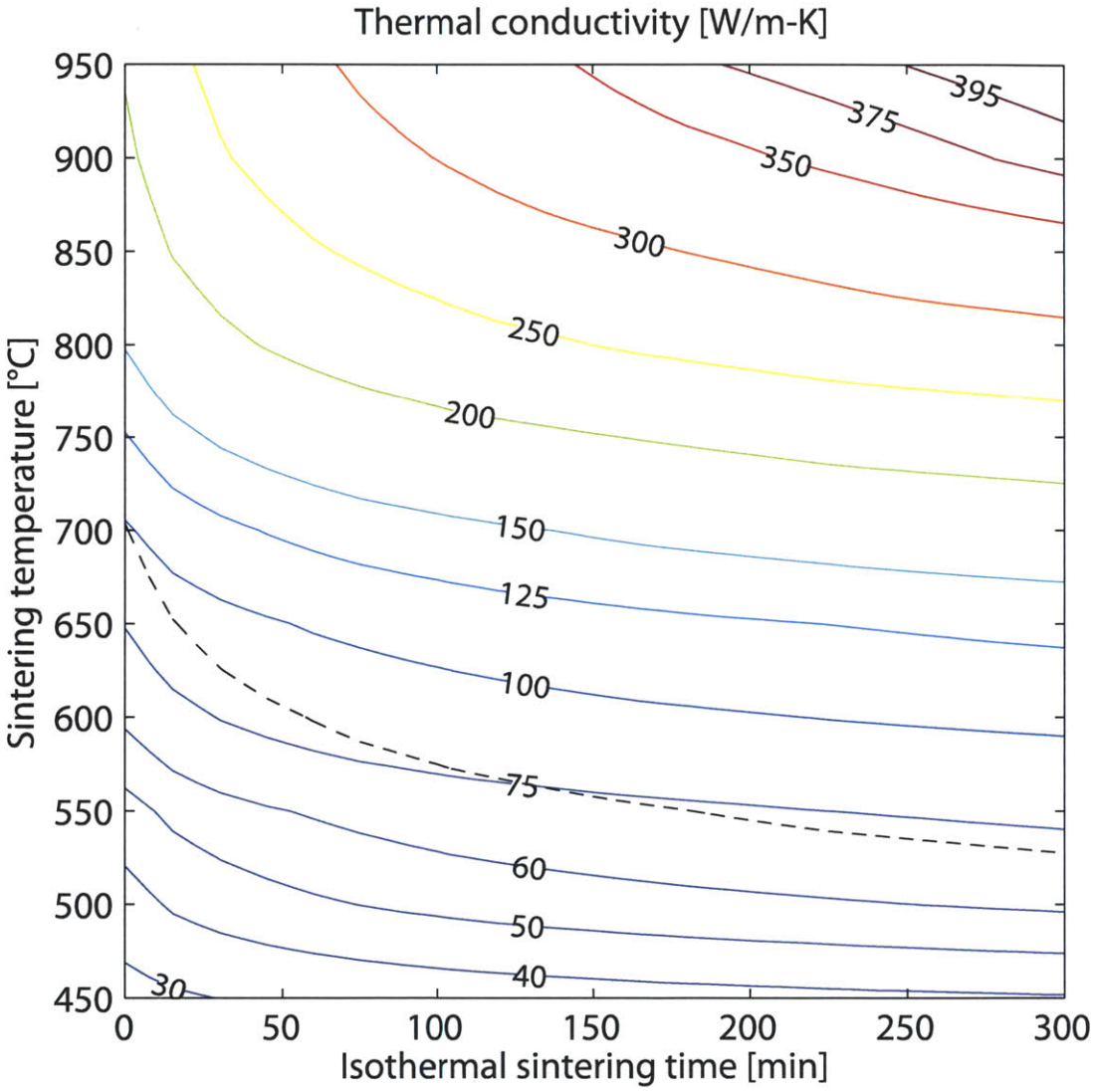

Figure 4.8: Contour plot of thermal conductivity as a function of sintering time and temperature for 10 μm copper powder wick. The model of this chapter was used to predict thermal conductivities from 0 to 300 minutes spanning from 450 °C to 950 °C. The black dashed line in this plot marks the critical shrinkage of the wick.

3, only surface diffusion and grain boundary diffusion are assumed to participate in the sintering process as coupled mechanisms. For this kind of model, it is common in sintering literature (e.g. [9, 61]) to define the reduced time for surface diffusion. Then, the reduced time is given by

$$t^* = \frac{D_{SD}\gamma M\Omega^{1/3}}{RTa^4}t \tag{4.8}$$

where D_{SD} is the surface self-diffusion coefficient of the material being sintered; γ is the material surface energy; M is the molar volume; Ω is the atomic volume; R is the gas constant; T is the sintering temperature; t is the sintering time; and, a is the radius of the particle.

The second parameter that comes from Equation 3.5 is the dimensionless neck size, given by

$$x^* = \frac{x}{a}. \tag{4.9}$$

The final dimensionless parameter is Γ. Γ is the ratio of the grain boundary diffusivity to the surface diffusivity of a material and is given by Equation 3.10. This equation is reproduced here:

$$\Gamma = \frac{\delta_{GBD}D_{GBD}}{\delta_{SD}D_{SD}}.$$

It is possible to write one of these parameters as a function of the other two. Because sintering temperature and time are the variables that can be controlled in the manufacturing of sintered wicks, reduced time is considered to be the independent variable. The dimensionless neck radius is a consequence of the sintering time and temperature selected, and thus becomes a dependent variable. The manner in which the sintering time and temperature affect the neck radius depends on the material selected. Different materials will have different curves of dimensionless neck radius as a function of reduced time. Therefore, the reduced neck can be written as a function of the reduced time and of Γ, $x^* = x^*(t^*, \Gamma)$. A dimensionless ramp rate is not considered in this analysis, because it was found to have a relatively small effect on

the neck growth (Chapter 3). In addition, the heating and cooling processes are not considered in the generalized charts because these processes are not isothermal and are not taken into account in the reduced time (recall that $t = 0$ is the beginning of the isothermal sintering time, after the heating process). It is expected that the results of the model deviate from the experimental values at small sintering times, and thus small reduced times.

4.5.2 Generalized Thermal Conductivity Chart

Besides the neck radius, x, between the particles, the thermal conductivity of a wick depends on the thermal conductivity of the material being sintered, as well as the porosity of the wick. The former variable can be included in the dimensionless analysis as

$$\kappa^* = \frac{\kappa}{\kappa_{\text{material}}} \tag{4.10}$$

where κ^* is the dimensionless thermal conductivity; κ is the thermal conductivity of the wick; and κ_{material} is the thermal conductivity of the material being sintered.

A generalized treatment of porosity was described in Chapter 3. In that chapter, it was shown that the experimental relation between the porosity of the 10 μm copper wicks and the theoretical shrinkage can be assumed to be the same for any material. This assertion assumes that the initial porosity is the same for all randomly packed wicks and that the change in porosity during sintering is a consequence of shrinkage only, and not of rearrangement of the particles. Thus, it is possible to determine the thermal conductivity of a particular material and particle size using this relation between porosity and theoretical shrinkage. If this thermal conductivity is plotted using the dimensionless parameters of this chapter, then the plot will be a generalized thermal conductivity chart.

Figure 4.9 shows a generalized thermal conductivity plot. The dimensionless ther-

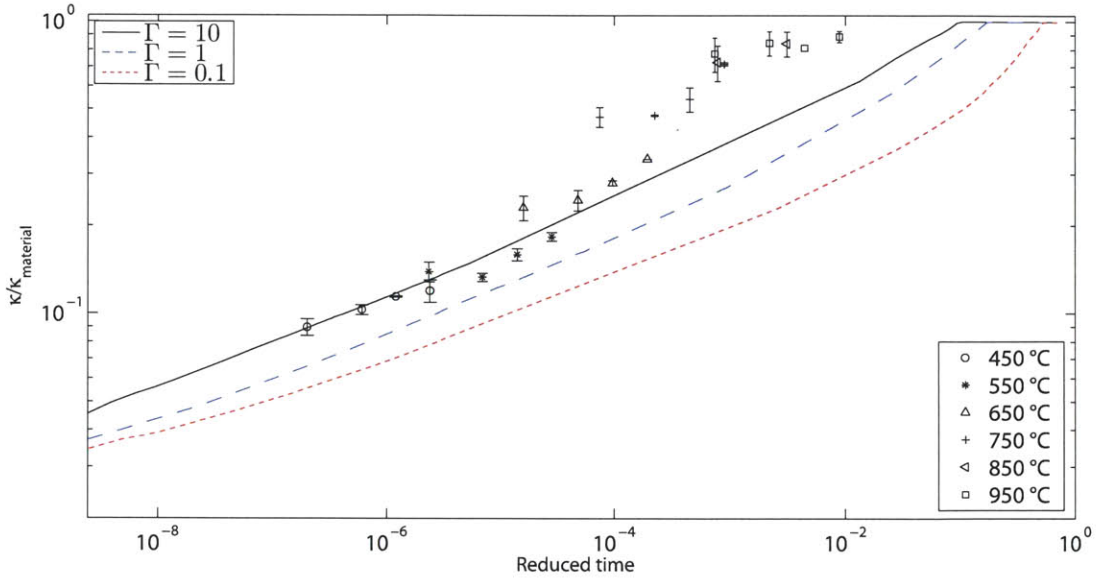

Figure 4.9: Dimensionless conductivity, $\kappa/\kappa_{\text{material}}$ (where $\kappa_{\text{material}} = \kappa_{\text{Cu}}$), as a function of reduced time (t^*). Markers show the experimental results.

mal conductivity of the wick is plotted against the reduced sintering time. In this plot, for the sake of generalization, the effect of the heating and cooling processes was neglected. The three curves represent different values of Γ. For copper, low values of Γ are related with high sintering temperatures, and vice versa. Reduced time includes the effect of both sintering temperature and sintering time. For copper, increasing the sintering temperature while keeping the hold time fixed increases the value of the reduced time. For this reason, equal thermal conductivities can be reached by sintering at low values of Γ for longer reduced times, or by sintering at higher values of Γ for shorter reduced times. The markers in Figure 4.9 show the experimentally measured thermal conductivity.

Figure 4.9 shows that the accuracy of the generalized chart is fair (underprediction of approximately 24%) for the low temperature measurements (450 °C, 550 °C,). However, the thermal conductivity is more underpredicted at higher temperatures. In addition to the previously discussed sources of error, ignoring the heating and cooling processes is a source of error that should lead to further underprediction of

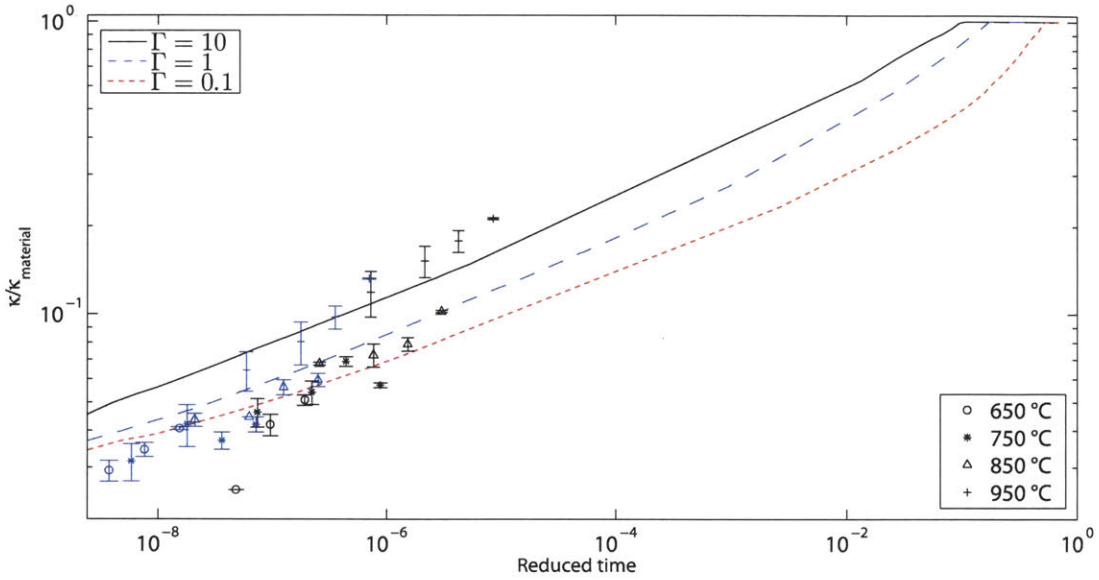

Figure 4.10: Dimensionless conductivity, $\kappa/\kappa_{\text{material}}$ (where $\kappa_{\text{material}} = \kappa_{\text{Cu}}$), as a function of reduced time (t^*). The markers show the experimental results for the coarse copper. Black markers show the results for the 38-75 μm powder and the blue markers show the results for the 75-106 μm powder

the thermal conductivity. Nevertheless, the model is helpful as a design tool for estimating the thermal conductivity of sintered wicks with reasonable accuracy.

4.6 Thermal Conductivity of Coarse Copper

The model of this chapter is not designed to predict the thermal conductivity of sintered powders without a uniform particle size. The coarse copper powder was sieved in relatively large size ranges. Nevertheless, the experimental results of these powders are compared with the generalized charts in Figure 4.10. The reduced time was calculated with the average particle size of each range. For the 38-75 μm powder, the average particle size is 57 μm; and for the 75-106 μm, the average particle diameter is 91 μm.

Despite the fact that the model is based on a unique particle size powder, Figure 4.10 shows that it can be used to determine an approximate thermal conductivity for these powders. The error found for sintering temperatures below 950 °C is below

10%. For a sintering temperature of 950 °C, the error becomes as large as 50%.

4.7 Chapter Summary

The results of the two-sphere model of Chapter 3 were used to define the geometry of a unit cell composed of two hemispheres bonded by a neck after sintering. The geometry of the unit cell was modeled in COMSOL, in order to determine the unit cell effective thermal resistance. In this manner, the effect of sintering time and temperature was taken into account in the calculation of the effective thermal conductivity of a wick. The effective thermal resistance of the unit cell was used in a random resistor network generated by a MATLAB code. The random resistor network was used to model the randomness in the position of particles and air gaps in a sintered wick. The network also accounts for the multiple connections between particles that exist in a real wick structure. The effective resistance of the random network is calculated by solving Ohm's law in matrix form. The model overestimates the thermal conductivity by 26% when compared to the experimentally measured values. The inefficient packing structure (simple cubic crystal) used to model the sintered wick and the overlapping of the unit cells in this model were found to be significant sources of error.

A generalized chart, which does not include the effect of the heating and cooling processes was built and compared with the experimental measurements. The agreement was satisfactory at low temperatures. However, as it was shown for the case of sintered 10 μm copper wicks, as the temperature increases the error also increases.

Next chapter discusses possible improvements that can be implemented in the sintering model and the thermal conductivity model.

Chapter 5

Conclusions and Future Work

5.1 Conclusions

Sintering of powdered metals is a manufacturing technique that can be used to form wick structures with controlled properties. Wick structures are a fundamental component of heat pipes because this structure drives the fluid flow inside the heat pipe. Thus, being able to predict the thermophysical properties of sintered wicks becomes extremely useful when designing systems based on heat pipes. In this thesis, shrinkage, porosity, permeability, maximum capillary pressure and thermal conductivity of sintered copper and Monel wicks were studied. Experimental measurements of these properties were presented. A model that is able to predict the thermal conductivity of sintered wicks was also developed. Although this model is specific to particles of uniform size and of a certain roughness, it is reasonably accurate and many times faster than finite element simulations.

The experimental measurements of the physical properties of the wicks show that shrinkage has to be carefully considered when sintering powders. Shrinkage causes detachment of the wick from its container. A clear relation between shrinkage and sintering time and temperature was found. The lower the sintering temperature and time, the smaller the shrinkage of the wick. However, in the sintering temperature-time range where no gap formed between the wick and the container, the wick per-

meability and capillary pressure did not show a clear variation with these fabrication factors. Thus, it is concluded that in this range, the flow properties of a randomly packed sintered wick depend exclusively on the particle size. The fabrication parameters can be dictated by the wick structural rigidity and the thermal conductivity desired. Obtaining specific properties with Monel powder is harder to achieve than with copper powder, because of the relatively small range between the minimum temperature needed to obtain structural rigidity and the maximum temperature that can be reached without significant shrinkage of the wick.

The two-sphere model was used to relate the sintering conditions to the neck geometry between particles in the wick. This model solves for the neck radius as a function of sintering temperature and time, $x(T,t)$, by first defining the chemical potential resulting from the geometry of two spheres bonded by a neck. Then, Fick's law is used to determine the amount of matter that diffuses by means of different sintering mechanisms. Finally the change in volume that occurs in the neck is determined from the amount of matter transported to this region. From the results of the two-sphere model it was concluded that the peak sintering temperature and the time at the sintering temperature dominate the neck growth rate. Thus, there exists a negligible difference between different heating rates. The heating and cooling processes are only important for very short holding times, when the time spent at the peak temperature is shorter than the time spent at temperatures close to the peak temperature while heating and/or cooling the wick.

The thermal conductivity model of Chapter 4 is based on the unit cell of the two-sphere model. By means of a simulation in COMSOL, the effective thermal resistance of the unit cell was found. As expected, the neck region dominates the thermal resistance of the wick. The effective thermal resistance of the unit cell was included in a random resistor network. The effective conductivity of this network gives the thermal conductivity of the sintered wick. Thermal conductivity of the wick was found to increase with sintering temperature and with isothermal hold time. From the results

of this model it is concluded that the change of thermal conductivity as the sintering time increases is a direct consequence of the sintering kinetics. The model is accurate for low levels of shrinkage. At high levels of shrinkage the model underpredicts the conductivity by up to 26%. Besides the many simplifications of the sintering model and the thermal conductivity, overlapping of unit cells and the inefficient packing scheme assumed for the wicks are important sources of error between the predicted and the measured thermal conductivity.

The thermal conductivity model enables the construction of a generalized thermal conductivity chart. This chart can be used to determine a practical sintering time and temperature profile to fabricate sintered wicks with the desired thermal conductivity.

5.2 Future Work

The sintering model and the thermal conductivity model described in this thesis are intended to capture the effect of the most important factors that determine the thermal conductivity of sintered wicks. It was shown that the fabrication conditions (i.e. sintering time and temperature) have a significant influence in determining the size of the necks between particles and thus, in determining the thermal conductivity of a sintered wick. However, the geometry of the wick itself has an important effect on the behavior of both the sintering model and the thermal conductivity model. Determining the geometry of the wick with great precision is a demanding task in computational terms. For this reason, many simplifications are needed in these models in order to solve them in a reasonable amount of time. Thus, possible improvements for these models are related to a more rigorous treatment of the wick geometry, which is likely to require improving the efficiency of the computational code.

Porosity is a key geometrical parameter of the thermal conductivity model. In this thesis, porosity was included in the model by fitting experimental measurements of this property. However, it was shown that the measured porosity actually depends

on the roughness of the powder used. Thus, the model results given in this thesis are valid only for powder of similar roughness to the one used for this study, but the methodology could be applied to other roughness particles. Future work would be focused on implementing a predictive model of porosity. This model would eliminate porosity as an experimental parameter and allow the conductivity model to be applied to a wider range of powders regardless of their roughness.

Shrinkage is another geometrical parameter that could be further improved. In this thesis shrinkage of the two-sphere model is determined by relating the volume of matter transported to the neck to the volume of matter encompassed in the region where the spheres overlap (see Figure 3.1). This approach effectively couples the neck growth and the shrinkage in a manner that makes it impossible to analyze sintering conditions where there is neck growth but no densification. Although it was shown in this work that it is impossible to reach this condition in copper (because surface diffusion dominates at higher sintering temperatures, where all the shrinkage has already happened), other wick materials could benefit from a low-shrinkage sintering scheme. Existing models in the sintering literature have improved the two-sphere model to effectively separate shrinkage from neck growth, while obeying mass conservation [61].

The two-sphere model is valid only for the first stage of sintering. When a powdered metal has been sintered at high temperatures for long periods of time, the structure of the wick no longer resembles that of spheres connected by necks. Instead, the necks grow until they touch each other. At this point, the sintering kinetics changes from neck growth to the elimination of pores in a solid matrix. In the sintering literature, this change in kinetics is related to changes in 'sintering stages'. The second stage of sintering is characterized by long interconnected pores of cylindrical shape. In the third stage of sintering, these pores become isolated and their shape is that of a spheroid. Surface diffusion slowly eliminates these pores. Thus, future work would focus on analyzing the structure of the sintered wicks and determine whether it is necessary to implement a model that takes into account the different

sintering stages. Because these sintering stages are strongly related to the structure of the wick, including any of these stages in the sintering/thermal conductivity model requires following the evolution of the wick geometry during sintering.

Other geometric limitations of the model that can be improved in the future have been discussed in Chapter 3 and 4 and include the overlapping of unit cells and the constraint on the porosity range associated with the simple cubic packing scheme.

The random resistor network model is many times faster than a full-field finite element simulation when calculating the thermal conductivity of a wick. However, the `MATLAB` code implemented in this thesis is inefficient when dealing with large networks. The model becomes impractical when working with structural matrices larger than a $10 \times 10 \times 10$ array. A possible solution to this problem is to implement more efficient algorithms to solve matrix equations for very large systems, such as reordering the nodes before elimination [54], or the 'KLU' algorithm [15].

In this thesis, permeability and capillary pressure were measured only for samples with lower shrinkage. These measurements were not performed in samples where the wick was not bonded to the walls of its container. The metal powder could be sintered in a graphite mold so that the wick can be easily detached after sintering. The wick can be press-fit inside a flexible-wall tube. Permeability and capillary pressure of this wick can be measured as explained in Chapter 2. In this manner, permeability and maximum capillary pressure could be measured for a larger range of sintering times and temperatures.

The thermal conductivity model described in this thesis is an efficient alternative to finite element simulations of sintered wicks. Addressing the future work suggested in this section will help to improve its accuracy.

Appendix A

SEM Measurements

In addition to the geometric measurements presented in Chapter 2, some of the necks between two particles were measured using a Japan Electron Optics Laboratory [23] Scanning Electron Microscope (SEM). This appendix explains the methodology followed to measure the radius of the neck connecting two particles. The radius measured is compared with the radius predicted by the two-sphere model.

A.1 Methodology of Measurement

First, two spheres bonded by a neck were found in the surface of a sintered wick. The measurement of the radius of the neck between two particles is accurate only when both particles are in the same plane, and this plane is parallel to the measurement plane. To ensure that these conditions were satisfied, only particles that were in focus at the same time were considered. Thus, after locating the bonded particles, the level of focus in the microscope was changed. It was checked that both of the particles move in and out of focus at the same time.

Once a suitable system of two particles bonded by a neck was found, a circle was drawn around each of the particles. The circle drawn was the one that best encompassed the particle. Because of shrinkage, the circles will overlap, as in Figure 3.1. The center of the overlapped region was found. A straight line was drawn from this

point to the neck. The length of this line is the neck's radius.

Figure A.1 shows an example of a SEM picture of two particles connected by a neck and the circles drawn that best encompassed the particles. The average diameter of these particles is 11 μm. The particles of this figure were sintered at 650 °C for 0 minutes. The two-particle model predicts a neck radius of 1.6 μm for these conditions. The radius of the measured neck is 1.9 μm.

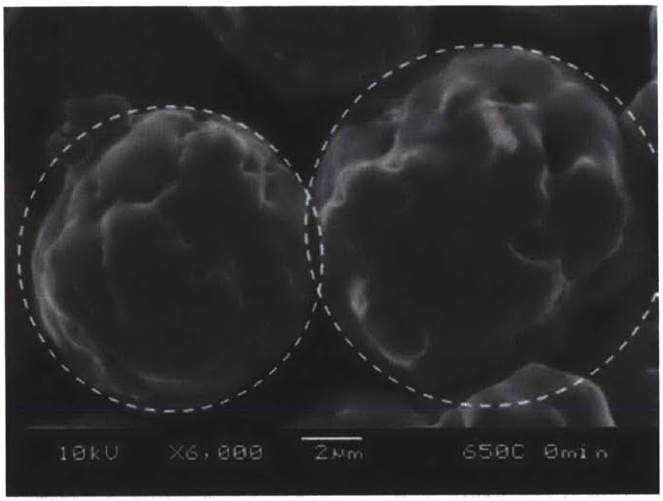

Figure A.1: SEM picture of two particles connected by a neck. The average diameter of these particles is 11 μm. The particles were sintered at 650 °C for 0 minutes.

A.2 Results

The average particle diameter of the measured spheres is 10 μm with a standard deviation of 1.4 μm. For each pair of particles, the error between the measured and the predicted value of the neck radius was calculated as

$$\text{error} = \frac{x_{\text{TSM}} - x_{\text{exp}}}{x_{\text{exp}}} \times 100\% \tag{A.1}$$

where x_{TSM} is the neck radius predicted by the two-sphere model and x_{exp} is the neck radius measured from the SEM pictures.

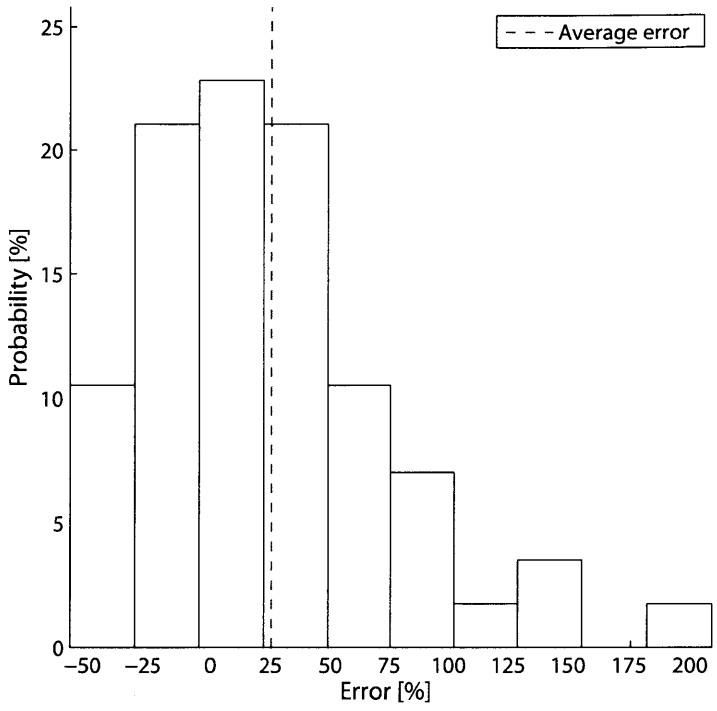

Figure A.2: Probability distribution of the error between measured and predicted values of the neck radius. The average error, approximately 25%, is marked by the dashed vertical line.

The error for all the measurements is shown as a probability density plot in Figure A.2. The probability of obtaining an error equal to the abscissa is plotted in the ordinate of this graph.

It can be seen in Figure A.2 that the two-sphere model tends to overestimate the neck radius. As shown in Figure A.2, there is more than 60% of probability of finding a difference between the calculated and experimental radii between -25% and 50%. Almost one quarter of the measured errors were between 0 and 25%.

Possible sources of error are explained in Chapter 3.

Appendix B

BCC and FCC Unit Cells

The thermal conductivity model of Chapter 4 is based on the thermal resistivity of the unit cell of Figure 4.1. This unit cell is formed by two hemispheres bonded by a neck. The geometry of the neck (its radius and radius of curvature) is dictated by the two-sphere sintering model according to the particle size and material, as well as the sintering temperature and time. Because each of the particles was assumed to be connected to its six closest neighbors in the random resistor network model, the minimum porosity that can be attained with this unit cell is around 47%, which is the simple cubic (SC) crystal porosity. Lower porosities are impossible to match with this packing scheme. In this appendix two additional unit cells are described.

B.1 Unit Cell Thermal Resistance

Besides the SC, additional unit cells with lower porosities were investigated. These unit cells were based on spheres packed as in body-centered cubic (BCC) and face-centered cubic (BCC) crystals. Figures B.1**a** and B.2**a** show the BCC-based and the FCC-based unit cells, respectively. These unit cells were chosen such that the nodes of the random network lie in the center of the BCC and FCC crystals. Figure B.1**b** shows two of the BCC-based unit cells together. The dashed line in this figure encloses a BCC crystal, which is shown by itself in Figure B.1**c**. Figures B.2**b** and B.2**c** show two FCC-based unit cells together and the FCC structure by itself, respectively.

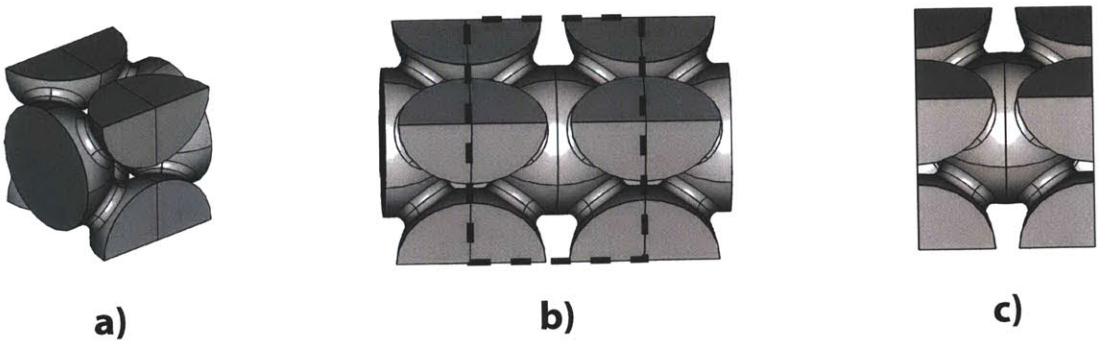

Figure B.1: **a)** The BCC-based unit cell. **b)** Two unit cells together. The dashed line square encloses a BCC crystal. The selection of this unit cell allows the node of the resistor network to be located in the center of the BCC crystal. **c)** The BCC structure encompassed in the dashed line of **b**. For this figure, $x/a = 0.4$.

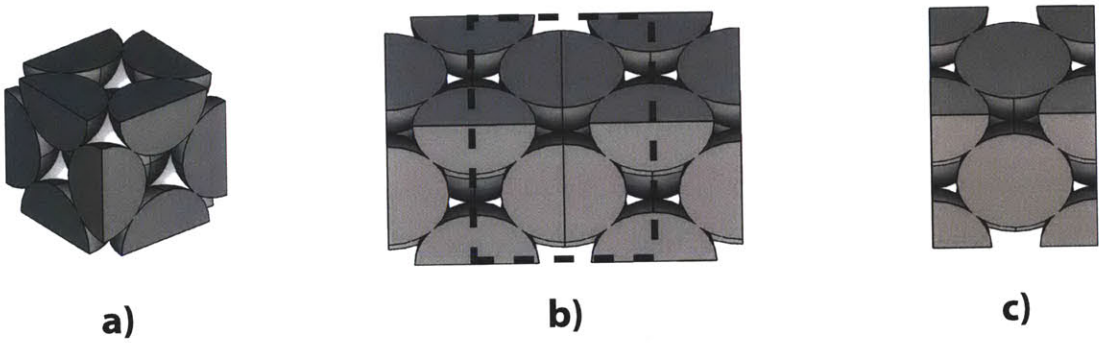

Figure B.2: **a)** The FCC-based unit cell. **b)** Two unit cells together. The dashed line square encloses an FCC crystal. The selection of this unit cells allows the node of the resistor network to be located in the center of the FCC crystal. **c)** The FCC structure encompassed in the dashed line of **b**. For this figure, $x/a = 0.05$.

As in the case of the SC unit cell, each of these unit cells was modeled in COMSOL. All the boundaries of the unit cells, except for two surfaces, were assumed to be adiabatic. A 10 K difference in temperatures was specified at the non-adiabatic surfaces of each cell. The total normal outward heat flux across one of these surfaces, $\dot{Q}$, was calculated from the simulation and used to obtain the unit cell thermal resistance according to Equation 4.1. The normalized thermal resistance for a BCC-based and an FCC-based unit cell is shown in Figure B.3. The ordinate of this figure is normalized to the thermal resistance of a solid cube of copper, the size of which is the same as

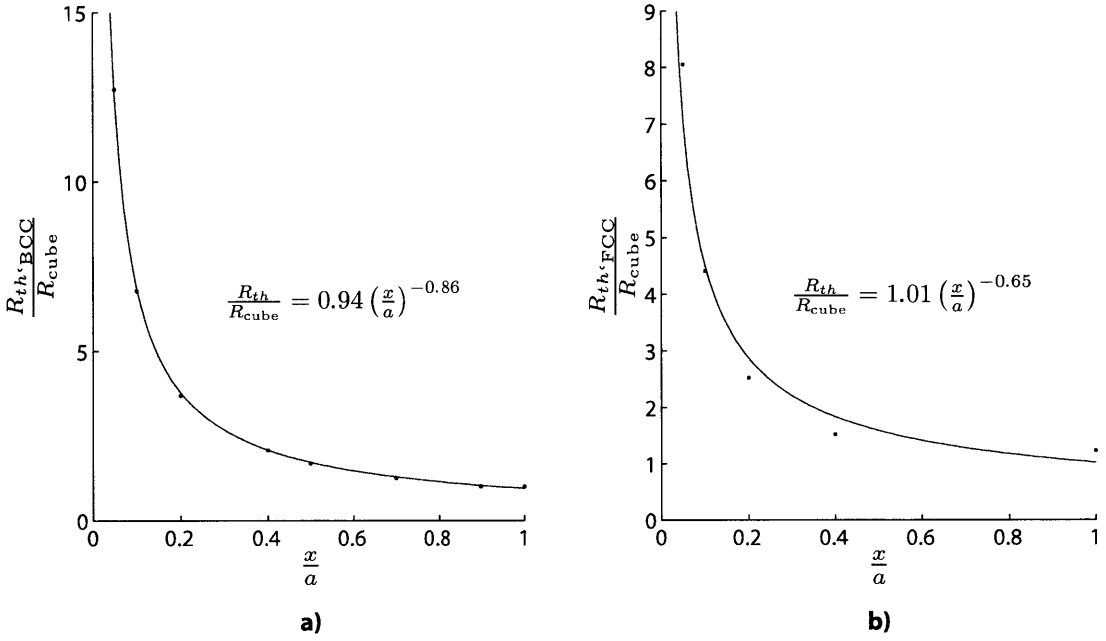

Figure B.3: Normalized thermal resistance of the **a)** BCC-based; and, **b)** FCC-based unit cells as a function of neck size. Simulation results are marked with dots. The blue lines show the best least-squares fit for the simulation results. The least-squares fit equations express the normalized thermal resistance, $\frac{R_{th}}{R_{\text{cube}}}$, in terms of the normalized neck radius, x/a.

the unit cell's size. This normalized thermal resistance is plotted as function of the neck size between the particles, x/a. The geometry of the neck between two spheres was obtained from the two-sphere sintering model. However, in this plot the effect of shrinkage was not taken into consideration.

Comparison of Figure B.3 with Figure 4.2 reveals that the effective thermal resistance of the two-sphere unit cell is larger than the resistance of the BCC and FCC-based unit cells. This reduction in the resistance is due to the multiple connections between particles that are present in both the BCC and FCC unit cells.

B.2 Comparison between The Resistor Network Model and COMSOL

As explained in Chapter 4, there exists an overlap of the unit cells in the nodes. Figure B.4**a** shows a simple geometry constructed with three BCC-based unit cells, 'A', 'B' and 'C', where the overlap between them can be seen. Figure B.4**b** shows the overlap for the FCC-based unit cell. As more unit cells are connected to a single node, more overlap will exist in that node, the worst case being that of six connections to a single node. A similar overlap was shown for the two-sphere unit cell, which accounted for an error of approximately 1.5%. However, in the BCC and FCC-based unit cells the overlap occurs not only in the spheres, but also in the necks between them. Thus, the resistance associated with some necks, is counted multiple times. Because the necks are the regions that dominate the thermal resistance of the unit cell, the overlap in the BCC and FCC unit cells has a larger impact on the effective wick resistance than the overlap in the two-sphere unit cell.

The fact that the nodes are located at the center of the unit cells, forces the heat flux to travel to the node in the center of a particle before being able to move to the rest of the nodes. In reality, the heat flux lines are free to bend before reaching the center of the unit cells. For this reason, the model is expected to overestimate the thermal resistance when the heat flux travels between nodes that are not directly connected by a unique unit cell.

To test the effect of the overlap of unit cells, as well as the effect of the position of the nodes, the geometry of Figures B.4**a** and B.4**b** were constructed. For these geometries, the effective thermal conductivity was calculated using the random resistor network and a COMSOL simulation. The temperature difference between two of the nodes of Figure B.4**a** and B.4**b** was set to 10 °C. The rest of the surfaces were set to be adiabatic. The total normal heat flux trough one of the non-adiabatic bases was calculated and used to compute the equivalent thermal resistance using Equation

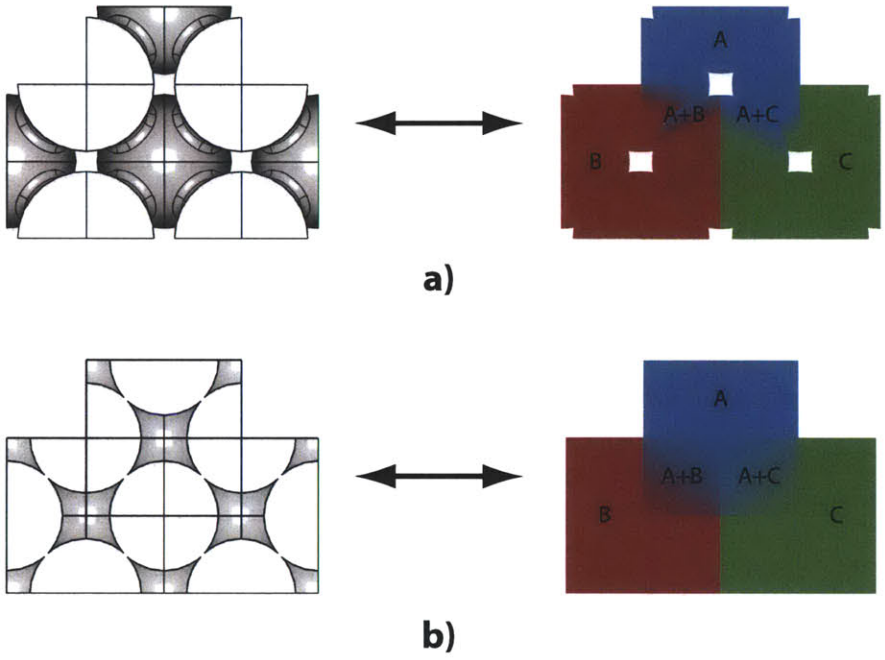

Figure B.4: A central node connected by unit cells to three other nodes. There are three unit cells, labeled 'A', 'B' and 'C' and differentiated by color. Unit cells 'A' and 'B', and 'A' and 'C' overlap in the regions shown for the **a)** BCC-based; and, **b)** FCC-based unit cell.

4.1. Two cases were considered. In one case, the temperature difference was set in bases opposed to each other. The effective thermal resistance calculated in this case is designed $R_{th,\text{across}}$. In the second case, the bases considered were perpendicular to each other and the resistance calculated is called $R_{th,\text{bent}}$.

For the BCC-based unit cell, $R_{th,\text{across}}$ calculated from the network model is 10.8% larger than the COMSOL result. For this unit cell, $R_{th,\text{bent}}$ from the resistor network is 38.3% larger than the simulation result. For the FCC-based unit cell, $R_{th,\text{across}}$ is 10.7% larger than the COMSOL result, while $R_{th,\text{bent}}$ from the resistor network is 38.0% larger than the simulation result. Thus, both the BCC and the FCC-based resistor networks overpredict the effective thermal resistance. However, the difference between the simulation and the resistor model is 4 to 7 times larger than in the two-sphere unit cell case.

The effective thermal conductivity of the 10 μm copper wick was calculated using the unit cells of this appendix. The general shape of the curves is similar to the one obtained with the two-sphere unit cell. Nevertheless, the predicted thermal conductivity is considerably below the experimentally measured one. Thus, the BCC and the FCC-based unit cells do not improve the accuracy of the thermal conductivity model.

Appendix C

MATLAB Code

C.1 Thermal Conductivity Model

This MATLAB code calculates the thermal conductivity of sintered wicks.
Version: 8.50
Francisco Alonso Dominguez Espinosa

Initialization

```
clear all; close all; clc
disp('3D random matrix model with h/a');
disp('SD and GBD coupled');
disp(' ');
```

Model parameters

```
k_mat=400; % Thermal conductivity of the sintered wick [W/m-K]
a=5e-6; % Particle radius [m]
T0=(25+273.15); % Initial sintering temperature [K]
r=1/6; % Heating ramp rate [K/s]
% Sintering temperatures. From 'Ti' to 'Tf' in 'step' steps [K]
Ti=(450+273.15);
step=100;
Tf=(950+273.15);
time=60*[0, 15, 45, 90, 180]; % Sintering time [s]
rndsiz=4; % Size of the structural matrix (rndsiz x rndsiz x rndsiz)
repite=8; % Number of random matrices generated to get an average conductivity
```

Neck size and shrinkage

```
z=1; % Index variable
% Initialization of array variables
si=(Tf-Ti)/step+1; % Size of array variables that depend on temperature
sit=numel(time); % Size of array variables that depend on time
x0=zeros(1,si); % Initial neck size [m]
x0u=ones(1,si); % Neck size after heating process [m]
x0i=ones(si,sit); % Neck size after isothermal sintering [m]
x0d=ones(si,sit); % Neck size after cooling process [m]
h=ones(si,sit); % Shrinkage parameter after sintering processes [m]
Ru=ones(si,sit); % Resistance of the unit cell [K/W]

pbar=waitbar(0,'Initializing sintering model...','Name','Sintering model','CreateCancelBtn',...
    'setappdata(gcbf,''canceling'',1)'); % Creation of progress bar

for T=Ti:step:Tf
    waitbar((z-1)/6,pbar,['Temperature: ',num2str(T-273.15),' C']); % Updating the progress bar
    x0u(z)=rampup(a,x0(z),T0,T,r); % Neck size after heating process [m]
    for v=1:1:sit
        if getappdata(pbar,'canceling') % 'Cancel' option for progress bar
            break;
        end
        x0i(z,v)=zhang(a,x0u(z),time(v),T); % Neck size after isothermal sintering [m]
        x0d(z,v)=rampdown(a,x0i(z,v),T0,T); % Neck size after cooling process [m]
        h(z,v)=xaha(a,x0d(z,v)); % Shrinkage parameter after sintering processes [m]
```

```
        Ru(z,v)=sphereh(a,x0d(z,v),h(z,v),k_mat); % Resistance of the unit cell [K/W]
        avan=(z-1)/si+v/(si*sit); % Wait bar progress
        waitbar(avan,pbar); % Updating the progress bar
    end
    z=z+1;
end
delete(pbar); % Closing the progress bar window
```

Random matrix and thermal resistance calculation

```
z=1; % Index variable
% Initialization of array variables
[m,n]=size(Ru);
k_R=zeros(m,n); % Effective thermal conductivity of sintered wick

pbar=waitbar(0,'Initializing random matrix model...','Name','Random resistor model','CreateCancelBtn',...
    'setappdata(gcbf,''canceling'',1)');  % Creation of progress bar

for T=Ti:step:Tf
    waitbar((z-1)/si,pbar,['Temperature: ',num2str(T-273.15),' C']); % Updating the progress bar
    for rpe=1:1:repite
        if getappdata(pbar,'canceling') % 'Cancel' option for progress bar
            break;
        end
        p=(-2.911*h(z,1)*100/a+58.67)/100; % Initial porosity of sintered wick
        [nodes,h0]=ran3h(rndsiz,p,h(z,1),a); % Assembly of a random structural matrix
        for w=1:1:n
            k_R(z,w)=k_R(z,w)+matr32h(a,Ru(z,w),nodes,h(z,w))/repite; % Average thermal conductivity [W/mK]
        end
        prog=(z-1)/si+(rpe/(repite*si)); % Wait bar progress
        waitbar(prog,pbar); % Updating the progress bar
    end
    z=z+1;
end
delete(pbar); % Closing the progress bar window
```

Plots

```
figure('Name','Thermal conductivity')
b=1; % Index variable
for w=1:1:si
    plot(time/60,k_R(w,:),'k'); % Plot of predicted values
    b=b+2;
    if w==1
        hold on
    end
end
xlabel('Isothermal sintering time [min]','FontSize',16);
ylabel('Thermal conductivity [W/mK]','FontSize',16);
hold off
```

C.2 Heating Process

```
function [x,h]=rampup(d,n,in,fi,ram)
```

Function rampup calculates the sinter neck radius and the shrinkage factor after the heating process.
Francisco Alonso Dominguez Espinosa

```
d is the radius of the particle [m]
n is the initial neck size [m]
in is the initial heating temperature [K]
fi is the final heating temperature [K]
ram is the heating ramp rate [K/s]
```

Get variables

```
a=d; % Radius of the particle [m]
ini=n; % Initial neck size [m]
T0=in; % Initial heating temperature [K]
T=fi; % Final heating temperature [K]
r=ram; % Heating ramp rate [K/s]
```

Calculation

Initialization of variables

```
x0b=0; % Neck size at the end of the heating process [m]
for temp=T0:0.1:T
    x0b=zhang(a,ini,(0.1/r),temp); % Call the results from Zhang's model [m]
    ini=x0b; % Set the new value of the neck size [m]
end
```

Returned variables

```
x=x0b; % Neck size at the end of the heating process [m]
h=xaha(a,x); % Shrinkage factor at the end of the heating process [m]
end
```

C.3 Isothermal Sintering Process

```
function [xf]=zhang(d,ini,n,temp)
```

Function zhang returns the neck size radius at a time 'ti' of sintering. Francisco Alonso Dominguez Espinosa

```
d is the radius of the particle [m]
ini is the initial neck size [m]
n is the sintering time [s]
temp is the sintering temperature [K]
```

Get variables

```
a=d; % Radius of the particle [m]
x0=ini; % Initial neck size [m]
ti=n; % Sintering time [s]
T=temp; % Sintering temperature [K]
```

Data

```
Ds=ssd(T); % Surface diffusion coefficient [m^2/s]
k=1.3806504e-23; % Boltzmann's constant [J/K]
gamma=1.72; % Copper surface energy [J/m^2]
delta=2.56e-10; % Copper interatomic distance [m]
omega=1.18e-29; % Copper atomic volume [m^3]
Gamma=Gammar(T); % Round Gamma to Zhang's plotted results
```

Data and interpolation

```
if Gamma==0
    t=[0; 9.9500E-10; 1.3800E-09; 1.9800E-09; 2.8300E-09; 3.9400E-09; 5.6400E-09; 8.0600E-09; 1.1200E-08; 1.6000E-08;...
        2.2300E-08; 3.1900E-08; 4.4400E-08; 6.3500E-08; 8.8300E-08; 1.2600E-07; 1.7600E-07; 2.5100E-07; 3.5900E-07;...
        5.0000E-07; 7.1500E-07; 9.9500E-07; 1.4200E-06; 1.9800E-06; 2.8300E-06; 3.9400E-06; 5.4800E-06; 7.8400E-06;...
        1.1200E-05; 1.5600E-05; 2.2300E-05; 3.1900E-05; 4.4400E-05; 6.3500E-05; 9.0800E-05; 1.3000E-04; 1.8100E-04;...
        2.5900E-04; 3.6000E-04; 5.1500E-04; 7.1600E-04; 1.0200E-03; 1.4300E-03; 1.9800E-03; 2.8400E-03; 4.0600E-03;...
        5.6500E-03; 8.0800E-03; 1.1600E-02; 1.6100E-02; 2.3000E-02; 3.2000E-02; 4.5800E-02; 6.3800E-02; 9.1300E-02;...
        1.2700E-01; 1.7700E-01; 2.5300E-01; 3.6200E-01; 5.05E-01];
    x=[0; 9.9950E-02; 1.0563E-01; 1.1108E-01; 1.1740E-01; 1.2408E-01; 1.3048E-01; 1.3722E-01; 1.4502E-01; 1.5327E-01;...
        1.6199E-01; 1.7120E-01; 1.8094E-01; 1.9124E-01; 2.0110E-01; 2.1254E-01; 2.2463E-01; 2.3741E-01; 2.4966E-01;...
        2.6386E-01; 2.7748E-01; 2.9179E-01; 3.0685E-01; 3.2430E-01; 3.4104E-01; 3.5863E-01; 3.7714E-01; 3.9660E-01;...
        4.1706E-01; 4.3639E-01; 4.5891E-01; 4.8017E-01; 5.0494E-01; 5.2834E-01; 5.5283E-01; 5.7845E-01; 6.0525E-01;...
        6.3329E-01; 6.5932E-01; 6.8642E-01; 7.1463E-01; 7.4400E-01; 7.7458E-01; 8.0237E-01; 8.3118E-01; 8.5671E-01;...
        8.8301E-01; 9.1013E-01; 9.3808E-01; 9.6688E-01; 9.8663E-01; 1.0118E+00; 1.0273E+00; 1.0483E+00; 1.0805E+00;...
        1.0861E+00; 1.0863E+00; 1.0919E+00; 1.0921E+00; 1.09222];
else if Gamma==0.1
        t=[0; 1.0300E-09; 1.4300E-09; 2.0600E-09; 2.9500E-09; 4.1200E-09; 5.9200E-09; 8.2600E-09; 1.1800E-08; 1.6500E-08;...
            2.3100E-08; 3.3100E-08; 4.7500E-08; 6.6300E-08; 9.5100E-08; 1.3300E-07; 1.8500E-07; 2.6600E-07; 3.8100E-07;...
            5.3200E-07; 7.4300E-07; 1.1000E-06; 1.4900E-06; 2.1300E-06; 2.9800E-06; 4.1600E-06; 5.8000E-06; 8.3300E-06;...
            1.1600E-05; 1.6200E-05; 2.3300E-05; 3.3400E-05; 4.6600E-05; 6.5000E-05; 9.3300E-05; 1.3000E-04; 1.8200E-04;...
            2.6100E-04; 3.6400E-04; 5.2200E-04; 7.2900E-04; 1.0500E-03; 1.4600E-03; 2.0400E-03; 2.8400E-03; 4.0800E-03;...
            5.6900E-03; 8.1600E-03; 1.1400E-02; 1.5900E-02; 2.3500E-02; 3.2700E-02; 4.5700E-02; 6.5600E-02; 9.4100E-02;...
            1.3100E-01; 1.8800E-01; 2.6300E-01; 3.6700E-01; 5.26E-01];
        x=[0; 7.5510E-02; 7.7830E-02; 8.0220E-02; 8.3950E-02; 8.7410E-02; 8.9200E-02; 9.2410E-02; 9.6700E-02; 1.0069E-01;...
            1.0484E-01; 1.0916E-01; 1.1423E-01; 1.1954E-01; 1.2447E-01; 1.3092E-01; 1.3700E-01; 1.4410E-01; 1.5156E-01;...
            1.5861E-01; 1.6682E-01; 1.7635E-01; 1.8548E-01; 1.9509E-01; 2.0415E-01; 2.1473E-01; 2.2699E-01; 2.3874E-01;...
            2.5111E-01; 2.6411E-01; 2.7779E-01; 2.9218E-01; 3.0731E-01; 3.2322E-01; 3.3996E-01; 3.5756E-01; 3.7608E-01;...
            3.9556E-01; 4.1394E-01; 4.3538E-01; 4.5793E-01; 4.8164E-01; 5.0403E-01; 5.3014E-01; 5.5199E-01; 5.8057E-01;...
            6.0756E-01; 6.3903E-01; 6.6537E-01; 6.9982E-01; 7.3236E-01; 7.6254E-01; 7.9799E-01; 8.3088E-01; 8.6951E-01;...
            9.1454E-01; 9.6190E-01; 1.0117E+00; 1.0534E+00; 1.08035];
    else if Gamma==1
            t=[0; 1.0300E-09; 1.4400E-09; 2.0700E-09; 2.9800E-09; 4.1700E-09; 5.8300E-09; 8.1500E-09; 1.1700E-08; 1.6900E-08;...
                2.3600E-08; 3.3000E-08; 4.6200E-08; 6.6500E-08; 9.3000E-08; 1.3400E-07; 1.8700E-07; 2.6200E-07; 3.7700E-07;...
                5.1300E-07; 7.3800E-07; 1.0300E-06; 1.4400E-06; 2.0800E-06; 2.9100E-06; 4.0700E-06; 5.6900E-06; 7.9600E-06;...
                1.1500E-05; 1.6000E-05; 2.2400E-05; 3.1400E-05; 4.5100E-05; 6.3100E-05; 9.0800E-05; 1.2700E-04; 1.7800E-04;...
                2.5600E-04; 3.5800E-04; 5.1500E-04; 7.2000E-04; 1.0100E-03; 1.4100E-03; 1.9700E-03; 2.8400E-03; 3.9700E-03;...
                5.7200E-03; 8.0000E-03; 1.1500E-02; 1.6100E-02; 2.2500E-02; 3.2400E-02; 4.5400E-02; 6.3500E-02; 9.1300E-02;...
                1.2800E-01; 1.7900E-01; 2.5700E-01; 3.5000E-01; 4.9000E-01; 7.06E-01];
            x=[0; 7.91600E-02; 8.16400E-02; 8.50600E-02; 8.90900E-02; 9.28200E-02; 9.72100E-02; 1.01290E-01; 1.06080E-01;...
                1.11660E-01; 1.16940E-01; 1.23740E-01; 1.30250E-01; 1.37110E-01; 1.45080E-01; 1.52720E-01; 1.61590E-01;...
                1.70970E-01; 1.80900E-01; 1.91400E-01; 2.02520E-01; 2.14280E-01; 2.26730E-01; 2.39890E-01; 2.53820E-01;...
                2.68570E-01; 2.82710E-01; 2.97600E-01; 3.14880E-01; 3.33170E-01; 3.50720E-01; 3.71080E-01; 3.90630E-01;...
                4.11200E-01; 4.32860E-01; 4.55650E-01; 4.79650E-01; 5.04920E-01; 5.31510E-01; 5.59500E-01; 5.85960E-01;...
                6.16820E-01; 6.45980E-01; 6.76530E-01; 7.04900E-01; 7.38230E-01; 7.69190E-01; 8.05560E-01; 8.35050E-01;...
                8.70060E-01; 9.01910E-01; 9.34930E-01; 9.64190E-01; 9.94380E-01; 1.02551E+00; 1.05221E+00; 1.07408E+00;...
                1.09642E+00; 1.09649E+00; 1.09658E+00; 1.09666];
        else if Gamma==10
                t=[0; 1.0000E-09; 1.4300E-09; 2.0500E-09; 2.9300E-09; 4.0800E-09; 5.8300E-09; 8.1200E-09; 1.1600E-08;...
```

```
                    1.6200E-08; 2.2500E-08; 3.2200E-08; 4.4800E-08; 6.4100E-08; 9.1700E-08; 1.3100E-07; 1.8300E-07;...
                    2.5400E-07; 3.6400E-07; 5.2000E-07; 7.4500E-07; 1.0400E-06; 1.4400E-06; 2.0600E-06; 2.8700E-06;...
                    4.1100E-06; 5.7200E-06; 8.1800E-06; 1.1700E-05; 1.6300E-05; 2.2700E-05; 3.2400E-05;4.6400E-05;...
                    6.6400E-05; 9.2400E-05; 1.2900E-04; 1.8400E-04; 2.5600E-04; 3.6600E-04; 5.1000E-04; 7.3000E-04;...
                    1.0200E-03; 1.4100E-03; 2.0200E-03; 2.8200E-03; 4.0300E-03; 5.6100E-03; 8.0200E-03; 1.1200E-02;...
                    1.6000E-02; 2.2200E-02; 3.1800E-02; 4.5500E-02; 6.3300E-02; 8.8100E-02; 1.2600E-01; 1.8000E-01;...
                    2.5100E-01; 3.4900E-01; 4.8600E-01; 6.9600E-01; 9.9600E-01; 1.3900E+00; 1.98E+00];
                x=[0; 7.5120E-02; 7.7430E-02; 7.9410E-02; 8.2690E-02; 8.5660E-02; 8.8750E-02; 9.1940E-02; 9.5250E-02;...
                    9.8680E-02; 1.0275E-01; 1.0752E-01; 1.1196E-01; 1.1657E-01; 1.2199E-01; 1.2766E-01; 1.3427E-01;...
                    1.3981E-01; 1.4631E-01; 1.5389E-01; 1.6104E-01; 1.6938E-01; 1.7815E-01; 1.8737E-01; 1.9608E-01;...
                    2.0624E-01; 2.1692E-01; 2.2815E-01; 2.3875E-01; 2.4985E-01; 2.6279E-01; 2.7501E-01; 2.8925E-01;...
                    3.0270E-01; 3.1837E-01; 3.3317E-01; 3.4866E-01; 3.6671E-01; 3.8376E-01; 4.0160E-01; 4.2027E-01;...
                    4.3981E-01; 4.6025E-01; 4.8165E-01; 5.0404E-01; 5.2748E-01; 5.5200E-01; 5.7476E-01; 6.0148E-01;...
                    6.2944E-01; 6.5870E-01; 6.8933E-01; 7.1775E-01; 7.5111E-01; 7.9000E-01; 8.2673E-01; 8.8279E-01;...
                    9.4741E-01; 1.0168E+00; 1.0694E+00; 1.0968E+00; 1.0969E+00; 1.0970E+00; 1.09703];
            end
        end
    end
end
% Dimensionless time calculation
B=Ds*delta*gamma*omega/(k*T);
tau=B*ti/a^4; % Reduced time
tau_ini=interp1(x,t,x0/a); % Value of the reduced time for the initial neck size
xi=interp1(t,x,tau+tau_ini); % Value of the dimensionless neck radius
```

Returned variables

```
xf=xi*a; % Value of the neck radius after isothermal sintering [m]
end
```

C.4 Cooling Process

```
function [x,h]=rampdown(d,n,in,fi)
```

Function rampdown returns the sinter's neck radius and the shrinkage parameter after the cooling process.
Francisco Alonso Dominguez Espinosa

```
d is the radius of the particle [m]
n is the initial neck size [m]
in is the initial cooling temperature [K]
fi is the final cooling temperature [K]
```

Get variables

```
a=d; % Radius of the particle [m]
ini=n; % Initial neck size [m]
T0=in; % Initial cooling temperature [K]
T=fi; % Final cooling temperature [K]
```

Calculation

Initialization of variables

```
x0b=0; % Neck size at the end of the heating process [m]
for temp=T0:0.1:T
    tzhang=2.28e5*exp(-5.811e-3*temp)-2.28e5*exp(-5.811e-3*(temp+0.1)); % Cooling time [s]
    x0b=zhang(a,ini,tzhang,temp); % Call the results from Zhang's model [m]
    ini=x0b; % Set the new value of the neck size [m]
end
```

Returned variables

```
x=x0b; % Neck size at the end of the heating process [m]
h=xaha(a,x); % Shrinkage factor at the end of the heating process [m]
end
```

C.5 Relationship between Neck Radius and Shrinkage Factor

```
function [h]=xaha(d,n)
```

Function xaha fits the data for the conservation of volume in the two-sphere model relating the neck size and the center approach. It returns 'h'.
Francisco Alonso Dominguez Espinosa

```
d is the radius of the particle [m]
n is the neck size at which the curvature and the center approach has to be evaluated [m]
```

Get variables

```
a=d; % Radius of the particle [m]
x=n; % Neck size at which the curvature and the center approach has to be evaluated [m]
```

Data and interpolation

```
xa=[0; 5.00E-02; 1.00E-01; 1.50E-01; 2.00E-01; 2.50E-01; 3.00E-01; 3.50E-01; 4.00E-01; 4.50E-01; 5.00E-01; 5.50E-01; 6.00E-01;...
    6.50E-01; 7.00E-01; 7.50E-01; 8.00E-01; 1];

ha=[0; 6.23E-04; 2.53E-03; 5.73E-03; 1.03E-02; 1.62E-02; 2.35E-02; 3.23E-02; 4.26E-02; 5.45E-02; 6.81E-02; 8.35E-02; 1.01E-01;...
    1.20E-01; 1.42E-01; 1.66E-01; 1.92E-01; 1/3];

p2=polyfit(xa,ha,6); % 6th-degree polynomial fit for 'h/a'
hprev=polyval(p2,x/a)*a; % The value of 'h' [m]
```

Returned variables

```
if hprev<0
    h=0; % Shrinkage factor [m]
else
    h=hprev; % Shrinkage factor [m]
end
end
```

C.6 Thermal Resistance of the Unit Cell

```
function [R_u]=sphereh(d,n,e,k1)
```

Function **sphereh** calculates the thermal resistance of a unit cell composed of two hemispheres connected by a neck. It includes the effect of h.
Francisco Alonso Dominguez Espinosa

```
d is the radius of the spheres [m]
n is the radius if the neck [m]
e is half the centers approach [m]
k1 is the thermal conductivity of the solid phase [W/mK]
```

Get variables

```
a=d; % Radius of the spheres [m]
x=n; % Radius if the neck [m]
h=e; % Shrinkage factor [m]
k=k1; % Thermal conductivity of the solid phase [W/mK]

% Fit for COMSOL results
R_cyl=(2*(a-h))/(k*pi*a^2); % Thermal resistance of the normalization cylinder [K/W]
R_u_l=1.0293/((x/a)^(0.932))*R_cyl; % Thermal resistance of the unit cell [K/W]
if R_u_l==Inf % Neck radius is zero
    R_u_l=3.9e6;  % Thermal resistance of the unit cell [K/W]
end
```

Returned variables

```
R_u=R_u_l;
end
```

C.7 Generation of the Random Structural Matrix

```
function [onodes2,h0f]=ran3h(siz,phi,app,d)
```

Function **ran3h** assembles a random matrix which represents the connections in a sintered wick. Each entry is either a zero or a one, randomly assigned. The number of zeros matches the observed porosity. It includes the effect of 'h'.
Francisco Alonso Dominguez Espinosa

```
siz is the size of the matrix (siz x siz x siz)
phi is the experimental porosity
app is the initial center approach [m]
d is the radius of the particle [m]
```

Get variables

```
s=siz; % Size of the matrix (s x s x s)
epsilon=phi; % Expected porosity
h=app; % This is the initial center approach, which is used to fix the initial porosity
a=d; % Radius of the particle [m]
```

Calculation

```
V=4/3*pi*a^3; % Volume of the unit cell [m^3]
dif=1; % Difference between epsilon and porosity
N=((2*(s*(a-h)+h))^3*(1-epsilon))/(V); % Number of ones needed
p=N/(s^3); % Binomial distribution's probability of success
% Validate probability
if p<0
    disp('ERROR (8001050F): Binomial distribution probability is smaller than 0!');
    disp(' ');
    p=0;
else if p>1
        disp('ERROR (8001050F): Binomial distribution probability is larger than 1!');
        disp(' ');
        p=1;
    end
end
% Auxiliary variables
pini=p; % Probability of Success
oce=0; % Get the warning messages only once time
oce2=0; % Get the warning messages only once time
oce3=0; % Get the warning messages only once time
difc=0.005; % Threshold in the difference between experimental and model initial porosity
t=0; % This will stop the while loop in case it is not possible to reach the target porosity
up=0; % This will stop the while loop in case it is not possible to reach the target porosity
down=0; % This will stop the while loop in case it is not possible to reach the target porosity
while (dif>difc || dif<(-difc))
    onodes=binornd(1,p,[s,s,s]); % Generate a random matrix
    % Porosity of 'onodes'
    cc=0; % Number of ones in corners
    for l=1:(s-1):s
        for k=1:(s-1):s
            for j=1:(s-1):s
                cc=cc+onodes(l,k,j);
            end
        end
    end
    ee=0; % Number of ones in edges
    % j varies
    for l=1:(s-1):s
        for k=1:(s-1):s
            for j=2:1:(s-1)
                ee=ee+onodes(l,k,j);
            end
        end
    end
    % l varies
    for k=1:(s-1):s
        for j=1:(s-1):s
            for l=2:1:(s-1)
                ee=ee+onodes(l,k,j);
            end
        end
    end
    % k varies
    for j=1:(s-1):s
        for l=1:(s-1):s
            for k=2:1:(s-1)
                ee=ee+onodes(l,k,j);
            end
        end
    end
    ff=0; % Number of ones in faces
    % j is constant
    for j=1:(s-1):s
        for k=2:1:(s-1)
            for l=2:1:(s-1)
                ff=ff+onodes(l,k,j);
            end
        end
    end
    % l is constant
    for l=1:(s-1):s
        for j=2:1:(s-1)
            for k=2:1:(s-1)
                ff=ff+onodes(l,k,j);
            end
        end
    end
    % k is constant
    for k=1:(s-1):s
        for l=2:1:(s-1)
            for j=2:1:(s-1)
                ff=ff+onodes(l,k,j);
            end
        end
    end
    tis=cc+ee+ff; % Total number of incomplete spheres
    vcs=(nnz(onodes)-tis)*V; % Volume of complete spheres
    vccs=cc*V/8; % Volume of 1/8-spheres
    vees=ee*V/4; % Volume of 1/4-spheres
    vffs=ff*V/2; % Volume of 1/2-spheres
```

```
    tvc=vcs+vccs+vees+vffs; % Total column of copper
    porosity=1-(tvc)/((2*(s-1)*(a-h))^3); % Porosity of 'onodes'
    dif=porosity-epsilon; % Difference between epsilon and porosity
    t=t+1;
    if t>=1000 && t<=1002 % Matrix generation failed
        if oce==0
            disp('Could not reach desired porosity. Changing success probability');
            disp(' ');
            oce=1;
        end
        if dif<0 % Epsilon is larger than porosity
            down=down+1;
            p=p-0.05;
            t=0;
        else % Epsilon is smaller than porosity
            up=up+1;
            p=p+0.05;
            t=0;
        end
        if p<0 || p>1
            t=1003;
            p=pini;
        end
        if up>=150 && down>=150
            if oce3==0
                disp('WARNING: Matrix may be too small to reach target porosity. Changing size');
                disp(' ');
                oce3=1;
            end
            s=s+1;
            t=0;
            p=pini;
        end
    end
    if t>=2000 % Matrix generation failed
        if oce2==0
            disp('WARNING: Could not reach target porosity. For now, changing h/a factor');
            disp(' ');
            oce2=1;
        end
        if dif<0 % h has to be smaller to reach target porosity
            h=0.95*h;
            t=899;
            p=pini;
        else % h has to be larger to reach target porosity
            h=1.05*h;
            t=899;
            p=pini;
        end
    end
end
% Display the final porosity and the structural matrix
str=['Porosity: ',num2str(porosity*100),'%'];
disp(str);
disp(' ');
% figure(); % Uncomment this line to see each one of the generated matrices generated.
for w=1:1:s
    subplot(1,s,w);
    spy(onodes(:,:,w));
end
```

Returned variables

```
onodes2=onodes; % Structural matrix
h0f=h; % Fix 'h' and 'x', if necessary
end
```

C.8 Effective Thermal Conductivity

```
function [R_m]=matr32h(d,R,rm,ini)
```

Function matr32h calculates the thermal resistivity of a structural matrix. It includes the effect of 'h'.
Francisco Alonso Dominguez Espinosa

```
d is the radius of the particle [m]
R is the resistance of a unit cell [K/W]
rm is the structural matrix
ini is the center approach [m]
```

Get variables

```
R_u=1/R; % Resistance of a unit cell [K/W]
nodes=rm; % Structural matrix
r=d; % Particle radius [m]
h=ini; % Shrinkage parameter [m]
```

Other variables

```
[f,y,upp]=size(nodes); s=f; % Size of nodes
% Thermal conductance for air gaps
R_a=1/3.9e6; % Two adjacent air gaps [K/W]
R_ua=1/1.95e6; % Half sphere and air gap [K/W]
```

Assembly of the Laplacian matrix

Initialization of array variables

```
L=zeros(numel(nodes),numel(nodes));
% Off-diagonal elements of Laplacian matrix
for a=1:1:numel(nodes)
    for b=1:1:numel(nodes)
        if a~=b
            [o,p,q]=ind2sub([s,s,s],a);
            [u,w,z]=ind2sub([s,s,s],b);
            if (o+1==u || o-1==u) && (p==w && q==z) % In the same plane and adjacent in the vertical direction
                if nodes(o,p,q)==1 && nodes(u,w,z)==1 % Two connected spheres
                    if (p==1 || p==s) && (q==1 || q==s) % Quarters along a face
                        L(a,b)=-1/4*R_u;
                    else if (p==1 || p==s) || (q==1 || q==s) % Halves along a face
                            L(a,b)=-1/2*R_u;
                        else
                            L(a,b)=-R_u;
                        end
                    end
                else if nodes(o,p,q)==0 && nodes(u,w,z)==0 % Two air gaps
                        if (p==1 || p==s) && (q==1 || q==s) % Quarters along a face
                            L(a,b)=-1/4*R_a;
                        else if (p==1 || p==s) || (q==1 || q==s) % Halves along a face
                                L(a,b)=-1/2*R_a;
                            else
                                L(a,b)=-R_a;
                            end
                        end
                    else % One sphere and one space
                        if (p==1 || p==s) && (q==1 || q==s) % Quarters along a face
                            L(a,b)=-1/4*R_ua;
                        else if (p==1 || p==s) || (q==1 || q==s) % Halves along a face
                                L(a,b)=-1/2*R_ua;
                            else
                                L(a,b)=-R_ua;
                            end
                        end
                    end
                end
            else if (p+1==w || p-1==w) && (o==u && q==z) % In the same plane and adjacent in the horizontal direction
                    if nodes(o,p,q)==1 && nodes(u,w,z)==1 % Two spheres
                        if (o==1 || o==s) && (q==1 || q==s) % Quarters along a face
                            L(a,b)=-1/4*R_u;
                        else if (o==1 || o==s) || (q==1 || q==s) % Halves along a face
                                L(a,b)=-1/2*R_u;
                            else
                                L(a,b)=-R_u;
                            end
                        end
                    else if nodes(o,p,q)==0 && nodes(u,w,z)==0 % Two air gaps
                            if (o==1 || o==s) && (q==1 || q==s) % Quarters along a face
                                L(a,b)=-1/4*R_a;
                            else if (o==1 || o==s) || (q==1 || q==s) % Halves along a face
                                    L(a,b)=-1/2*R_a;
                                else
                                    L(a,b)=-R_a;
                                end
                            end
                        else % One sphere and one space
                            if (o==1 || o==s) && (q==1 || q==s) % Quarters along a face
                                L(a,b)=-1/4*R_ua;
                            else if (o==1 || o==s) || (q==1 || q==s) % Halves along a face
                                    L(a,b)=-1/2*R_ua;
                                else
                                    L(a,b)=-R_ua;
                                end
                            end
                        end
                    end
                else if (q+1==z || q-1==z) && (o==u && p==w) % Adjacent in different planes
                        if nodes(o,p,q)==1 && nodes(u,w,z)==1 % Two spheres
                            if (o==1 || o==s) && (p==1 || p==s) % Quarters along a face
                                L(a,b)=-1/4*R_u;
                            else if (o==1 || o==s) || (p==1 || p==s) % Halves along a face
                                L(a,b)=-1/2*R_u;
                                else
                                    L(a,b)=-R_u;
                                end
                            end
                        else if nodes(o,p,q)==0 && nodes(u,w,z)==0 % Two air gaps
```

```
                            if (o==1 || o==s) && (p==1 || p==s) % Quarters along a face
                                L(a,b)=-1/4*R_a;
                            else if (o==1 || o==s) || (p==1 || p==s) % Halves along a face
                                L(a,b)=-1/2*R_a;
                                else
                                    L(a,b)=-R_a;
                                end
                            end
                        else % One sphere and one space
                            if (o==1 || o==s) && (p==1 || p==s) % Quarters along a face
                                L(a,b)=-1/4*R_ua;
                            else if (o==1 || o==s) || (p==1 || p==s) % Halves along a face
                                L(a,b)=-1/2*R_ua;
                                else
                                    L(a,b)=-R_ua;
                                end
                            end
                        end
                    end
                end
            end
        end
    end
end
% Diagonal elements of Laplacian matrix
for a=1:1:numel(nodes)
    for b=1:1:numel(nodes)
        if a~=b
            L(a,a)=L(a,a)-L(a,b);
        end
    end
end
Lo=L;
% Grounding nodes
[m,n]=size(L);
f=zeros(m,1); % Auxiliary variable
for a=1:1:s
    for b=1:1:s
        n=sub2ind([s,s,s],s,b,a);
        f=f-10*L(:,n);
    end
end
for a=1:1:s
    for b=1:1:s
        n=sub2ind([s,s,s],1,b,a);
        L(n,:)=[0];
        L(:,n)=[0];
        f(n)=[0];
        n=sub2ind([s,s,s],s,b,a);
        L(n,:)=[0];
        L(:,n)=[0];
        f(n)=[0];
    end
end
b=1; % Auxiliary variable
borrado=0; % Auxiliary variable
while borrado==0
    [m,n]=size(L);
    if b-1==m
        break
    else
        if L(b,:)==[0]
            L(b,:)=[];
            L(:,b)=[];
            f(b)=[];
            b=1;
        else
            b=b+1;
        end
    end
end
% Solve Ohm's equation for U
U=L\f; % Potential matrix
% Total current flowing to the last plane
it=0;
for a=1:1:s
    for b=1:1:s
        n=sub2ind([s-2,s,s],1,b,a);
        ri=sub2ind([s,s,s],1,b,a);
        rii=sub2ind([s,s,s],2,b,a);
        it=it+U(n)*-Lo(ri,rii);
    end
end
R_prev=10/it; % Effective thermal resistance [K/W]
```

Returned variables

```
R_m=1/(2*(s-1)*(r-h)*R_prev); % Effective thermal conductivity [W/mK]
end
```

Bibliography

[1] Alfa Aesar. Product 42689. 26 Parkridge Road, Ward Hill, MA 01835, USA.

[2] J. Allison. Air flow in high aspect ratio heat sink. Master's thesis, Massachusetts Institute of Technology, 2010.

[3] W.G. Anderson, P.M. Dussinger, R.W. Bonner, and D.B. Sarraf. High temperature titanium-water and monel-water heat pipes. In *the proceedings of the 4th International Energy Conversion Engineering Conference and Exhibit (IECEC), American Institute of Aeronautics and Astronautics, Reston, VA*, 2006.

[4] Ashcroft. Model G2 EW-68900-64. 250 East Main Street, Stratford, CT 06614, USA.

[5] N. Atabaki and BR Baliga. Effective thermal conductivity of water-saturated sintered powder-metal plates. *Heat and Mass Transfer*, 44(1):85–99, 2007.

[6] R.W. Balluffi, S.M. Allen, W.C. Carter, and R.A. Kemper. *Kinetics of materials.* Wiley-Interscience, 2005.

[7] GS Beavers, EM Sparrow, and DE Rodenz. Influence of bed size on the flow characteristics and porosity of randomly packed beds of spheres. *Journal of Applied Mechanics*, 40:655, 1973.

[8] A. Birnboim, T. Olorunyolemi, and Y. Carmel. Calculating the thermal conductivity of heated powder compacts. *Journal of the American Ceramic Society*, 84(6):1315–1320, 2001.

[9] D. Bouvard and RM McMeeking. Deformation of Interparticle Necks by Diffusion-Controlled Creep. *Journal of the American Ceramic Society*, 79(3):666–672, 1996.

[10] D.B. Butrymowicz, J.R. Manning, and M.E. Read. Diffusion in copper and copper alloys. part i. volume and surface self-diffusion in copper. *J. Phys. Chem. Ref. Data*, 2(3), 1973.

[11] R.C. Chu. The challenges of electronic cooling: past, current and future. *Journal of Electronic Packaging*, 126:491, 2004.

[12] R.D. Cowan. Proposed method of measuring thermal diffusivity at high temperatures. *Journal of Applied Physics*, 32(7):1363–1370, 1961.

[13] B. Dan, BG Sammakia, and G. Subbarayan. On refining the parameters of a Random Network Model for determining the effective thermal conductivity of particulate thermal interface materials. In *Thermal and Thermomechanical Phenomena in Electronic Systems (ITherm), 2010 12th IEEE Intersociety Conference on*, pages 1–8. IEEE.

[14] DARPA. Broad agency announcement 08-15, January 2008.

[15] T.A. Davis and E.P. Natarajan. Algorithm 907: Klu, a direct sparse solver for circuit simulation problems. *ACM Transactions on Mathematical Software*, 37(3):36:1–36:17, 2010.

[16] A. Devpura, P.E. Phelan, and RS Prasher. Percolation theory applied to the analysis of thermal interface materials in flip-chip technology. In *Thermal and Thermomechanical Phenomena in Electronic Systems, 2000. ITHERM 2000. The Seventh Intersociety Conference on*, volume 1. IEEE, 2000.

[17] Atlantic Equipment Engineers. Product ML-100. 13 Foster Street, Bergenfield, NJ 07621, USA.

[18] H.E. Exner. PRINCIPLES OF SINGLE-PHASE SINTERING. *Rev. Powder Metall. Phys. Ceram. 1,(1/4), 1979*, 1979.

[19] A. Faghri. *Heat pipe science and technology*. 1995.

[20] D. Ganapathy, K. Singh, P.E. Phelan, and R. Prasher. An effective unit cell approach to compute the thermal conductivity of composites with cylindrical particles. *Journal of heat transfer*, 127:553, 2005.

[21] VV Gil', EN Minkovich, and AD Shnyrev. Degassing during prolonged heat-pipe operation. *Journal of Engineering Physics and Thermophysics*, 31(4):1131–1136, 1976.

[22] RK Islamgaliev, K. Pekala, M. Pekala, and RZ Valiev. The determination of the grain boundary width of ultrafine grained copper and nickel from electrical resistivity measurements. *physica status solidi (a)*, 162(2):559–566, 1997.

[23] Japan Electron Optics Laboratory. SEM-5910. 11 Dearborn Road, Peabody, MA 01960, USA.

[24] D. Jenicek. Design of low-power permanent-magnet synchronous motor for use in high-density heat pump. Master's thesis, Massachusetts Institute of Technology, 2011.

[25] S. Kanuparthi, G. Subbarayan, T. Siegmund, and B. Sammakia. An efficient network model for determining the effective thermal conductivity of particulate thermal interface materials. *Components and Packaging Technologies, IEEE Transactions on*, 31(3):611–621, 2008.

[26] S. Kanuparthi, X. Zhang, G. Subbarayan, BG Sammakia, T. Siegmund, A. Gowda, and S. Tonapi. Random network percolation models for particulate thermal interface materials. In *Thermal and Thermomechanical Phenomena in Electronics Systems, 2006. ITHERM'06. The Tenth Intersociety Conference on*, pages 7–pp. IEEE, 2006.

[27] A. Kariya, C. Koveal, J. Allison, M. Kelley, M. McCarthy, J.G. Brisson, and E.N. Wang. A Capillary-Pumped Loop Heat Pipe with Multi-Layer Microstructured Wicks. In *Proceedings of the 9th International Workshop on Micro and Nanotechnology for Power Generation and Energy Conversion Applications (PowerMEMS), 2009*, pages 1–4. PowerMEMS.

[28] W.D. Kingery and M. Berg. Study of the Initial Stages of Sintering Solids by Viscous Flow, Evaporation-Condensation, and Self-Diffusion. *Journal of Applied Physics*, 26(10):1205–1212, 1955.

[29] GC Kuczynski, G. Matsumura, and BD Cullity. Segregation in homogeneous alloys during sintering. *Acta Metallurgica*, 8(3):209–215, 1960.

[30] S.C. Lin and K. Banerjee. Cool chips: opportunities and implications for power and thermal management. *Electron Devices, IEEE Transactions on*, 55(1):245–255, 2008.

[31] Y.J. Lin and K.S. Hwang. Effects of powder shape and processing parameters on heat dissipation of heat pipes with sintered porous wicks. *Materials transactions*, 50(10):2427–2434, 2009.

[32] Lindberg-Blue. Model HTF55667C. 2821 Old Route 15, New Columbia, PA 17856, USA.

[33] Sandvik Osprey Ltd. Tailored alloy. Milland Road, Neath, SA11 1, UK.

[34] Y.F. Maydanik. Loop heat pipes. *Applied Thermal Engineering*, 25(5-6):635–657, 2005.

[35] M. McCarthy, T. Peters, J. Allison, A. Dominguez, D. Jenicek, A. Kariya, C. Koveal, J.G. Brisson, J.H. Lang, and E.N. Wang. Design and analysis of high-performance air-cooled heat exchanger with an integrated capillary-pumped loop heat pipe. In *Proceedings of the 12th IEEE Intersociety Conference on Thermal and Thermomechanical Phenomena in Electronic Systems (ITherm), 2010*, pages 1–8. IEEE.

[36] J.M. Missiaen. Modelling of sintering: recent developments and perspectives. *Revue de Métallurgie*, (12):1009–1019, 2002.

[37] NETZSCH-Gerätebau. Model LFA 457. 37 North Avenue, Burlington, MA 01803, USA.

[38] NIST. Elemental data index, July 2010.

[39] Norgren. Excelon B72G-2AK-AE1-RMG. 5400 South Delaware Street, Littleton, CO 80120, USA.

[40] J. Pan and ACF Cocks. A numerical technique for the analysis of coupled surface and grain-boundary diffusion. *Acta metallurgica et materialia*, 43(4):1395–1406, 1995.

[41] WJ Parker, RJ Jenkins, CP Butler, and GL Abbott. Flash method of determining thermal diffusivity, heat capacity, and thermal conductivity. *Journal of Applied Physics*, 32(9):1679–1684, 1961.

[42] AR Paul, MC Naik, and KNG Kaimal. Mass transport of chromium and nickel in monel-400. *Journal of Nuclear Materials*, 58(2):205–210, 1975.

[43] AR Paul, MC Naik, and KS Venkateswarlu. Mass transport of cobalt and copper in monel-400. *Journal of Nuclear Materials*, 149(3):277–282, 1987.

[44] GP Peterson and LS Fletcher. Effective thermal conductivity of sintered heat pipe wicks. *Journal of thermophysics and heat transfer*, 1(4):343–347, 1987.

[45] SW Petrick. Hydrogen gas generation in water/stainless-steel heat pipes. In *American Society of Mechanical Engineers, Winter Annual Meeting, New York, N. Y*, page 1972, 1972.

[46] D.A. Reay, P.A. Kew, PA Kew, and P.D. Dunn. *Heat pipes*. Butterworth-Heinemann, 2006.

[47] JGR Rockland. On the rate equation for sintering by surface diffusion. *Acta Metallurgica*, 14(10):1273–1279, 1966.

[48] T. Sakurai, T. Hashizume, A. Kobayashi, A. Sakai, S. Hyodo, Y. Kuk, and HW Pickering. Surface segregation of ni-cu binary alloys studied by an atom-probe. *Physical Review B*, 34(12):8379, 1986.

[49] Sartorius. Model GD503NTEP. 30 South Cross Road, Bradford, MA 01835, USA.

[50] Alicat Scientific. Model L-5CCM-D/5V. 7641 North Business Park Drive, Tucson, AZ 85743, USA.

[51] MG Semena, AI Rudenko, and AA Efimova. Mass of hydrogen liberated in stainless steel heat pipes with water during lengthy operation. *Journal of Engineering Physics and Thermophysics*, 53(4):1122–1126, 1987.

[52] T. Semenic and Y. Lin. Thermophysical properties of biporous heat pipe evaporators. *Journal of Heat Transfer*, 130(2):022602, 2008.

[53] R. Singh, A. Akbarzadeh, and M. Mochizuki. Experimental Determination of Wick Properties for Loop Heat Pipe Applications. *Journal of Porous Media*, 12(8):759–776, 2009.

[54] G. Strang. *Computational science and engineering*. Wellesley-Cambridge Press, 2007.

[55] T. Surholt and C. Herzig. Grain boundary self-diffusion in cu polycrystals of different purity. *Acta materialia*, 45(9):3817–3823, 1997.

[56] FB Swinkels and MF Ashby. A second report on sintering diagrams. *Acta Metallurgica*, 29(2):259–281, 1981.

[57] Tresna. ID 111-101-20g. 5, Guilin Hi-Tech Industrial Zone, Guilin, Guangxi Province 541004, P.R. China.

[58] DKL Tsang, BJ Marsden, SL Fok, and G. Hall. Graphite thermal expansion relationship for different temperature ranges. *Carbon*, 43(14):2902–2906, 2005.

[59] R. van der Hofstad. Percolation and random graphs. *New perspectives in stochastic geometry*, page 173, 2009.

[60] TL Wilson and PG Shewmon. The role of interfacial diffusion in the sintering of copper. *AIME MET SOC TRANS*, 236(1):48–58, 1966.

[61] W. Zhang and I. Gladwell. Sintering of two particles by surface and grain boundary diffusion-a three-dimensional model and a numerical study. *Computational materials science*, 12(2):84–104, 1998.